MEASUREMENT OF RECOIL PROTON POLARIZATION IN NEUTRAL PION PHOTOPRODUCTION AT 60 AND 90 DEGREES, USING A WIRE CHAMBER SYSTEM

Thesis by

Shui-uh Cheng

In Partial Fulfillment of the Requirements

For the Degree of

Doctor of Philosophy

California Institute of Technology

Pasadena, California

1970

(Submitted May 25, 1970)

ACKNOWLEDGEMENTS

This thesis work was conceived and supervised by Clemens Heusch. He took part in every phase of its operation. His experience, advice, and guidance was vital to the success of this experiment. He, as head of our group, provided me with continuing motivation and encouragement during the past few years.

Charles Prescott, pioneered in the construction, testing, and running of all wire spark chambers used in the experiment, also linked the PDP-5 computer on-line to the system and kept the computer functioning smoothly throughout the entire experimental period. His creativity, participation, patience, and thoroughness contributed invaluably to the successful execution of all stages of the experiment. Thanks are also due to other members of the group for sharing the task of running, particularly to Kirk McDonald, Edward Lipson, and Robert Kline for their help in wire orbiting calibration.

Walter Nilsson constructed much of the apparatus; his craftsmanship and attention to detail deserves full recognition. My thanks also go to William Friedler for his design and skillful construction of three wire chamber houses.

I am grateful to the synchrotron crew, under Paul Van Ligten, to Earle Emery and Dick Wileman, and to the synchrotron operators, headed by Al Neubieser, for their continued assistance.

Much time was saved due to Greg Stewart's participation in data scanning and data anlysis. I also appreciate his patience in correcting the draft of this thesis.

For financial support, I am indebted to the Atomic Energy Commission, and to the California Institute of Technology.

Above all, much appreciation and thanks go to the U. S. Government and its people whose generosity and kindness made it possible for me to complete my advanced study in this country.

ABSTRACT

We measured the recoil proton polarization in the reaction $\gamma p \rightarrow \pi^{o} p$ at the Caltech electron synchrotron at pion CM production angles around 60^{o} and 90^{o}, and photon energies from 0.65 to 1.375 GeV.

Recoil protons were momentum-analyzed by a bending magnet along with a counter-wire spark chamber system. The polarization was determined by measuring the left-right asymmetry of p-C scatterings in a carbon plate range chamber. The data acquisition was handled by an on-line PDP-5 computer.

Among the 600,000 events taken, approximately 18,000 p-C scattered events survived the kinematics tests and requirements of analyzing power to yield 23 polarization points.

The results indicate a strong angular dependence throughout the angular and energy regions covered. They agree very well with earlier results, but with improved statistics and with finer energy binning in the region of overlap.

π^{o} photoproduction cross sections in the same kinematical region were also messured in the process. The agreement with known values is excellent.

These results are interpreted in the framework of an isobar and partial wave model of π^{o} photoproduction.

To my mother, A-mei

TABLE OF CONTENTS

TABLE OF CONTENTS (Continued)

TABLE OF CONTENTS (Continued)

LIST OF FIGURES

LIST OF FIGURES (Continued)

LIST OF FIGURES (Continued)

LIST OF FIGURES (Continued)

LIST OF TABLES

1. INTRODUCTION

Single pion photoproduction in the photon energy range $k < 1.5$ GeV is largely dominated by s-channel nucleon isobar intermediate states. [1], [2] In the production of charged pions, there is also an important contribution from the t-channel pion exchange term, which determines the behavior in the forward direction. However, the pion exchange term is forbidden in the case of π^o photoproduction, because the existence of a non-zero $\gamma\pi^o\pi^o$ vertex would violate the law of charge conjugation.

In terms of the familiar helicity formulation introduced by Jacob and Wick, [3] and assuming that parity is conserved in photoproduction, we can write down the experimental observables. The differential cross section is

$$\frac{d\sigma}{d\Omega}(\theta) = \frac{1}{2} \frac{q}{k} \sum_{i=1}^{4} |H_i|^2 \qquad (1\text{-}1)$$

where k and q represent the momenta of incident photon and of the produced pion. The polarization of the recoil nucleon in the direction $\hat{q} \times \hat{k}$ is then

$$P(\theta) = \frac{q}{k} \frac{1}{\frac{d\sigma}{d\Omega}(\theta)} \mathrm{Im}(H_1 H_3^* + H_2 H_4^*), \qquad (1\text{-}2)$$

which is due to the interference between different helicity amplitudes. It provides one means of probing the phase relations among the helicity amplitudes.

Another such means is the measurement of the asymmetry parameter $\Sigma(\theta) = (\sigma_\perp - \sigma_{//})/(\sigma_\perp + \sigma_{//})$ for a process initiated by polarized photons, where $\sigma_\perp$ and $\sigma_{//}$ are the cross sections for photon polarization perpendicular and parallel to the production plane. In terms of the helicity amplitudes it is

$$\Sigma(\theta) = \frac{q}{k} \frac{1}{\frac{d\sigma}{d\Omega}(\theta)} \mathrm{Re}(H_1 H_4^* - H_2 H_3^*). \qquad (1\text{-}3)$$

Finally, the asymmetry parameter $T(\theta) = (\sigma_+ - \sigma_-)/(\sigma_+ + \sigma_-)$ for a photoproduction process off a polarized proton target (with σ_+ , σ_- the cross sections for target polarization parallel or anti-parallel to $\hat{k} \times \hat{q}$) can be expressed as

$$T(\theta) = \frac{q}{k} \frac{1}{\frac{d\sigma}{d\Omega}(\theta)} \mathrm{Im}(H_1 H_2^* + H_3 H_4^*) . \qquad (1\text{-}4)$$

So far no data have been available for the measurement of $T(\theta)$. Only a very few measurements on $\Sigma(\theta)$ amd $P(\theta)$ have been made. Even for the most completely investigated observable, $\frac{d\sigma}{d\Omega}(\theta)$, the existing data are by no means complete and consistent. In particular, the reactions $\gamma n \to n\pi^o$ and $\gamma n \to p\pi^-$ have been sparsely investigated due to experimental difficulties.

By expanding the helicity amplitudes in terms of partial waves, Walker [1] was able to fit most of the known experimental data with a model consisting of electric Born terms, nuclear isobars resonances in Breit Wigner form, and a nonresonant background in low

partial waves which is required to vary smoothly with energy. This model yielded fairly satisfactory results in the energy region $k < 1.5$ GeV. It appears doubtful that this approach will be meaningful at higher energies.

Historically, the measurement of recoil nucleon polarization was proposed by Sakurai [4] to try to determine the relative parity of the isobars $D_{13}(1520)$ and $P_{33}(1236)$. If the parities were the same, no polarization should be seen at $\theta^*_\pi = 90^\circ$ near the "second resonance" once we assume no appreciable admixture of other diagrams. However, the experimental result clearly indicated that a substantial polarization did exist in that region, which was interpreted as evidence for the interference of opposite parity states.

As one proceeds to higher photon energy, the number of contributing states increases. The polarization value is now the result of interference between many partial waves. Arguments such as Sakurai's become more difficult to apply. To disentangle the situation, people in the past [2], [5] have tried to describe the photoproduction processes "at intermediate energies" in terms of a combination of s-channel isobars (see Figure 1.1), which dominate the behavior at the low energy, and t-channel pole exchanges, either elementary or Reggeized (see Figure 1.2), which dominate the behavior at very high energy, plus assorted background terms. Among the possible t-channel poles, the ω is believed to dominate the ρ and ϕ according to SU_3 predictions.

The results of the last Caltech π^0 polarization experiment, [6] at $\theta^*_\pi = 60^\circ$, $750 < k < 1450$ MeV were interpreted in terms

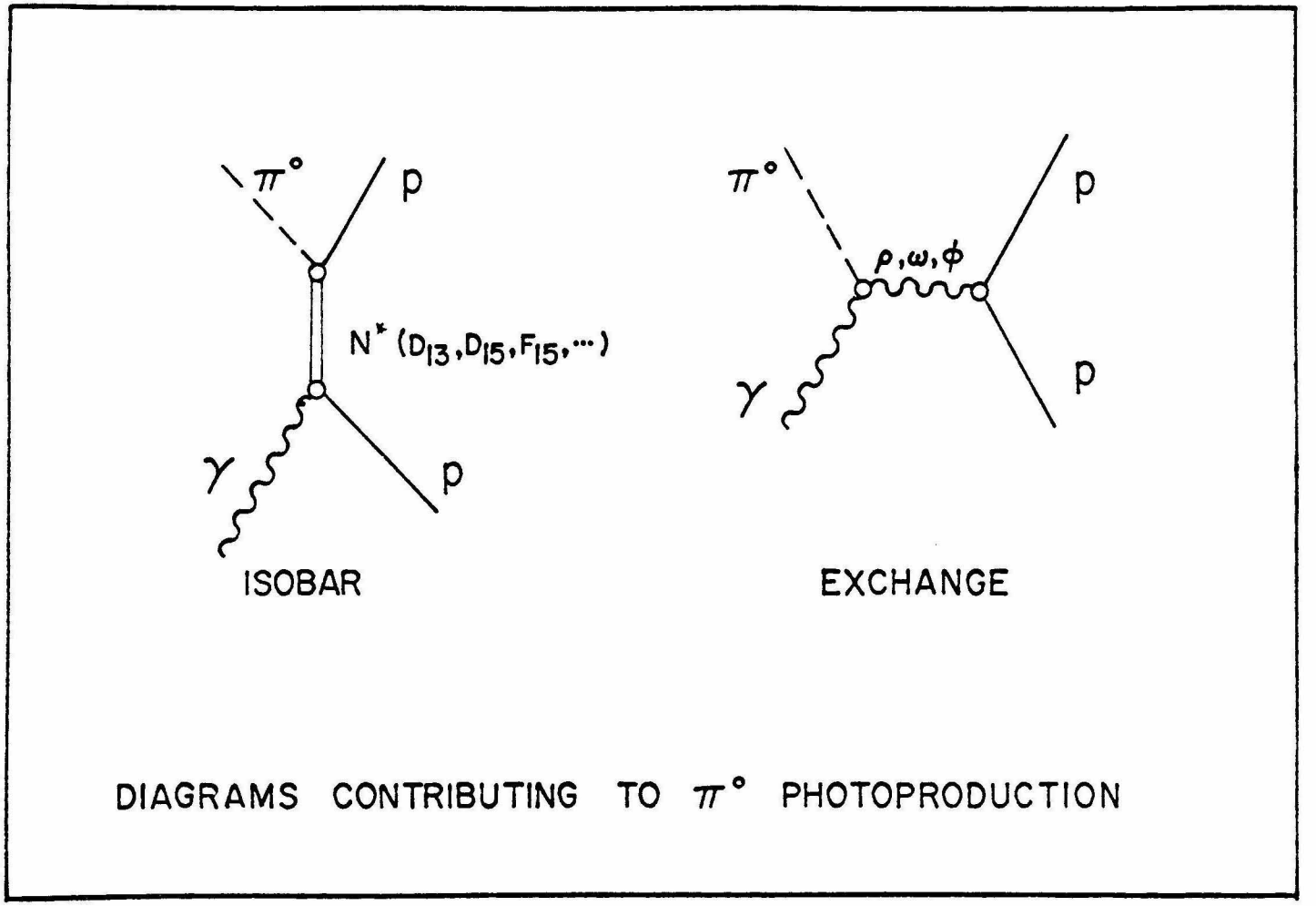
π°
p
N* (D13, D15, F15, ···)
γ
p
ISOBAR
π°
ρ, ω, φ
p
γ
p
EXCHANGE
DIAGRAMS CONTRIBUTING TO π° PHOTOPRODUCTION

Figure 1.1

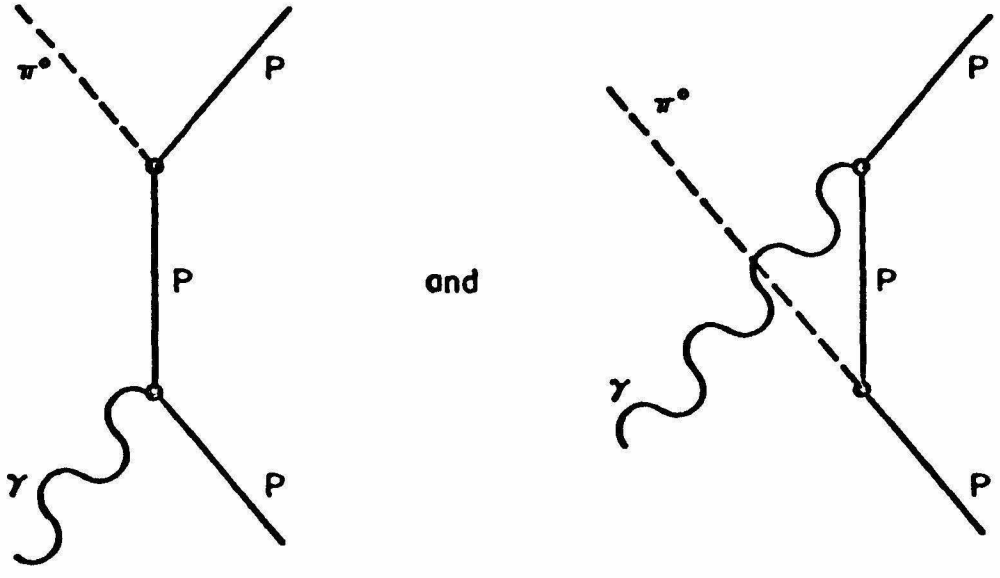

BORN TERMS CONTRIBUTING
TO π° PHOTOPRODUCTION

Figure 1.2

of isobars, Born terms and a slowly turned-on Reggeized ω exchange.

Since that time, the duality picture has been formulated [7], [8] to say that the reaction amplitude can be alternatively described by a complete set of s-channel poles or a complete set of t-channel Regge poles, plus appropriate background terms. It further states that the leading Regge pole exchange roughly corresponds to the sum of all s-channel resonances. This view is in contrast to the once popular conjecture that the leading Regge exchange is related to the non-resonant background terms.

The duality picture implies, in particular, that any attempt to try to mix the leading t-channel pole and s-channel poles in a reaction has to be approached with due caution in order to avoid double counting.

On the other hand, the evaluation of t-channel background integrals hinges on specific models. We may, for example, assume they are due to the presence of Regge cuts and fixed poles.

Our experiment was intended to get the best polarization data possible at $\theta^*_\pi = 63 \pm 8^\circ$ and $\theta^*_\pi = 93 \pm 8^\circ$, and at energies as high as our experimental method would permit, in order to put further constraints on the diagrams contributing in the isobar region.

2. EXPERIMENTAL METHOD AND TECHNIQUES

2.1 General Description

This experiment is to study the two-body reaction

$$\gamma + p \dashrightarrow \pi^o + p$$
$$\hookrightarrow \gamma\gamma \qquad (2.1\text{-}1)$$

The polarization of the recoil proton was measured for incident photon energy k, between 650 MeV and 1375 MeV, at pion center-of-mass production angle θ^*_π, 63 + - 8 and 93 + - 8 degrees. The polarization was measured by the asymmetry in p-C scattering of the recoil proton. (9) The p-C scattering occurred in a large carbon plate wire spark chamber system. This allowed one to follow the entire proton trajectory closely. Since the data collection and data analysis were all computer handled, the possibility of introducing artificial asymmetry was reduced to a minimum.

Briefly, the entire experimental procedure can be described in the following steps. (See Figure 2.1.)

(1) The Bremsstrahlung beam of the Caltech synchrotron was passed through a liquid hydrogen target.

(2) A counter system which detected the recoil proton and the forward decaying photon of the π^o was used to obtain a clear π^o trigger.

(3) A series of wire chambers was used in conjunction with a bending magnet to obtain the complete determination of the π^o photo-production kinematics. The information was stored on-line through a PDP-5 computer.

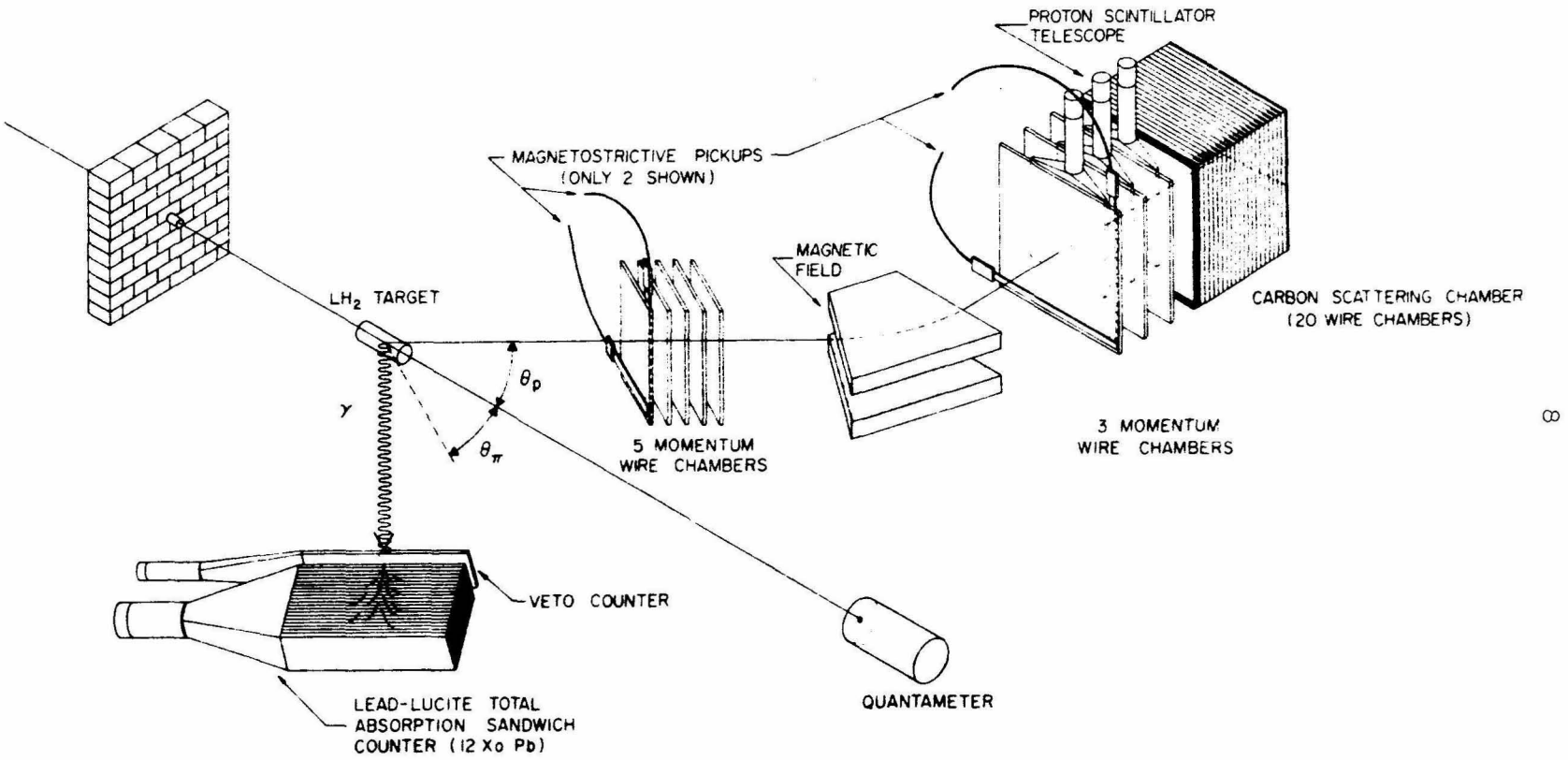

Figure 2.1 Three dimensional experimental setup.

(4) A large carbon-plate wire chamber system was used to detect the recoil proton polarization by means of p-C scattering in the system. The scattering information was recorded on-line on a magnetic tape along with (3).

Nearly six hundred thousand events were taken in two kinematical settings. Approximately 3.4 X 10^{14} equivalent quanta of photon beam were used. Data collection was about one event per two seconds with the synchrotron pulsing once per second. The faster data collection rate was due to the use of the on-line computer (PDP-5) which could handle up to one event per second. Thirty-five thousand events survived the preliminary requirement of p-C scattering angle $\geq 4^{\circ}$. But only 18 thousand finally passed all kinematical and analyzing power requirements and were used to obtain the final polarization values.

In the next sections the details of what has been outlined above will be discussed more thoroughly. The details of the experimental apparatus and some calculation can be found in the appendices.

2.2 Trigger and Selection of Neutral Pion

Figure 2.2 shows the general layout of the experimental apparatus in the Caltech synchrotron. The Bremsstrahlung beam from the machine was collimated, scraped and purified in a permanent sweeping magnet. It then passed through a target containing 0.63 gm/cm^2 of liquid hydrogen. The duty cycle of the synchrotron was about 13%, allowing the fast coincidence electronics and the subsequent spark action more than sufficient time to occur at the rate of data accumulation. (See Table 6.2 for typical counting rates

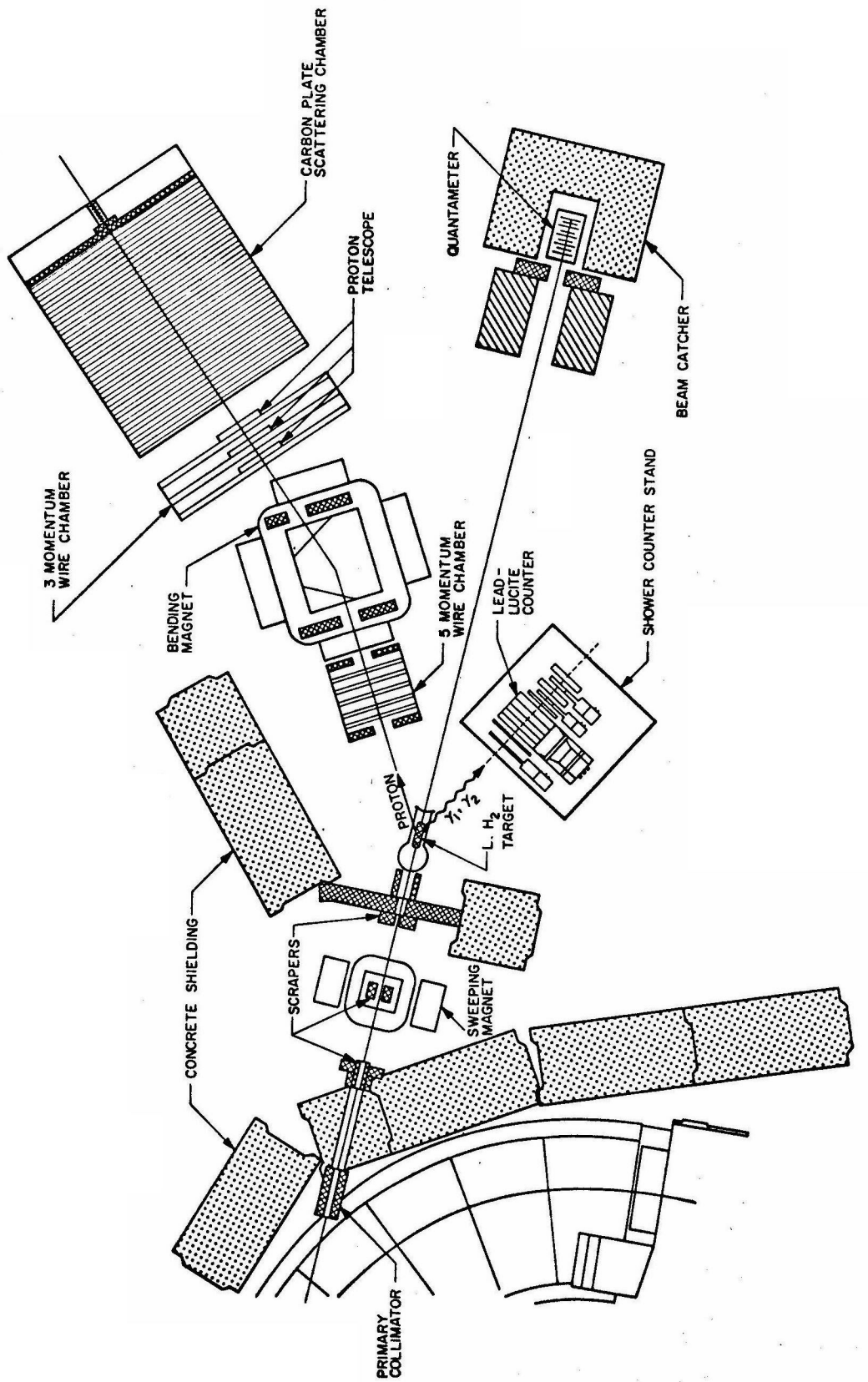

Figure 2.2 General experimental layout.

of the experiment.)

Since the results of this experiment are sensitive to the background, care was taken to insure that contamination was minimal. The major source of background was due to protons assumed to be produced by process (2.1-1) but which in fact were not. The final background contamination of less than 7% (see Appendix 6.17 and Appendix 6.18) was achieved by employing a detection scheme which required a coincidence of the recoil proton and the forward decaying photon in the trigger. Basically, two systems were used to obtain the trigger

(1) The π^{o} detection apparatus consisted of a γ detecting system. The γ detecting system consisted of a scintillation counter and a lead-lucite Cerenkov shower counter arranged to insure a clean separation of γ's from charged π's or protons. The system was placed in the laboratory such that the normal to the aperture was parallel to the horizontal plane. The angle between the normal and the incident Bremsstrahlung was determined by the pion center of mass production angle desired. To improve the cleanness of the π^{o} trigger, a bias of 250 MeV was imposed on the pulse height of the lead-lucite shower counter. This bias helped greatly in discriminating against the multi-pion production background (see also Appendix 6.3).

(2) The proton detection scheme consisted of a proton aperture, a bending magnet, and a proton telescope. The proton aperture allowed recoil protons in the selected kinematical range to pass

through to the bending magnet and excluded the rest of the particles which might or might not originate from the hydrogen target. The bending magnet selected appropriate momenta. The final and the most powerful biasing was set in the proton telescope. The proton telescope consisting of three scintillation counters was located right behind the bending magnet as shown in Figure 2.2. The protons were slow enough to yield counter pulse heights well above those of minimum ionizing particles. The electronic bias on those counters was adjusted so as to exclude particles which had ionizing power significantly below the protons. However, the bias was carefully set not to exclude the protons desired. For all the settings the proton kinematic energy was low enough (mostly below 300 MeV, some as high as 500 MeV, or $\beta_p < 0.77$) that the proton telescope obtained a reasonably clean pulse-height separation between protons and $\beta \simeq 1$ charged particles, mainly π's. A typical pulse height distribution for protons is shown in Figure 6.6 (see also Appendix 6.4 for the details of the proton side of the experiment).

To summarize, a π^o signature was a three-fold coincidence in the proton telescope in coincidence with the γ system.

2.3 On-Line Wire Spark Chamber System

This experiment enjoyed a great improvement over the previous Caltech polarization experiment [6] by using an on-line wire spark chamber system. The system registered the event information on a magnetic tape instead of using the conventional optical method, and

therefore was relieved of the complicated and tedious lens correction. Human errors introduced in the processes of scanning and measuring were also greatly reduced.

In fact, from the data acquisition through the preliminary data analysis all the way to the final calculation of proton polarization, the whole operation was completely computer handled. Not only the time and the costs were considerably reduced as compared with a typical optical spark chamber experiment, but the experiment was capable of producing more reliable results.

The event information stored on the magnetic tape emphasized heavily the proton side. Since no hodoscope was used on the π^{o} side to determine the location of the shower, the only information the π^{o} system provided was the pulse height of the lead-lucite shower counter. The information of the recoil proton trajectories before and after the bending magnet was registered in digitized form, each number representing a spark location in either the horizontal or vertical view of a wire spark chamber.

Knowing the proton trajectories and the magnet configuration, and assuming a clean π^{o} trigger, the photoproduction kinematics could be completely reconstructed.

In the case of p-C scattering, the information of the scatter kinematics could be abstracted from the spark locations in the wire chambers in the carbon-plate scattering house.

The measured variables describing the kinematics of the event, the errors in these variables, and the manner in which

they were obtained are given in Table 2.1. Complementary to this table is Figure 2.3 which defines the variables.

2.4 Proton Carbon Analyzing Scatter

Consider a p-C scatter in the context of general spin 1/2 - spin 0 scattering. The most general amplitude one can write which conserves all quantities conserved by the strong interactions (e.g., parity, J ... etc.) is

$$F = f + \vec{\sigma} \cdot \hat{n}_2 \, g,$$

the $\vec{\sigma}$ being the usual Pauli spin matrices, $\hat{n}_2 // \hat{p} \times \hat{p}'$ (where $\wedge$ indicates a unit vector), f and g are Fermi's invariant amplitudes. One can easily show that a spin 1/2 beam with initial polarization $\vec{P}$ gives (10)

$$\sigma(\theta,\Phi) = [|f|^2 + |g|^2 + 2\mathrm{Re}(f^*g)\hat{n}_2 \cdot \vec{P}] = \sigma_o(\theta)(1 + A\,\hat{n}_2 \cdot \vec{P}) \qquad (2.4\text{-}2)$$

$\sigma_o(\theta) = |f|^2 + |g|^2$, is the unpolarized cross section,

$$A = 2\mathrm{Re}(f^*g)/\sigma_o(\theta);$$

A, the analyzing power, is a property of the scattering material, i.e., carbon, which has been measured in other experiments (see Appendix 6.14).

In the case of π^o photoproduction with the initial unpolarized, parity conservation requires that the polarization of the recoil proton on the production plane be zero, and if the final state proton is polarized at all it can only be in a direction

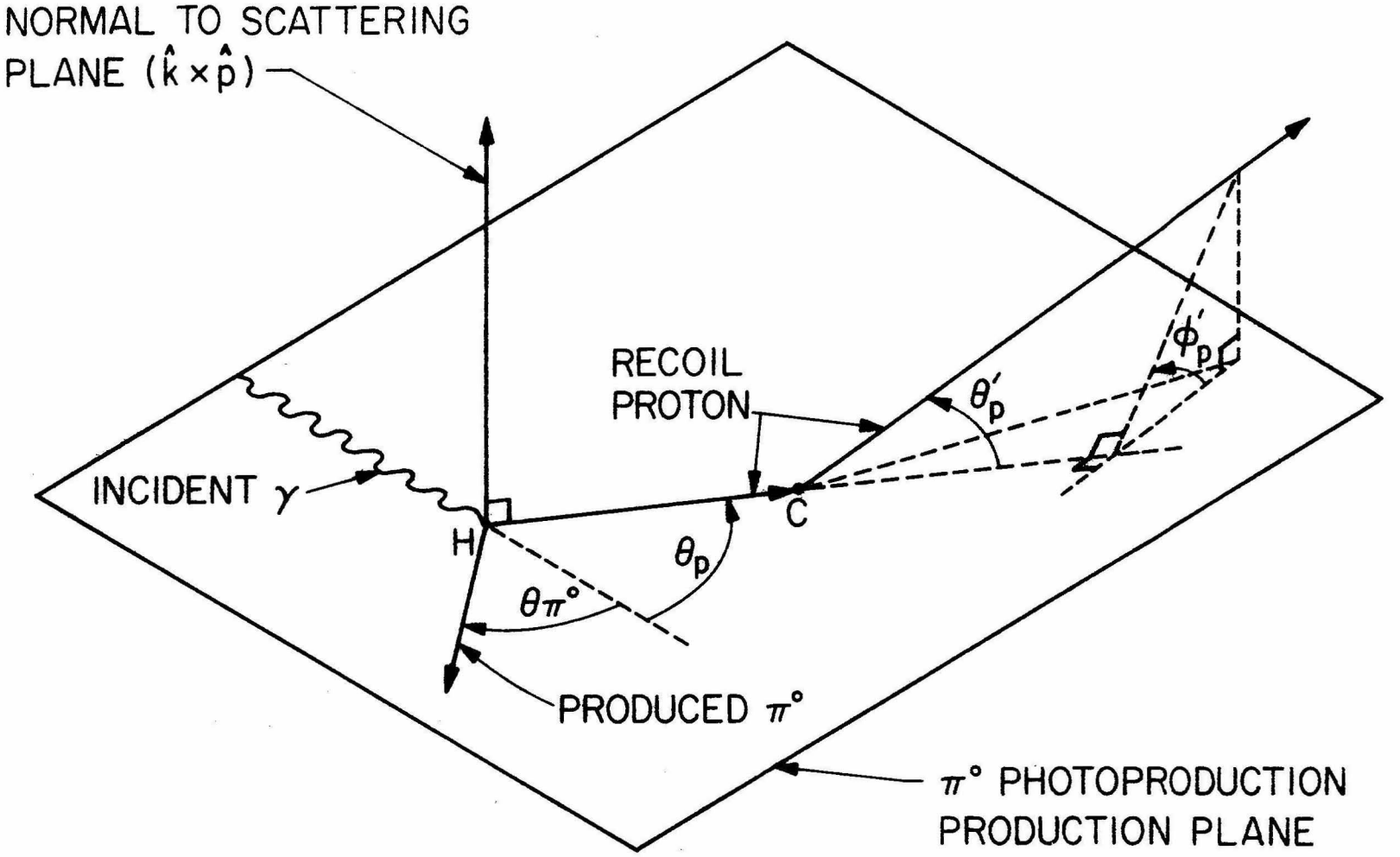

Figure 2.3 γ-p and p-π° interaction kinematics.

TABLE 2.1: MEASURED VARIABLES AND ERRORS

Measured Variables	Procedure for Obtaining Values of Variables	Typical Uncertainties	Major Source of Errors
θ_p	Measurement of tracks in the front wire chambers	0.28	Multiple scattering ≈ 0.28 Alignment error ≈ 0.05
R_p	Total range in carbon	$< 4\%$	The error stated holds only for events without p-C scattering or with elastic p-C scattering. Error here is due primarily to finite carbon thickness
θ'_p	Measurement of tracks in the carbon plate range chamber	$< 2\%$	Finite wire spacing and chamber spacing combined with the p-C scattering vertex
Φ'_p	Same as θ'_p	< 0.1 in $\cos \Phi'_p$	Same as θ'_p
R'_p	gm/cm^2 of equivalent carbon from LH_2 target to the p-C scattering vertex	$< .8$ gm/cm^2	Uncertainty at target combined with the uncertainty in determining the p-C vertex in carbon plate
R''_p	gm/cm^2 of equivalent carbon from p-C scattering vertex to the end of proton track	< 1.1 gm/cm^2	Error in vertex determination folded with uncertainty in stopping location of proton at end of track

perpendicular to the production plane. Hence, take $\vec{P} = \hat{n}_1 P$, $\hat{n}_1 = \hat{k} \times \hat{p}$; equation (2.4-2) then gives

$$\sigma(\Theta'_p , \Phi'_p) = \sigma_o(\Theta'_p) (1 + A P \cos \Phi'_p). \qquad (2.4\text{-}3)$$

See Figure 2.3. Equation (2.4-3) is the key to a proton polarization measurement in our energy range. One can proceed in two ways from here:

(1) Scintillation counters can be set up behind a carbon block such that $\cos \Phi'_p = +1$ for one counter, α, and $\cos \Phi'_p = -1$ for the other, β. Then, assuming the two counter detection efficiencies equal,

$$N_\alpha = c(1 + AP), \; N_\beta = c(1 - AP),$$

N being the number of counts and c a constant; and

$\epsilon = \dfrac{N_\alpha - N_\beta}{N_\alpha + N_\beta} = \bar{A}P$, where $\bar{A}$ is the average analyzing power over the kinematical region of acceptance (usually quite limited for this method). By looking at the counting asymmetry ϵ, and knowing the analyzing power, A, one can obtain the polarization, P.

(2) A wire spark chamber system containing carbon plates can be used to see the scatters. In this case, the greater part of the proton trajectory can be seen, and so apparatus-introduced asymmetries are largely avoided. Also, a rather precise measurement of Θ'_p, $\cos \Phi'_p$ can be made over relatively large ranges of these variables compared with method 1. Here statistical methods are used to determine the polarization, briefly as follows. The

expected distribution for p-C scattering is given by (2.4-3). For each (k, Θ^*_π) bin one measures a large number, N, of such scatters each with an associated $\cos \Phi'_{p_i}$ and A_i. We then form

$$L(P) = \prod_{i=1}^{N} (1 + A_i P \cos \Phi'_{p_i}), \text{ for each } (k, \Theta^*_\pi) \text{ bin.} \qquad (2.4\text{-}4)$$

As described in more detail later (Section 3.4), L(P) is the so-called likelihood function. The value of P which maximizes L(P), P*, is the best value of the polarization obtainable from the data. This method assumes, of course, that no artificial asymmetries have been introduced into the observed scatter asymmetry. One also must be sure that the detection efficiency for scatters is independent of polarization. (These considerations are treated in Appendix 6.12.)

This experiment used the latter method for the polarization determination. The chambers used are described in Appendix 6.6. The parameters measured were Θ'_p, $\cos \Phi'_p$ and the proton ranges before and after scattering. These parameters were used to determine the relevant value of analyzing power associated with each event (Appendix 6.14). Table 2.1 together with Figure 2.3 completely defines these variables; in addition, the table mentions the way they were obtained, and the approximate errors involved.

2.5 Backgrounds

A. Proton Compton Scattering Background

From Table 6.7 in Appendix 6.18, one can see the similarity between the kinematics of single pion photoproduction and proton

Compton scattering. Since our system did not intend to detect both decaying photons of the pion, proton Compton scattering events could become a very important source of background. The minimum pulse height requirement in the shower counter did not help to discriminate against the Compton background events, for the γ from Compton scattering usually possesses higher energy than the forward decaying γ of the π^o .

This background contamination could be estimated from cross section information of Compton scattering at CMS 65^o (11) (see Figure 2.4) and at CMS 90^o (12) (see Figure 2.5). By folding in the geometric detection efficiency of Compton scattering in our system with the known cross sections, one could estimate the background counts as a function of incident photon energy and the CMS angle. A subtraction of these counts has to be made before the estimation of single pion production cross section (see Section 3.5).

The Compton scattering constituted about 4% of events at $\theta^*_\pi = 63 +- 8^o$ and about 3.1% at $\theta^*_\pi = 93 +- 8^o$, which is considered tolerable in this experiment. (Error bar 10% in polarization.) For details of the calculation see Appendix 6.18.

B. Multipion Photoproduction Background

The other potential source of background is the multipion photoproduction. Since the upper limit of the incident photon energy was 1375 MeV, photoproduction of up to 6 pions was energetically possible. The charged pions were excluded by the veto counter of the γ detector. Therefore one expects that the

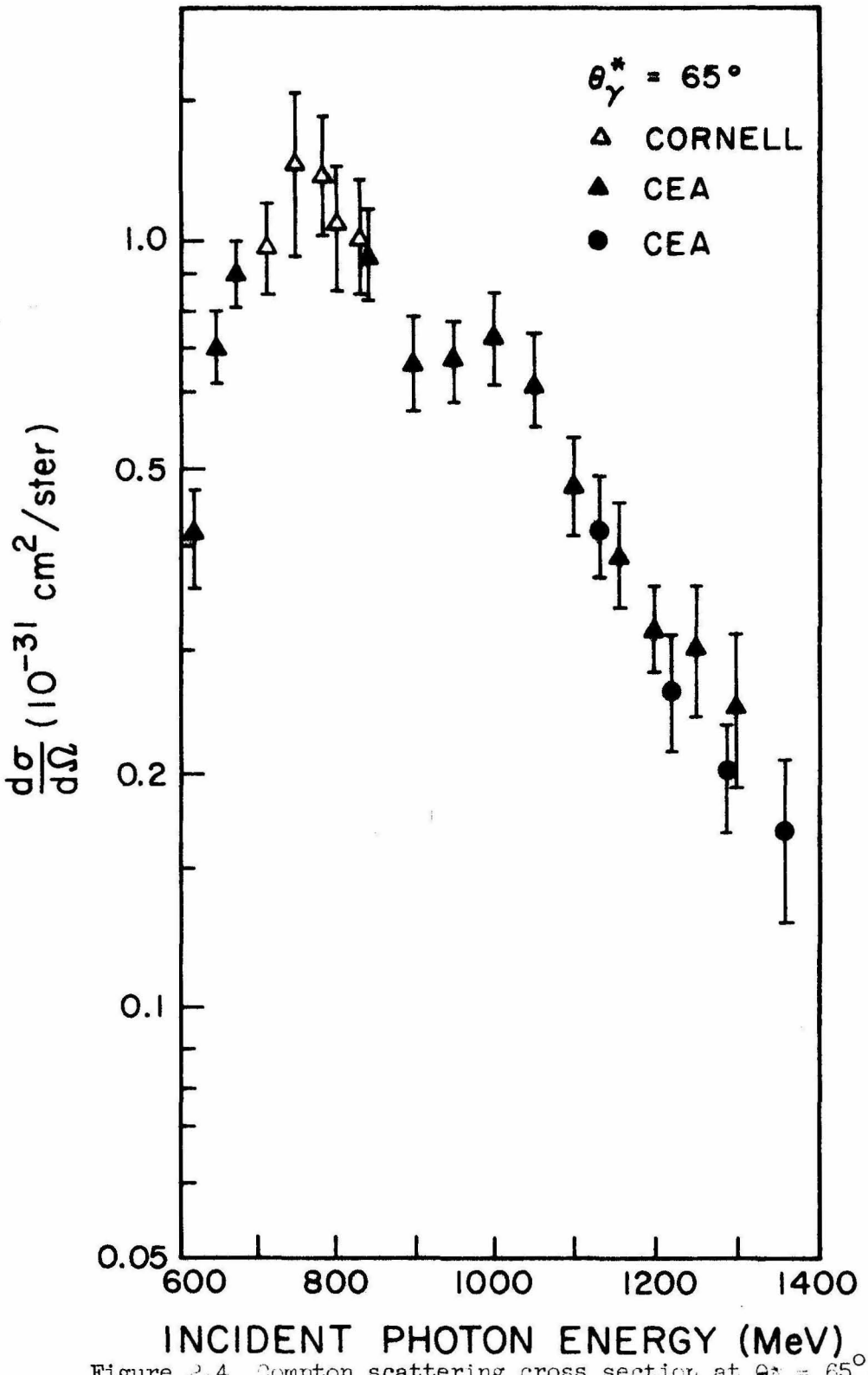

Figure 2.4 Compton scattering cross section at $\theta_\gamma^* = 65^\circ$.

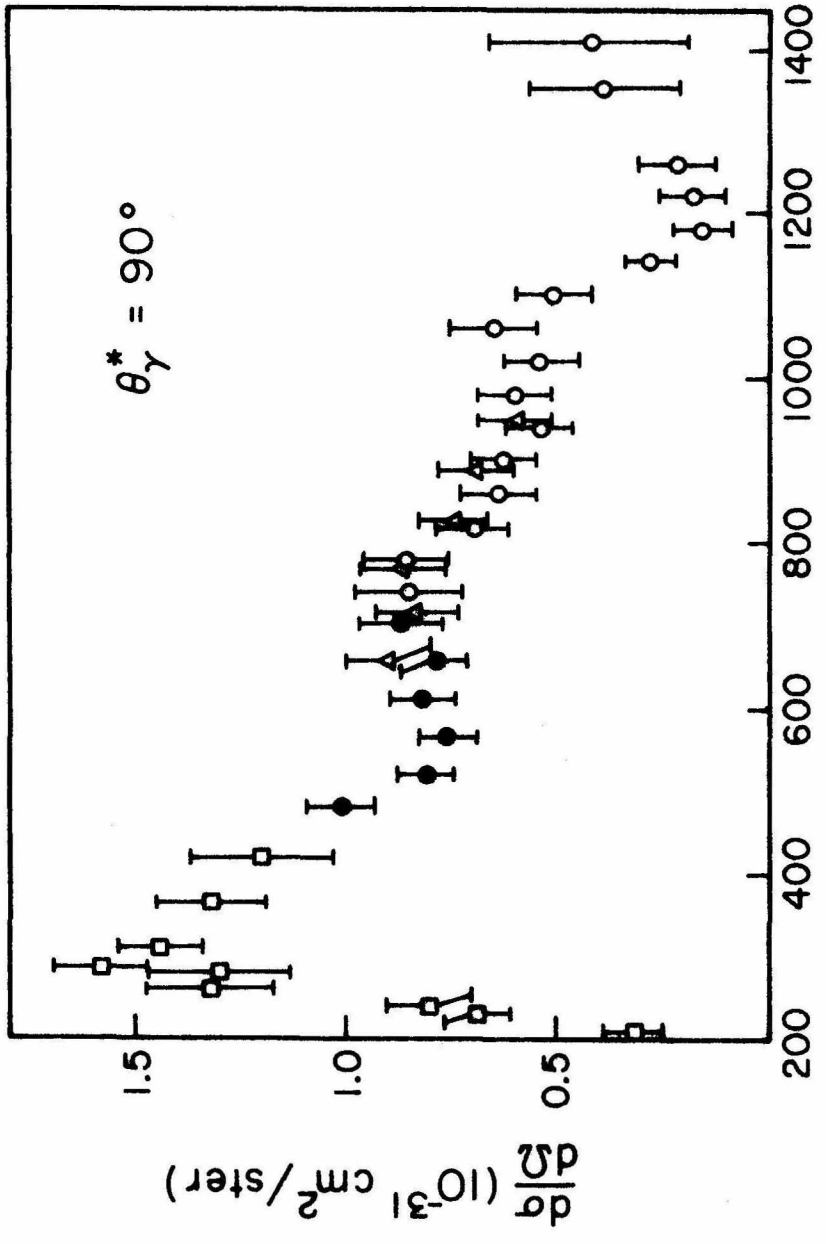

Figure 2.5 Compton scattering cross section at $\theta^*_\gamma = 90°$.

remaining source of background, aside from proton Compton scattering, to be multiple neutral pion photoproduction simulating single neutral pion photoproduction in the detection apparatus.

It is assumed that the two π^o photoproduction dominated the rest of multi π^o production, for a minimum of 250 MeV pulse height requirement in the shower counter would bias off most of the pions from multi π^o processes where the production cross sections were not available and were believed to be small.

No reliable estimation of the total cross section of two π^o photoproduction has been available. A comparison of bubble chamber data [13] and counter data up to 1200 MeV incident photon energy showed that essentially all the cross section for the pion photoproduction was accounted for by single neutral pion photoproduction.

A Monte Carlo estimation of the detection of the two pion background was made (see Appendix 6.17). In addition, by assuming a uniform $2\pi^o$ cross section over the entire incident photon energy range, one was able to estimate the contamination to be 3.2% at $\theta^*_\pi = 93 \pm 8^o$ and 2.8% at θ^*_π 63 ± 8^o.

To summarize, the total contamination of background events could amount to 7% where 4% is from proton Compton scattering and the rest from two π^o process.

3. DATA ANALYSIS

3.1 Track Recognition

The small storage space of the PDP-5 computer (4 K) and its relatively slow cycle time (6 μsec) forbids on-line data analysis beyond simple distribution displays, etc.. All the subsequent analysis was done on Caltech's IBM 360/75 machine.

An efficient and accurate track recognition scheme is of vital importance to the success of data analysis. Two separate schemes were devised, one to find tracks in the front five wire chambers, the other to find tracks in the wire chambers behind the bending magnet (total up to 23 chambers) with an option to find the scattered track in case of a p-C proton carbon scatter.

Both schemes have been well tested, for every setting (a total of 7) at least 1,000 events were carefully examined. The detailed computer output was checked with the playback display on the RM 561 A oscilloscope event by event. The playback option helped greatly in perfecting the track-fitting schemes.

A. Front Chambers

It has been noticed that throughout the experiment no more than two recognizable tracks ever appeared in any view of the front chambers. In case of multiple sparks, no immediate attempt was made to try to identify their location in space, i.e., we did not try to correlate the spark locations from both views of the same chamber. Instead, the scheme dealt with track recognition in the horizontal and vertical views separately, thus

reducing the tedious spark stereo problem to the much simpler track stereo problem (see also Section 3.1-e).

The wooden box which held the five front wire chambers was shielded by an 1/2" lead plate facing the target with an opening of 3" x $3\frac{1}{2}$" centered at the central proton trajectory. Therefore, prior to the track recognition subprogram, all sparks falling outside the proton aperture were removed, since geometrically these sparks could not have originated from the liquid hydrogen target and therefore were undesired in the track fitting. This constraint cleaned up a lot of background sparks and greatly reduced the efforts in the track fitting.

The algorithm of this scheme took advantage of the fact that there were only five chambers involved, a relatively small number. The scheme was capable of finding up to two tracks in one view. It began with constructing the first possible line segment, which, in general, was the line joining the first spark of the first chamber to the first spark of the next chamber, then extrapolated this line segment into other chambers. If, in a given chamber, the distance from the extended line to the nearest spark in this chamber was within a few standard deviations (one standard deviation here was chosen to be the average wire spacing of the wire chamber, namely 1 mm. The number of standard deviations used was adjustable.) this spark would be picked up. The following chambers (of the front 5) would be likewise treated and these picked sparks, along with the sparks forming the beginning line segment, were used to make a least square line fitting. In case

of not having enough sparks to make the line fitting, the first line segment would be abandoned and a second possible line segment which, in general, was the line joining the first spark of the first chamber to the second spark of the second chamber, would be constructed. And a similar spark searching and line fitting process was repeated.

In the least square line fitting, assuming N sparks to begin with, the scheme always started with a fitting using all N sparks. If the chi-square value of the fitting turned out too large to be accepted, then the first possible combination of N-1 (N-1 being 3 or 4 now) out of the original N sparks would be chosen to do the fitting, and the chi-square value examined. This process would be repeated until either a satisfactory chi-square value was found or the fittings of all possible combinations of sparks of 3 and up were exhausted. In either case no more than $C_5^5 + C_4^5 + C_3^5 = 16$ trials would be attempted. Should the scheme fail to find a straight line after exhausting all possible combinations, a next possible line segment would be constructed and a similar spark searching and line fitting process followed.

When a line was finally successfully found, the sparks which contributed to this line fitting would then be removed so that an exact track searching procedure could be applied to the remaining sparks to look for a possible second track. (Obviously this scheme can be generalized to search for more than two tracks.)

By choosing the acceptable chi-square value to be 3* (M-2); where M is the number of sparks participating in the line fit,

M-2 being the degree of freedom in a straight line least square fitting, throughout the analysis, it was found that on the average it took between three and four trials to find a successful track.

The efficiency of finding at least one track in the front chambers is defined as the product of the efficiencies in the horizontal and vertical views. It ranges from 85% to 99.7%. The drastic variation from nearly 1 to 85% was caused by the malfunction or inefficiency of a particular chamber. Most of the time the efficiency was about 99%. A careful examination of a sample of unsuccessful events clearly indicated that these events were either falsely triggered or totally unrecognizable.

B. Back Chambers

We defined a fiducial area containing all the useful sparks in the three wire chambers which were sandwiched with the proton telescope to be a 10" by 12" area. This was slightly larger than the size of the proton telescope. In the scattering house where the p-C scattering is anticipated (i.e., the spark may appear in any part of the chamber), only those sparks appeared within 2 cm of the fiducials are excluded. This screening was intended to get rid of edge sparks.

Since no more than one track was ever observed in the back chambers throughout the entire experiment, the scheme could concentrate on finding only one track in one view at a time, keeping in mind that the track might penetrate a large number of wire chambers (up to 23). The first pass of this scheme was to find

a reasonable first guess line equation without performing a least square line fitting.

To begin with, all line segments connecting the sparks of immediately adjacent chambers were constructed (as compared with constructing a line segment at a time which could be formed between any two sparks of two distinct chambers in the previous scheme). Each line was represented by the line equation X_i(or Y_i) = $M_i Z + B_i$. The slopes, M's, and the intercepts, B's, of all line segments were then grouped into an M — B plot (Figure 3.2) where each point represents a line segment. If a cluster of points is observed by the computer to fall into a region of $\Delta M \leq (1 + \bar{M}^2)\, \Delta\theta_{max}$ and $\Delta B \leq \Delta M * Z$, then the first guess line equation is defined as the arithmetical mean of this cluster of points, namely, $\bar{M} = (\sum_{i=1}^{N} M_i)/N$ and $\bar{B} = (\sum_{i=1}^{N} B_i)/N$. In the actual implementation of this algorithm, the mean value of the slopes, $\bar{M}$, was defined step by step; the first $\bar{M}$ was defined as M_1, when a second line segment satisfied the prescribed criteria of ΔM and ΔB, $\bar{M}$ would be modified as $\bar{M} = (M_1 + M_2)/2$. This $\bar{M}$ was used to try a third line segment, etc.. $\Delta\theta_{max}$ is the maximum tolerable angular fluctuation of the line segments which physically belong to the same trajectory. In this experiment, the wire spacing of the chambers was 1 mm., the minimum distance between two adjacent wire chambers was 1.5 cm., therefore a fluctuation of up to $\Delta\theta_{max} = \frac{1}{15} \simeq 4^{\circ}$ was expected for the line segments which belong to the same track. In principle, $\Delta\theta_{max}$ could be greatly reduced by either decreasing the wire spacing

or increasing the chamber distance.

The $\Delta\theta_{max} = 4^{o}$ condition set the upper limit for the angular resolution of the p-C scattering, i.e., the scheme could not resolve a less-than-4-degree scatter in one view, since, by definition, the line segments of the scattered track with $\theta_p' \leq 4^{o}$ would be included in the incoming ones.

In the second part of this scheme, the first guess line equation was used to pick up sparks within a few standard deviations of it. (The multiple scattering increased the uncertainty of the spark location. One standard deviation was chosen to be 2 or 3 mm. depending on the relative location of the wire chambers.)

All the sparks thus gathered were put into a least square line fitting. If the chi-square value of the fitting was too large to be accepted, the fit would be abandoned. No attempt was made to try to reduce the number of sparks and repeat the least square fitting all over again as was done in the previous scheme. There were three reasons to justify this measure. First of all, since the number of sparks involved could be as high as 23, to exhaust all mathematical combinations of 3 sparks and up was an impossible task even with a very high speed digital computer like the IBM 360/75. Secondly, there were only up to 2 sparks allowed to appear in the last 20 out of the total 23 chambers (two scalers for each view of a chamber). The proton lead aperture, bending magnet, and the proton telescope together greatly reduced the chance that an accidental charged particle

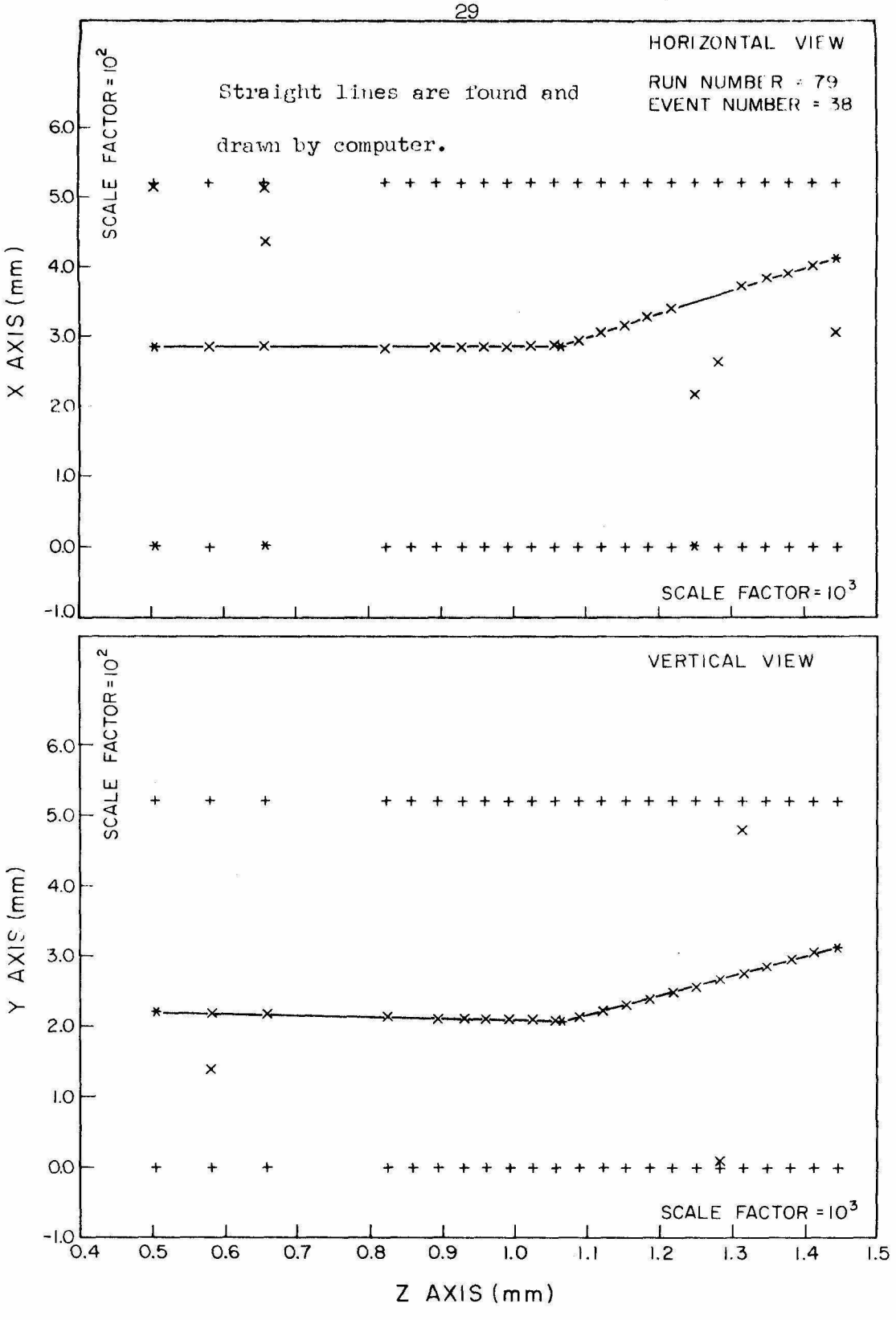

Figure 3.1 Scale plot for track identification.

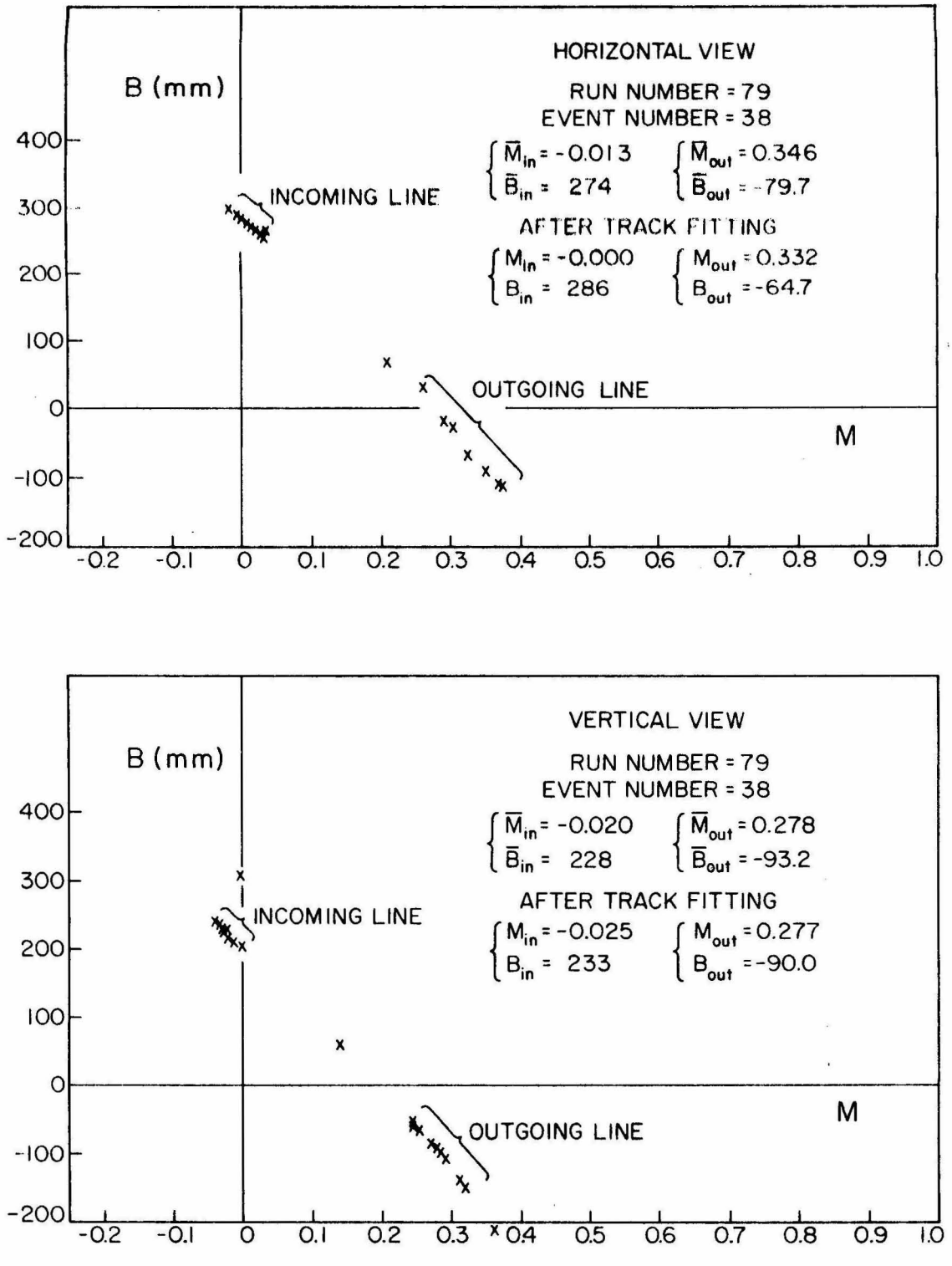

Figure 3.2 M-B plot for track identification.

would penetrate into the scattering house. It was unlikely that such a spark would appear so close to the first guess line as to be included in the line fitting. Thirdly and lastly, we allowed a large acceptable chi-square value for the fitting. It was set to be 5 x (M-2), where M-2 is the number of degree of freedom in a straight line fitting of M sparks.

The efficiency of finding a track in the back chambers is, as in the previous case, defined as the product of the efficiency in the horizontal and vertical views. It was on the order of 97%. The fluctuation of efficiency was only a few percent. The reason for this more stable track finding efficiency was due to the fact that more chambers were involved in the fitting. The scheme thus was less dependent on the performance of any particular chamber or chambers. In fact, during a certain period of data acquisition, one chamber was found dead, but no immediate action was taken to correct it until the end of that run. The analysis efficiency of this run did not show a marked reduction. To summarize, with a large number of chambers involved, it was the collective behavior which determined the efficiency of track recognition.

C. Solution To The Stereo Problem

As stated in Section 3.1-A, only the track stereo problem in the front chambers needs to be solved. To be more specific, a unique solution has to be devised in the case where two tracks were found either in the horizontal or vertical view, or both views, of the front chambers to determine which one of the

double tracks really was associated with the recoil proton. The very fact that only one track was found in the back chambers greatly helped to solve this ambiguity.

It was found that only between 3 to 5 percent of the events had double tracks in one view or the other. For a normal event with only one track in each view, the treatment of the stereo problem was bypassed. If the double tracks were found in the horizontal view, the first logical test to resolve the ambiguity was to extrapolate the tracks back to the target area and make sure the tracks really came from it. The one which did not originate from the target would be suppressed. In the case that both tracks survived the test, the second test would call upon one of the tracks at a time together with the one found in the back chambers to do the proton momentum fitting (see Appendix 6.11-A). Whichever first yielded an acceptable momentum would stay for further tests. If the double tracks were found in the vertical view, the first test was again to extrapolate both tracks to the target area, and suppress the one which did not originate from it. Usually this simple test alone would solve the ambiguity. Otherwise, a second test was made to match the slopes of the tracks before and after the bending magnet. A first order calculation using Maxwell's equations showed the vertical slope of a charged particle trajectory would not be changed by going through a bending magnet whose magnetic field was vertical. Therefore, the track that had a slope consistent with the one in the back chambers would survive the test. This completed the

identification of the track stereo problem.

D. Determination of Proton Carbon Scattering

The primary purpose of the preliminary data analysis of a polarization experiment is to filter out as early as possible the non-proton carbon scattered events which do not carry polarization information. The track recognition scheme in the back chambers (see 3.1-B) was modified to recognize the scattered track. In the M-B plot mentioned for the line segments in the back chambers, if a second distinct cluster of points was found in addition to the one corresponding to the incoming track, a similar treatment would be applied to find its first guess line equation. To define a useful scatter, we required at least a 4 degree scattering angle in at least one view, i.e., the projection of the p-C scattering polar angle into either the horizontal or the vertical view should be no less than 4 degrees. This constraint would pick up all events with $\tan \theta'_p \geq \sqrt{2} \tan 4^o$ or crudely, $\theta'_p \geq 4^o \sqrt{2}$; but only a part of the events in the region $4^o \leq \theta'_p \leq 4^o\sqrt{2}$ depending on whether the projection of θ'_p in any view would exceed 4 degrees.

Before we entered into the second part of the least square fitting, a first-guess location of the scattering vertex along the common axis (Z axis) of both views was needed to separate the back wire chambers into two regions. The location of the vertex was calculated from the view which showed the larger preliminary scattering angle. Often, only one view showed a

greater than 4 degree scatter and the other view did not show a scatter. In this case, the first-guess vertex was calculated from the view with scatter. By filtering the sparks in the two regions (one before, the other after the vertex) using the two first-guess line equations (these two line equations might be identical in the view where the outgoing track is within 4 degrees of the incoming one), one could proceed to do the least square fitting as previously described. The exact location of the scattering vertex along the common axis could not be uniquely determined if one tried to calculate it from separate views, since this only resulted in two different numbers. To get the exact location of the scattering vertex, one has to construct the incoming line equation in space uniquely out of the 2-dimensional line equations in the horizontal and the vertical views. Similarly, the outgoing line equation in space was uniquely constructed out of the 2-dimensional outgoing line equations in the horizontal and the vertical views. The vertex was defined to be the center of the minimized line segment between these two spatial lines. A very stringent bias was imposed to reject the events with minimized line segment larger than 1 cm. Only about 2.5% of the events were rejected by this constraint. A careful examination of these rejected events showed that they either were highly inelastic in nature and therefore could not yield useful information for polarization (see Appendix 6.14) because of undefined analyzing power, or they would also be rejected in the subsequent tests. Figure 3.1 shows a typical scattered

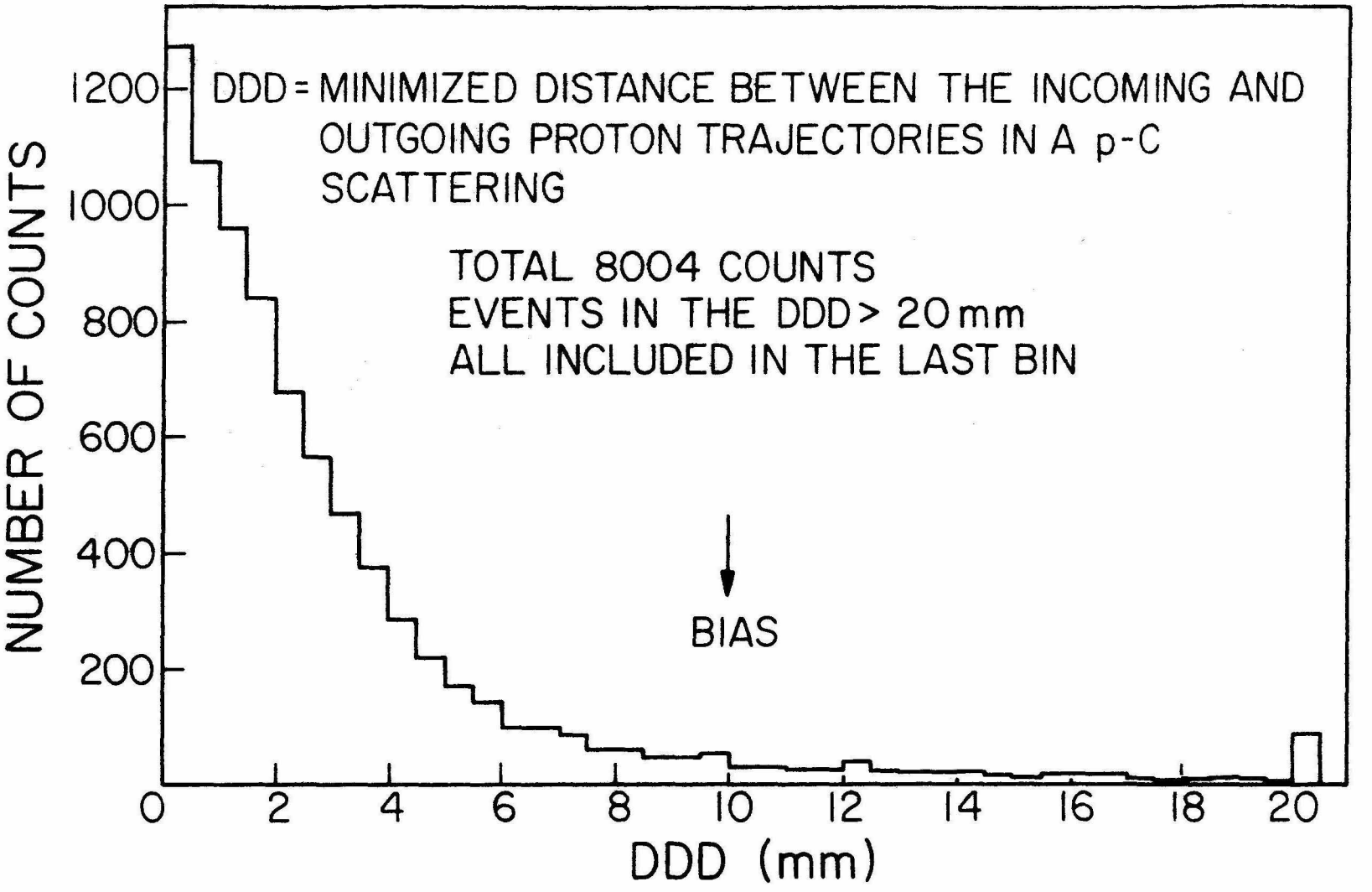

Figure 8.3 Distribution of the minimized distance in space between the incoming and the scattered proton trajectories.

event found by the computer.

3.2 Major Biases in Preliminary Data Reduction

Prior to the track recognition, events with shower counter pulse height below 250 MeV were discarded in order to suppress the possible multiple π^o production background. A more detailed explanation is given in Appendix 6.17. The time-of-flight distribution between the signals from the shower counter and one of the proton scintillation counters served as a redundant check of the coincidence of the system. The full width of the time-of-flight distribution was on the order of 5 nsec. which was largely caused by the variation of the velocity of the recoil protons. Throughout the preliminary data analysis, even without setting a bias on it, the distribution of the surviving events always looked normal and clean. Therefore the distribution was simply left as it was without the imposition of any bias.

The first major bias applied was to make sure that the recoil proton did originate from the liquid hydrogen target in the horizontal view. The projection of target on the horizontal plane was a rectangle 9.18 x 3.81 cm. A 1/2" polyethylene plate was placed in front of the first wire chamber to suppress soft electrons and photons. This plate induced some multiple scattering, which in turn broadened the shoulders of the target distribution (see Figure 3.4-A). The events falling outside the extended target area were suppressed.

A similar check was then applied to make sure that the recoil proton came from the target in the vertical view. Although the diameter of the target was 3.81 cm., the target distribution (see

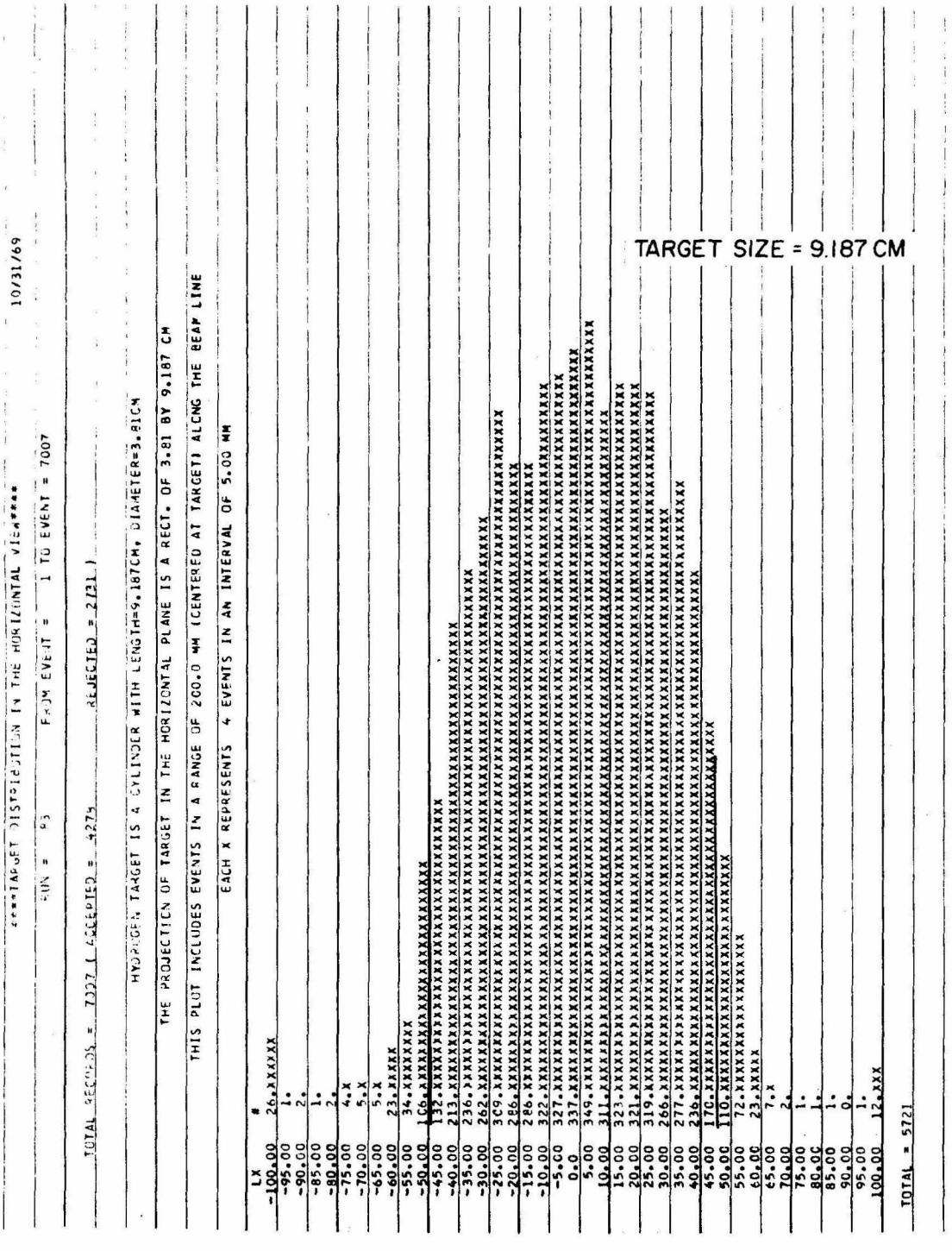

Figure 3.4 A Target distribution in the horizontal view.

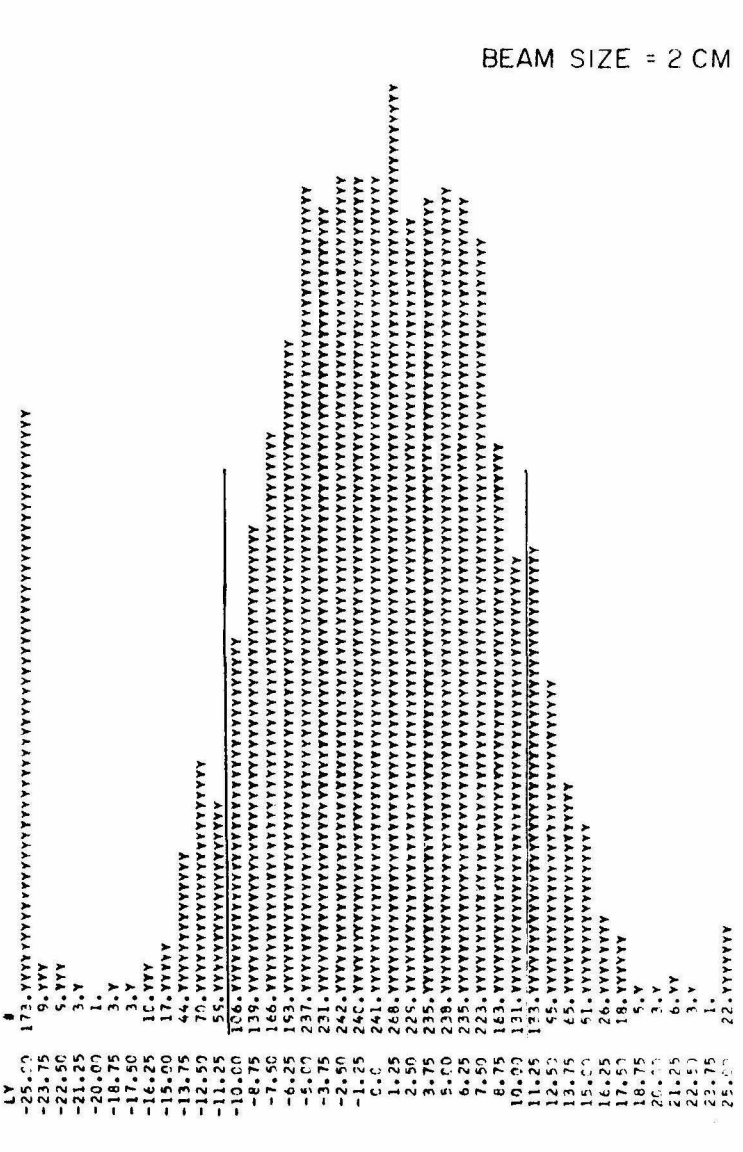

Figure 3.4 B Target distribution in the vertical view.

Figure 3.4-B) in the vertical view only showed a heavy concentration in a region of 2 cm. This is due to the bremsstrahlung beam which had a diameter of on the order of 2 cm. The events falling outside the extended target area (due to multiple scattering also) were suppressed as before.

A third test was to try to correlate the tracks before and after the bending magnet by matching their slopes. This was a safe check to make certain that both track segments physically belonged to the same track. In Figure 3.5, the difference of vertical slopes was plotted against the number of events. The half-width of the distribution was on the order of 0.02 (or 1.2 degrees). It was chiefly caused by the multiple scattering of the recoil proton in the carbon-plate range chamber. A maximum tolerable variation of vertical slopes was set to be 0.05 (or 3 degrees). All the badly matched events were removed from further tests.

The most important test of all was the proton momentum fitting. A wire orbiting calibration of the proton momentum in the bending magnet was done in the spring of 1968.[14] (See Appendix 6.11-A.) Three different magnetic field configurations were chosen to accept proton momenta in the range 800-1200 MeV, 600-1000 MeV, and 400-800 MeV/c, respectively. Given the incoming and the outgoing proton trajectories and the magnet configuration, the proton momentum could be calculated providing all the fitting parameters were within the precalibrated ranges.

Since the geometrical detection efficiency (see Figure 6.28 and 6.29) for most of the settings of the experiment covered a proton

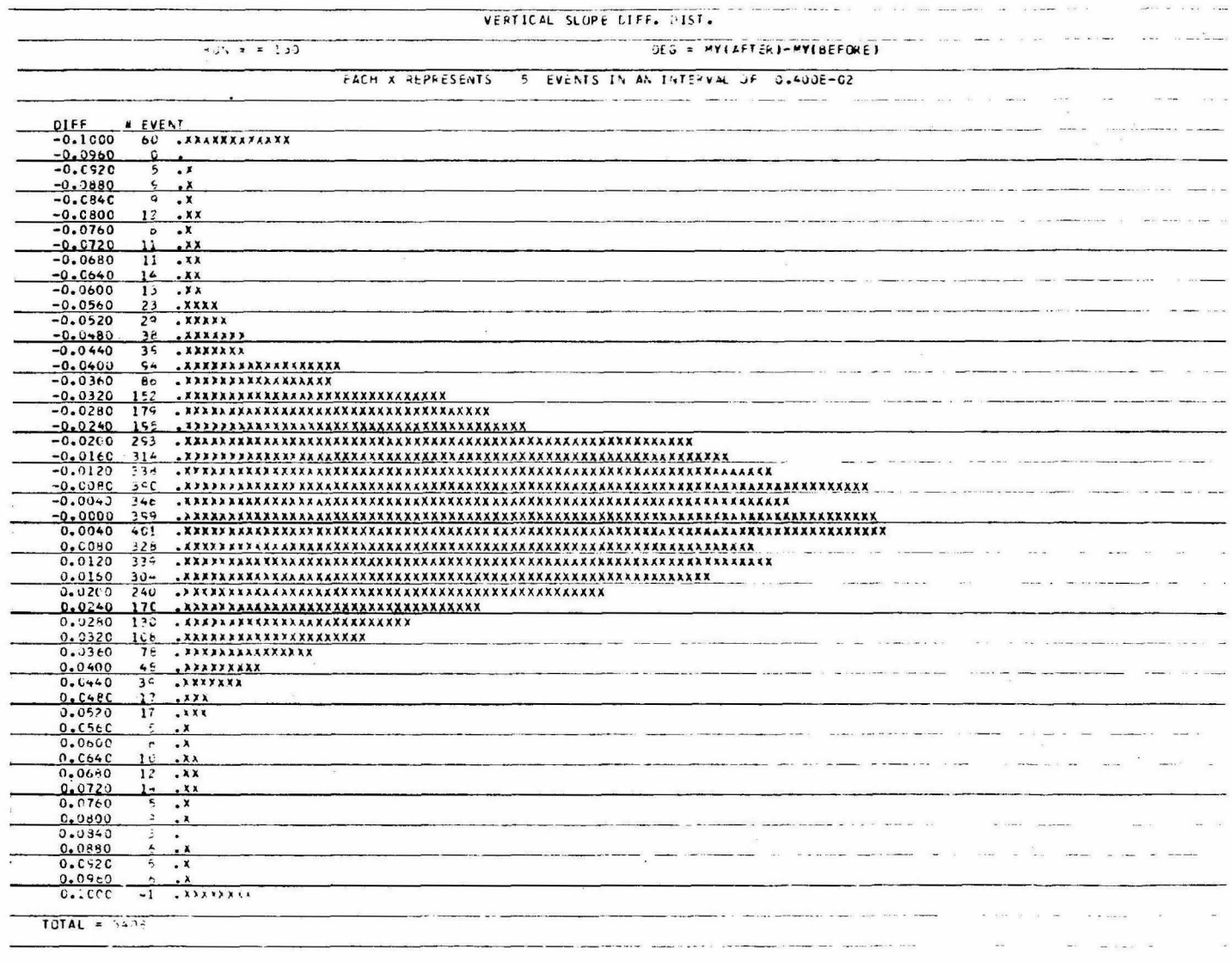

```
                                        VERTICAL SLOPE DIFF. DIST.

                    RUN # = 130                                   DEG = MY(AFTER)-MY(BEFORE)

                                 EACH X REPRESENTS    5  EVENTS IN AN INTERVAL OF  0.400E-02

  DIFF      # EVENT
 -0.1000   60  .XXXXXXXXXXXX
 -0.0960    0  .
 -0.0920    5  .X
 -0.0880    9  .X
 -0.0840    9  .X
 -0.0800   12  .XX
 -0.0760    6  .X
 -0.0720   11  .XX
 -0.0680   11  .XX
 -0.0640   14  .XX
 -0.0600   13  .XX
 -0.0560   23  .XXXX
 -0.0520   29  .XXXXX
 -0.0480   38  .XXXXXXX
 -0.0440   39  .XXXXXXX
 -0.0400   94  .XXXXXXXXXXXXXXXXXX
 -0.0360   86  .XXXXXXXXXXXXXXXXX
 -0.0320  152  .XXXXXXXXXXXXXXXXXXXXXXXXXXXXXX
 -0.0280  179  .XXXXXXXXXXXXXXXXXXXXXXXXXXXXXXXXXXX
 -0.0240  195  .XXXXXXXXXXXXXXXXXXXXXXXXXXXXXXXXXXXXXXX
 -0.0200  293  .XXXXXXXXXXXXXXXXXXXXXXXXXXXXXXXXXXXXXXXXXXXXXXXXXXXXXXXXXX
 -0.0160  314  .XXXXXXXXXXXXXXXXXXXXXXXXXXXXXXXXXXXXXXXXXXXXXXXXXXXXXXXXXXXXXX
 -0.0120  334  .XXXXXXXXXXXXXXXXXXXXXXXXXXXXXXXXXXXXXXXXXXXXXXXXXXXXXXXXXXXXXXXXXX
 -0.0080  390  .XXXXXXXXXXXXXXXXXXXXXXXXXXXXXXXXXXXXXXXXXXXXXXXXXXXXXXXXXXXXXXXXXXXXXXXXXXXXXX
 -0.0040  346  .XXXXXXXXXXXXXXXXXXXXXXXXXXXXXXXXXXXXXXXXXXXXXXXXXXXXXXXXXXXXXXXXXXXXX
 -0.0000  399  .XXXXXXXXXXXXXXXXXXXXXXXXXXXXXXXXXXXXXXXXXXXXXXXXXXXXXXXXXXXXXXXXXXXXXXXXXXXXXXX
  0.0040  401  .XXXXXXXXXXXXXXXXXXXXXXXXXXXXXXXXXXXXXXXXXXXXXXXXXXXXXXXXXXXXXXXXXXXXXXXXXXXXXXXX
  0.0080  328  .XXXXXXXXXXXXXXXXXXXXXXXXXXXXXXXXXXXXXXXXXXXXXXXXXXXXXXXXXXXXXXXXX
  0.0120  339  .XXXXXXXXXXXXXXXXXXXXXXXXXXXXXXXXXXXXXXXXXXXXXXXXXXXXXXXXXXXXXXXXXXX
  0.0160  304  .XXXXXXXXXXXXXXXXXXXXXXXXXXXXXXXXXXXXXXXXXXXXXXXXXXXXXXXXXXXX
  0.0200  240  .XXXXXXXXXXXXXXXXXXXXXXXXXXXXXXXXXXXXXXXXXXXXXXXX
  0.0240  170  .XXXXXXXXXXXXXXXXXXXXXXXXXXXXXXXXXX
  0.0280  130  .XXXXXXXXXXXXXXXXXXXXXXXXXX
  0.0320  106  .XXXXXXXXXXXXXXXXXXXXX
  0.0360   78  .XXXXXXXXXXXXXXX
  0.0400   49  .XXXXXXXXX
  0.0440   39  .XXXXXXX
  0.0480   17  .XXX
  0.0520   17  .XXX
  0.0560    5  .X
  0.0600    6  .X
  0.0640   10  .XX
  0.0680   12  .XX
  0.0720   14  .XX
  0.0760    5  .X
  0.0800    5  .X
  0.0840    3  .
  0.0880    6  .X
  0.0920    6  .X
  0.0960    6  .X
  0.1000   -1  .XXXXXXXX

 TOTAL = 5406
```

Figure 3.5 Distribution of the vertical slope difference.

momentum range wider than 400 MeV/c, only the upper part of the momentum spectrum would be used in most cases. Fortunately the events in this region always contained more interesting polarization information and were less contaminated by multi-pion production background.

The relative percentage of events which survived this momentum test ranged from 40% to 98%, depending on how well the prescribed 400 MeV/c momentum range fitted into the upper part of the detection efficiency curve. This test alone accounted for the largest single loss of events (see Figure 3.6).

The last test was to bias off events with reconstructed photon energy larger than the end point energy of the synchrotron (see Appendix 6.11-D for the reconstruction of the photon energy). Since an assumption was made during the calculation that only one single π^o was produced, the reconstructed photon energy originating from a Compton scattering event would appear to be higher than it actually was. Since Bremsstrahlung has a continuous energy spectrum nothing could be done about it if the reconstructed energy was still less than the end point energy. However, if it was larger than the end point energy, the event would be biased off on the grounds that it could not be the kind of reaction desired. Within the resolution of the experiment the material (mostly a 1/2" polyethylene plate and liquid hydrogen) between the target and the first wire chamber introduced a certain amount of multiple scattering which tended to move up the reconstructed Bremsstrahlung end point. The shift was estimated to be on the order of 15 MeV depending on the synchrotron end point itself, the exact amount of material in between, and the recoil proton angle with respect

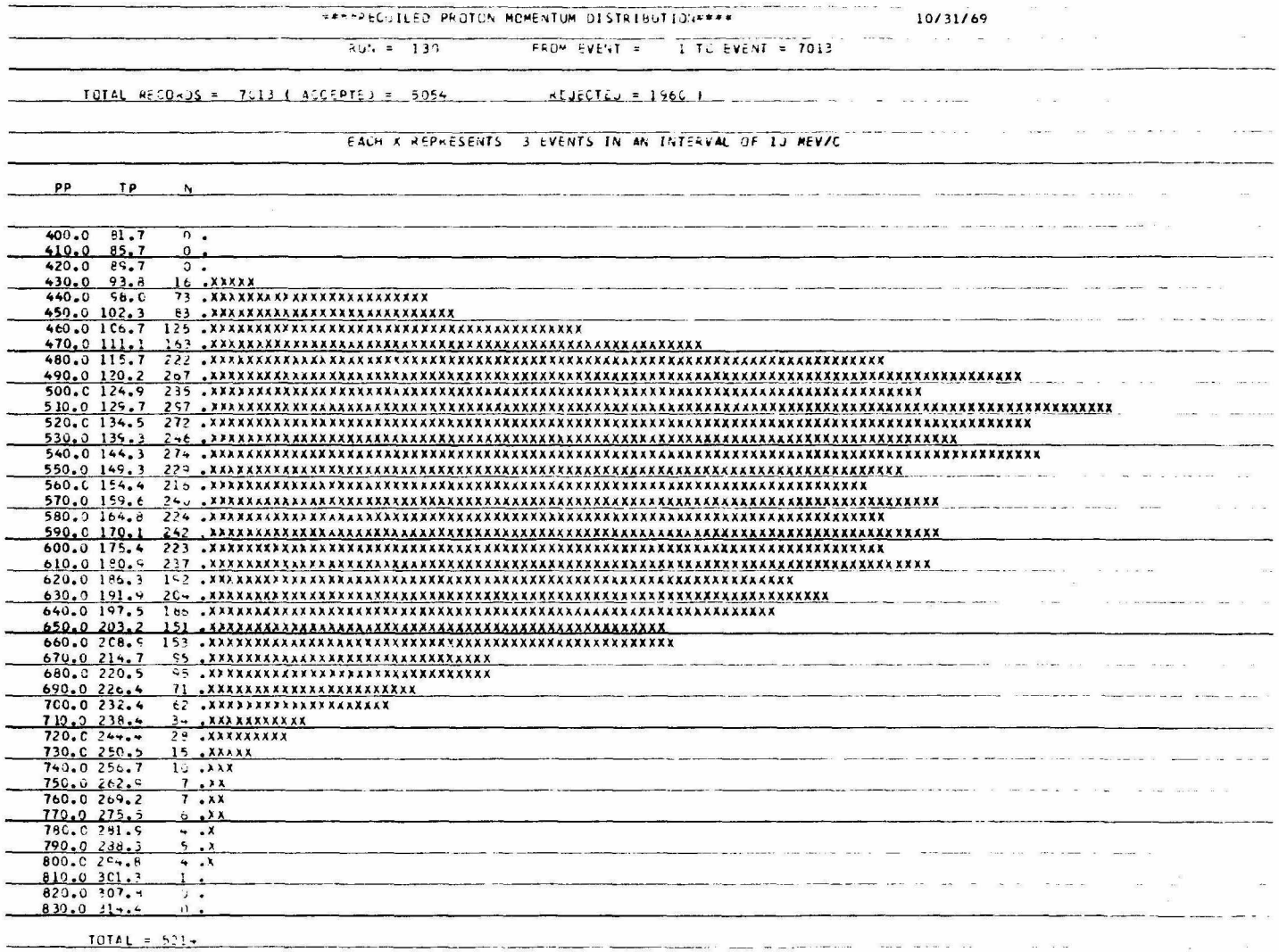

```
****RECOILED PROTON MOMENTUM DISTRIBUTION****                    10/31/69

                    RUN =  139          FROM EVENT =    1 TO EVENT = 7013

     TOTAL RECORDS =  7013 ( ACCEPTED =  5054          REJECTED = 1960 )

                    EACH X REPRESENTS  3 EVENTS IN AN INTERVAL OF 10 MEV/C

   PP      TP      N

 400.0   81.7      0 .
 410.0   85.7      0 .
 420.0   89.7      0 .
 430.0   93.8     16 .
 440.0   98.0     73 .
 450.0  102.3     83 .
 460.0  106.7    125 .
 470.0  111.1    163 .
 480.0  115.7    222 .
 490.0  120.2    207 .
 500.0  124.9    235 .
 510.0  129.7    297 .
 520.0  134.5    272 .
 530.0  139.3    246 .
 540.0  144.3    274 .
 550.0  149.3    229 .
 560.0  154.4    216 .
 570.0  159.6    240 .
 580.0  164.8    224 .
 590.0  170.1    242 .
 600.0  175.4    223 .
 610.0  180.9    237 .
 620.0  186.3    192 .
 630.0  191.9    204 .
 640.0  197.5    165 .
 650.0  203.2    151 .
 660.0  208.9    153 .
 670.0  214.7     99 .
 680.0  220.5     95 .
 690.0  226.4     71 .
 700.0  232.4     62 .
 710.0  238.4     34 .
 720.0  244.4     29 .
 730.0  250.5     15 .
 740.0  256.7     10 .
 750.0  262.9      7 .
 760.0  269.2      7 .
 770.0  275.5      6 .
 780.0  281.9      4 .
 790.0  288.3      5 .
 800.0  294.8      4 .
 810.0  301.3      1 .
 820.0  307.9      0 .
 830.0  314.4      0 .

           TOTAL = 5214
```

Figure 3.6 Reconstructed recoil proton momentum distribution.

to the incoming photon beam. The effect of the broadening of the end point energy was accounted for by extending the maximum allowable reconstructed photon energy to be the sum of the synchrotron end point energy and the uncertainty in energy introduced by the multiple scattering. Table 3.1 shows the major biases and their effects in a typical run.

3.3 Data Handling and Data Storage

All the preliminary data analysis up to this point was done off line on the Caltech IBM 360/75 using a comprehensive analysis program. The details of this program can be found in CTSL 48. (15) The input information, generated on line in a PDP-5 computer in the experiment, was stored on a 7 track magnetic tape. Each full size tape of 2400 feet contained up to 7200 records. Each record by itself contained the full information of an event, packed in low density (200 characters/inch or 100 PDP words/inch), consisting of 294 12-bit PDP words. Shorter tapes were occasionally used for special tasks. The format of a record is shown in Table 3.2. Altogether, about 100 full size tapes were generated to store nearly 600k events. It took the 360/75 between 4 to 6 minutes CPU time to process a full size tape for the preliminary data reduction. The first part of the program has to deal with the compatibility of the two computers. A 360 assembly language subroutine was written to translate the 7 track 12-bit information. The rest of the analysis program was written in the familiar FORTRAN 4 language. The output tape contained the events which survived all the tests. The record format of the output tape

TABLE 5.1: OVERALL ANALYSIS EFFICIENCY IN RUN 130

Total # Records Processed = 7013

Records Survived = 5054

	TEST	NTEST	NSURVIVE	% RELAT.
1.	PBL BIAS	7013.	6012.	85.73
2.	FRONT XZ	6012.	5952.	99.00
3.	FRONT YZ	5952.	5937.	99.75
4.	XZ TARGET	5937.	5912.	99.58
5.	YZ TARGET	5912.	5659.	95.72
6.	BACK XZ	5659.	5439.	96.11
7.	BACK YZ	5439.	5408.	99.43
8.	V. SLOPE MATCH	5408.	5309.	98.17
9.	MOMENTUM FIT	5309.	5214.	98.21
10.	KGAMMA RANGE	5214.	5054.	96.93

consisted of all the pertinent information needed for the further calculation of polarization. The format is shown in Table 3.3.

Since on the average only about 6% of the events survived all the tests in the preliminary analysis, the output tape (packed in high density of 800 characters/inch) was much more condensed than the input one. An effort was made to put together all the individual condensed output tapes belonging to the same geometry, same synchrotron end point, and same magnet configuration into a master tape. Seven master tapes were thus created; in case the original one was lost, a duplicate one was available. Altogether, there were 35k events with useful p-C scatter found in the preliminary data analysis. Seventy percent of the events were with pion center-of-mass production angle 93 +- 8 degrees and the remaining 30% events with 63 +- 8 degrees. This large amount of data enabled a statistically meaningful determination of the polarization parameters. As a by-product it gave a complete set of p-C scattering data in the experiment's kinematical region for future reference. (See Appendix 6.15.)

3.4 Calculation of Polarization

Conventionally the proton polarization is represented as a function of incoming photon energy and the center-of-mass pion production angle. An intuitive way to visually estimate the order of magnitude of polarization is by making a histograph of the number of events versus the azimuthal angle of the proton carbon scattering, Φ'_p (which is by definition the angle between the pion production plane and the p-C scattering plane), for all the events within a region

TABLE 3.2 INPUT TAPE FORMAT

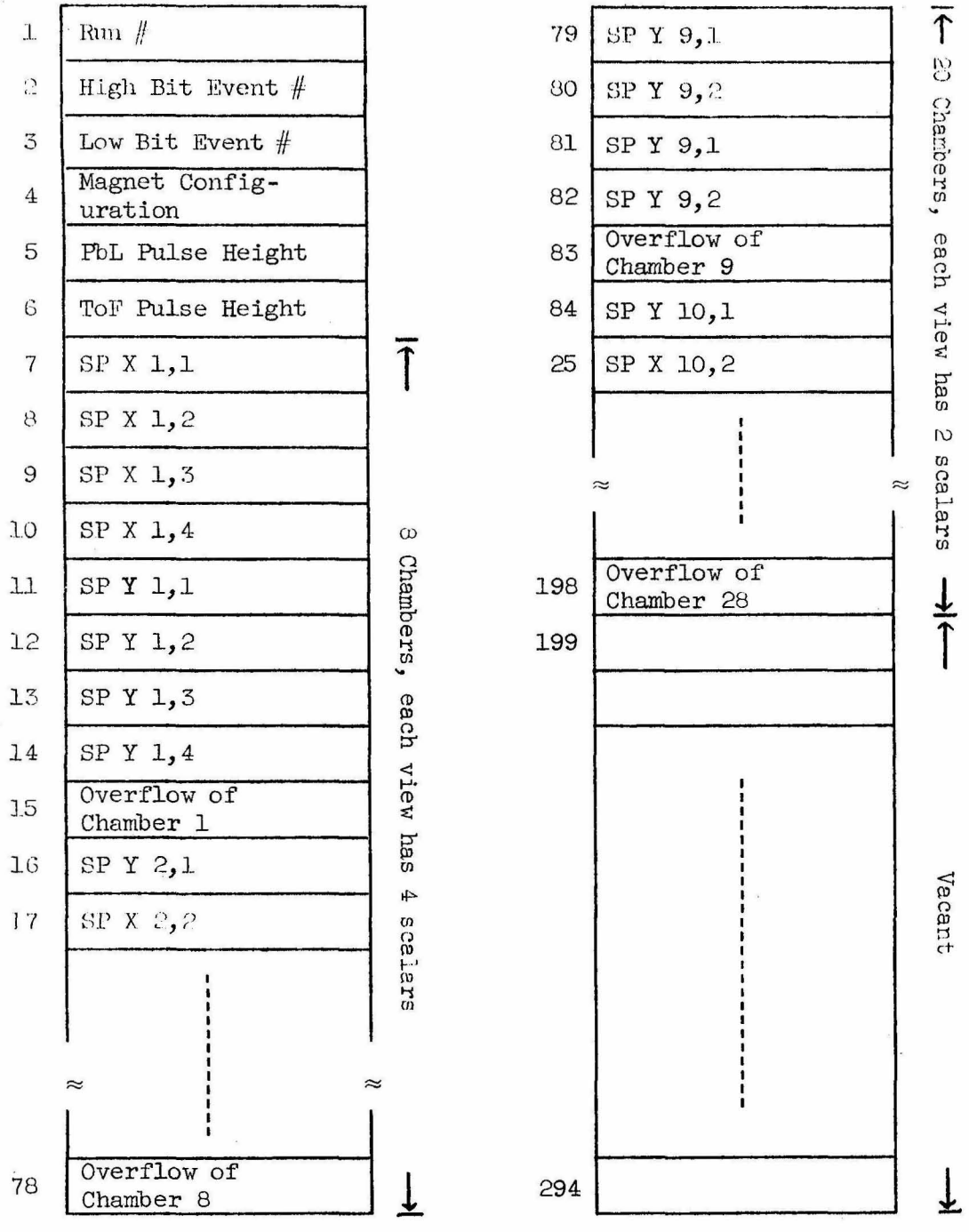

TABLE 3.3: OUTPUT TAPE FORMAT

1.	B_x (front)*1	17.	θ_π^{cm}
2.	M_x (front)	18.	$T_{p\ initial}$
3.	B_y (front)	19.	$\cos(\theta_{pr}^{lab})$
4.	M_y (front)	20.	$T_{p\ vertex}$
5.	B_x (back)	21.	θ_{pC}
6.	M_x (back)	22.	Φ_{pC}
7.	B_y (back)	23.	Inelasticity
8.	M_y (back)	24.	Energy Resolution
9.	B_x (scatter)	25.	Flag*2
10.	M_x (scatter)	26.	Chamber # of Proton Stoppage
11.	B_y (scatter)	27.	Vertex Module #
12.	M_y (scatter)	28.	Magnetic Configuration
13.	X_{vertex}	29.	PbL Pulse Height
14.	Y_{vertex}	30.	T.o.F. Pulse Height
15.	Z_{vertex}	31.	Run Number
16.	K_{photon}	32.	Event Number

*1 B_x, M_x (front) represent the intercept and slope of the fitted line in the front chambers

*2 Flag = 1 Scattered track leaves Range Chamber

Flag = 0 Scattered track stops inside Range Chamber

$$\left(k \pm \frac{\Delta k}{2} , \theta^*_\pi \pm \frac{\Delta\theta^*_\pi}{2}\right)$$

where k is the center of the photon energy bin, Δk the full width, θ^*_π is the center of pion center-of-mass production angular bin, $\Delta\theta^*_\pi$ its full width. Scattering theory [16] predicts

$$N(\Phi'_p) = N_o(1 + \overline{AP} \cos \Phi'_p) \qquad (3.4\text{-}1)$$

where N_o is a normalization constant; $\overline{AP}$ is the mean of the product of carbon analyzing power and the proton polarization in this bin. The value $\overline{AP}$ is actually the lower limit of polarization P, since the carbon analyzing power is always between -1 and +1. A very quick and powerful way of checking the reliability of the data is simply to see if the Fourier analysis of $N(\Phi'_p)$ shows any large non-zero coefficient, for a sin Φ'_p term is in direct contradiction to what is expected from equation (3.4-1) and therefore should be discredited.

Figure 3.7 shows two histographs of this nature. The functional dependence of a cos Φ'_p term is clearly indicated along with a crude estimation of the $\overline{AP}$.

However, no attempt has been made to try to disentangle $\bar{P}$ from $\overline{AP}$ because of the complexity involved. A much more sophisticated maximum likelihood method was used to calculate the polarization and its uncertainty. The maximum likelihood theorem is briefly described in Appendix 6.13.

In this experiment the likelihood function is

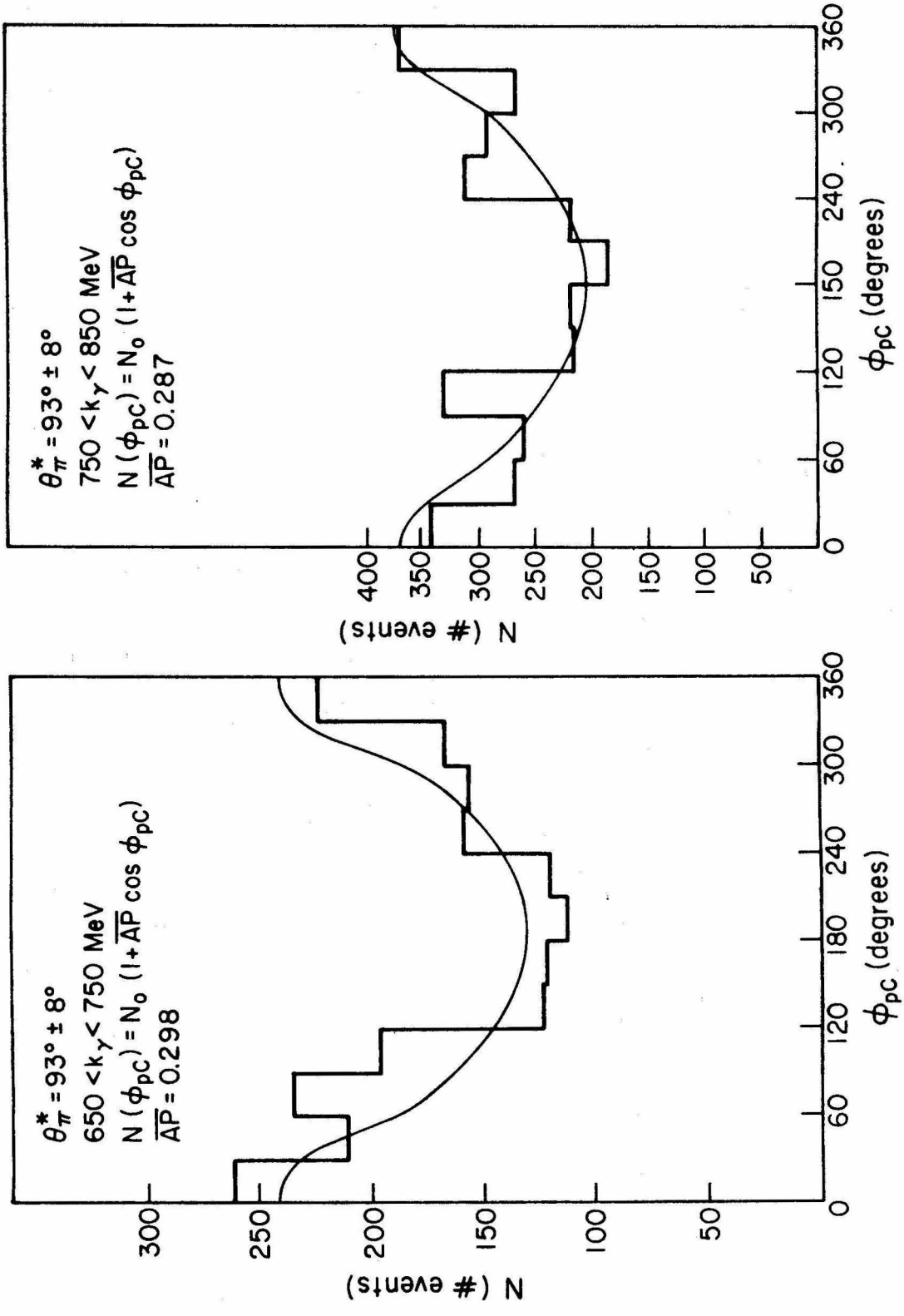

Figure 3.7 Distributions in Φ_{pC} for p-C scattered events.

$$L(P) = \prod_{i=1}^{n} [\sigma_o(T_{p_f}, \theta'_p)\, E_i(k, \theta^*_\pi)(1+A_i(T_{p_f}, \theta'_p, \Delta T_p) P \cos \Phi'_{p_i}] \qquad (3.4\text{-}2)$$

ΔT_p is the inelasticity of the p-C setting for the n events in the (k, θ^*_π) bin. T_{p_f} is the proton kinetic energy just before the p-C scattering, θ'_p and Φ'_p are the polar and azimuthal angles of the scattering in the laboratory system, A_i is the analyzing power of carbon, σ_o is the unpolarized cross section, E_i the single pion production detection efficiency. (See Appendix 6.16.) Since neither σ_o nor E_i are functions of the polarization P, equation (3.4-2) implies an equivalent likelihood function

$$L(P) = \prod_{i=1}^{n} [(1 + A_i(T_{p_f}, \theta_p, \Delta T_p)\, P \cos \Phi'_{p_i})]. \qquad (3.3\text{-}3)$$

The maximum likelihood theorem states that at the limit $n \to \infty$ the likelihood function L(P) approaches a gaussian. Therefore the best fitted value of polarization is at $P = P^*$ where the condition

$$\frac{\partial}{\partial P}[L(P)]_{P=P^*} = 0 \qquad (3.4\text{-}4)$$

is satisfied. The uncertainty of the polarization is defined by

$$\Delta P = \left\{ - \frac{\partial^2}{\partial P^2} \ell n(L(P)) \right\}^{-\frac{1}{2}}_{P=P^*} \qquad (3.4\text{-}5)$$

In this experiment, because of the large amount of useful events, the gaussian approximation was always a good one (see Figure 3.8).

3.5 Calculation of Single Pion Photoproduction Differential Cross Section

As a by-product and as a check of a polarization experiment, it is always useful to estimate the π^o cross section in the kinematical region covered and check the results against the well established data. Good agreement of the results is an assurance that the apparatus was working correctly in all details and as a whole. About 20% of the original 600k events were used to perform an estimation of the single π^o cross section. It covered the identical kinematical regions of the polarization measurements, namely θ^*_π = 63 +- 8 degrees, $650 \leq k \leq 1350$ MeV and θ^*_π = 93 +- 8 degrees, $650 \leq k \leq 1350$ MeV. The cross section in this region, specifically the region of the second and third resonances, has been well reported, [1] namely the region of the second and the third resonances.

To determine the photon energy, k, the first step is to evaluate the kinetic energy of the recoil proton by using the wire orbiting calibration method (see Appendix 6.11-A). Once the kinetic energy, T_p, has been obtained, one can easily calculate the photon energy by using the laws of conservation of energy and momentum assuming that a single π^o was produced. (For the details, see Appendix 6.11-D.) Figure 6.17 shows a typical raw k distribution of the experiment. By unfolding the k distribution with the geometrical detection efficiency and taking into account the systematic correc-

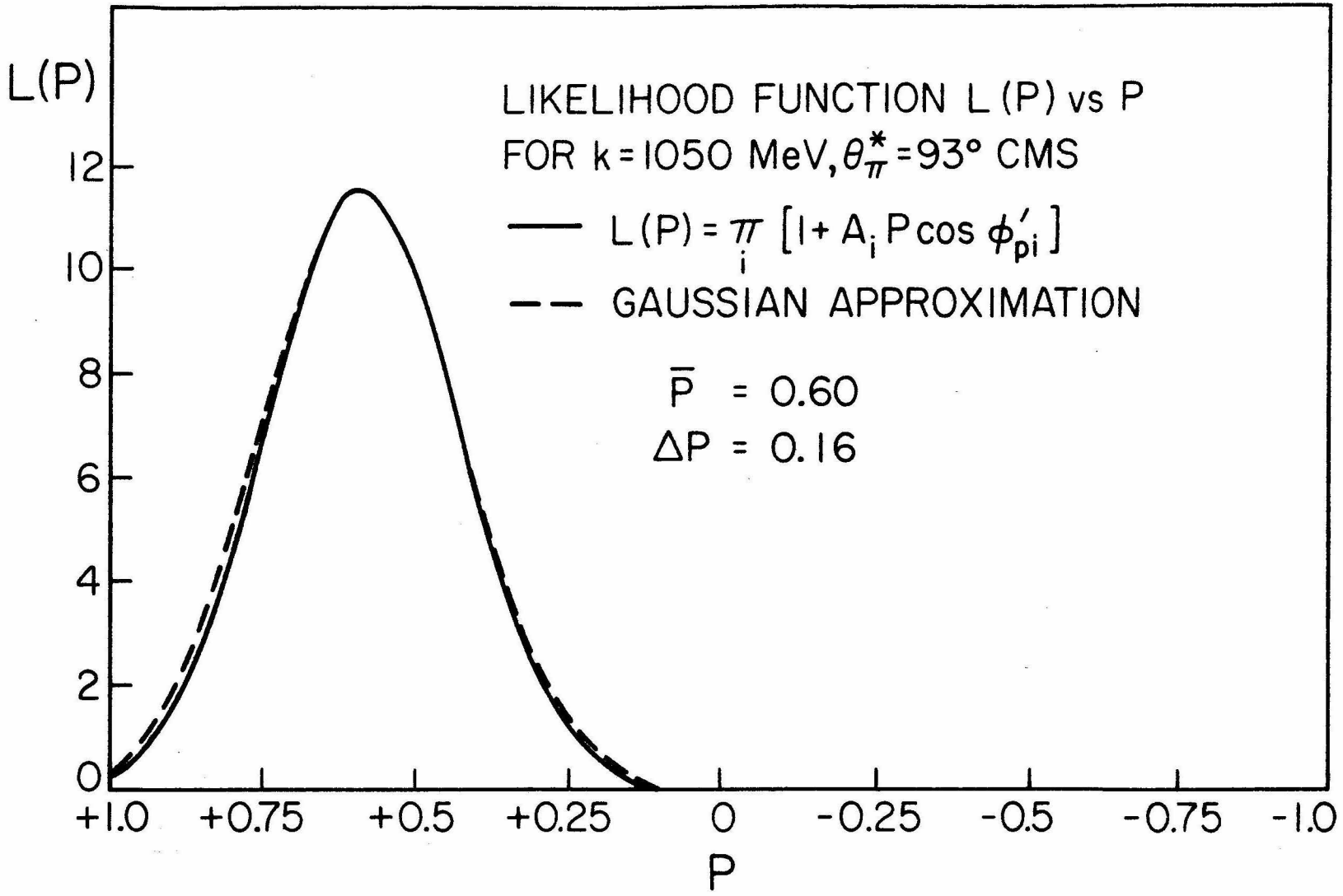

Figure 5.3 Likelihood function L(P) vs. P.

tions one is able to calculate the π^o differential cross section.

In calculating a cross section one must account for all events. Every event with a recognizable track in the back chambers was accepted. It is also important that the systematic corrections should be made prior to the calculation. Even though each effect is rather small, the combined effect could be considerable. Table 3.4 lists the systematic effects for the cross section calculation in the region $\theta^*_\pi = 93^o$ +- 8^o, $650 \leq k \leq 1350$ MeV.

The general method used in calculating the cross section once all systematic corrections were completed was modified from that of Section V-A of Reference 17 . For completeness the relevant formula is reproduced here.

The total number of counts at a given incident photon energy bin $k \pm \Delta k/2$ is a summation of contributions from single π^o photoproduction, Compton scattering and 2 π^o photoproduction (contributions from three or more π^o productions are believed to be negligible). The formula is

$$C(k) = \frac{4\ \pi\ \alpha\ \beta\ N_p\ W\ b\ \Delta k\ B(k)}{E_o k} \left(\overline{\frac{d\sigma}{d\Omega}}_\pi \epsilon_\pi(k) + \overline{\frac{d\sigma}{d\Omega}}_{2\pi} \epsilon_{2\pi}(k) + \overline{\frac{d\sigma}{d\Omega}}_{\gamma p} \epsilon_{\gamma p}(k) \right) \qquad (3.5\text{-}1)$$

where

$C(k)$ = number of events experimentally generated in the interval k +- $\Delta k/2$

$\epsilon(k)$ = geometrical detection efficiency of event initiated from photon of energy k

TABLE 3.4: SYSTEMATIC EFFECTS*

Effect	Loss % in $\theta_\pi^* = 93\pm8^\circ$	Loss % in $\theta_\pi^* = 63\pm8^\circ$
Spark Chamber Dead Time	0.4	0.4
SP-1	Negligible	Negligible
SP-2	Negligible	Negligible
SP-3	Negligible	Negligible
Veto	0.4	3.0
PbL	Negligible	Negligible
Photon Pre-Conversion**	3.5	3.0
Shower Counter Inefficiency***	5.0	3.5
Proton Counter Inefficiency	Negligible	Negligible
Miscellaneous	1.5	1.5
Total Corrections	10.8	11.4

* Systematic effects do not include inefficiency due to analysis. A typical analysis efficiency table can be found in Table 3.1.

** Photons which convert in the target walls or in air before reaching the veto counter are lost.

*** Pulse height requirement introduced in the analysis is responsible for this inefficiency. The electronic bias was set low enough so that it introduced negligible inefficiencies.

E_o = synchrotron end point energy in MeV

α = systematic corrections, all those of Table 3.4

β = overall data analysis efficiency (as those of Table 3.1)

N_p = number of protons in target per cm^2 ($3.9176 \times 10^{23}/cm^2$)

W = quantameter constant ($=1.097 \times 10^{13}$ MeV/BIP; see also Appendix 6.1)

b = number of BIPs

Δk = energy bin (= 25 MeV)

B(k) = The bremsstrahlung function for 0.193 radiation length of tantalum target (Z = 73)

k = Energy of the center of photon energy bin in MeV

The geometrical detection efficiencies of different reactions are given in Figure 6.28 and Figure 6.29. The differential cross sections of proton Compton scattering are shown in Figure 2.4 and Figure 2.5. Although the cross section of 2 π^o production is not readily available, an upper limit of 18 μb total cross section was used for all the background estimation (see Appendix 6.17).

The evaluation of $\overline{\frac{d\sigma}{d\Omega}}_{\pi}$ was made after completing the background subtraction. The results of π^o photoproduction cross section agreed very well with known values (for the results, see Section 4.2).

4. RESULTS

4.1 Proton Polarization

This experiment was intended to measure the recoil proton polarization in π^o photoproduction with synchrotron end point up to 1375 MeV, at pion C. M. production angles, θ^*_π, of 60 and 90 degrees. However, the actual θ^*_π distribution of the useful events (see Figure 4.2 and Figure 4.4) showed that the geometric centers were actually 63^o and 93^o respectively. The k distributions for the events containing useful p-C scatters are displayed in Figure 4.1 and Figure 4.3. The events with k > 1150 MeV in $\theta^*_\pi = 93 \pm 8^o$ were scarce; they were further reduced in the evaluation of the carbon analyzing power (see Appendix 6.14). The corresponding polarization points are therefore associated with large error bars. They are presented for the sake of completeness. The data are presented in Figure 4.5, Figure 4.6, Table 4.1, and Table 4.2.

Although Bloom's experiment [6] at $\theta^*_\pi = 60^o$ covered energies as high as k = 1450 MeV, our experiment provided a first check on his results with better statistics and finer energy binning. (50 MeV in this experiment as compared with 100 MeV in the previous one.)

For the data taken around $\theta^*_\pi = 60^o$, the magnet was operated at configuration 2 most of the time; it only accepted the recoil protons with momentum between 600 MeV/c and 1000 MeV/c. The photon energy, k, associated with such recoil protons usually exceeded 900 MeV. Therefore, the lower limit of photon energy at $\theta^*_\pi = 60^o$ polar-

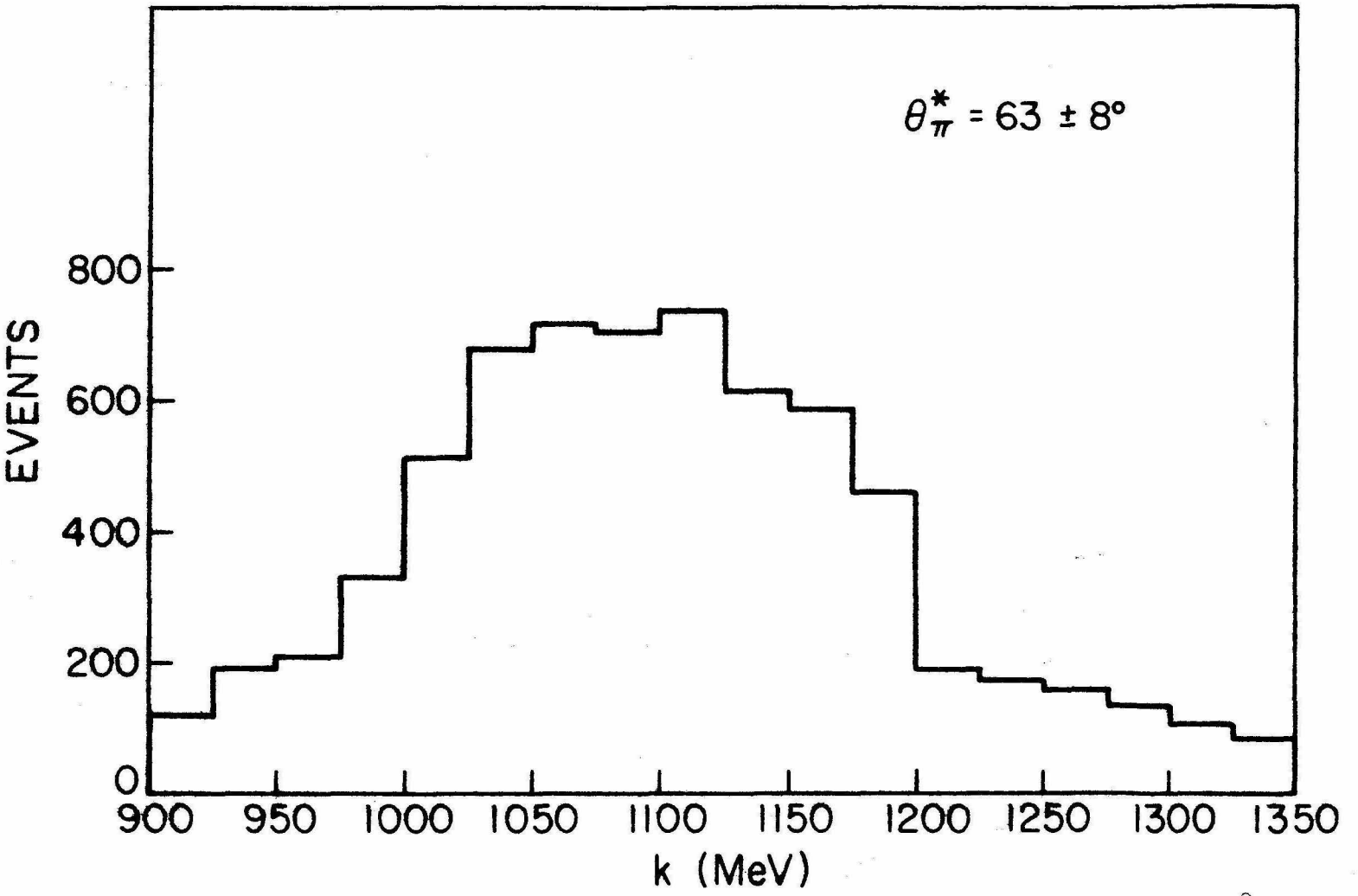

Figure 4.1 k distribution for scattered events in the region $\theta^*_\pi = 63 \pm 8^\circ$.

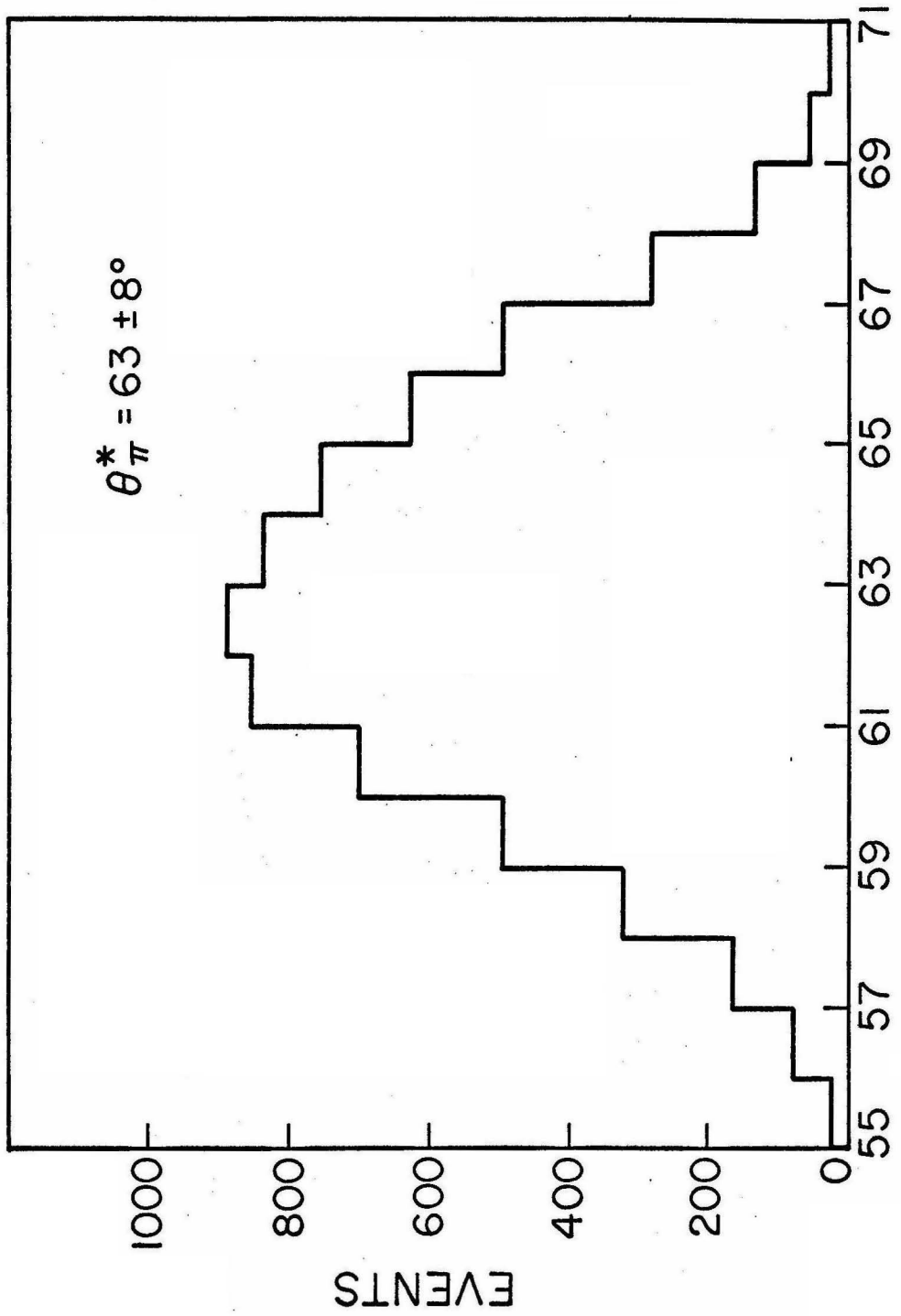

Figure 4.2 Distribution of θ^*_π in the region $\theta^*_\pi = 63 \pm 8^\circ$.

TABLE 4.1 POLARIZATION DATA AT $\theta_{\pi}^{*} = 63 \pm 8^{o}$.

k(MeV)	$P_{\perp}$	$P_{//}$
925	0.15 ± 0.24	0.25 ± 0.24
975	-0.01 ± 0.16	0.01 ± 0.18
1025	0.00 ± 0.11	0.06 ± 0.12
1075	0.07 ± 0.10	-0.04 ± 0.11
1125	0.16 ± 0.11	-0.01 ± 0.11
1175	0.37 ± 0.12	0.05 ± 0.13
1225	0.10 ± 0.20	-0.44 ± 0.21
1275	0.56 ± 0.25	0.34 ± 0.25
1325	0.54 ± 0.29	-0.29 ± 0.33

ization points was 900 MeV.

However, there were still about 25% events at θ^*_π around 60° that were taken in magnet configuration 3 (400 MeV/c < p_p < 800 MeV/c). A large portion of the photon energy range associated with such a proton momentum range lay below 900 MeV. As a consequence, we were able to abstract enough events to do a differential cross section estimate, but not enough to do a polarization estimate.

The results at $\theta^*_\pi = 63 \pm 8^\circ$ generally agreed well with those of Bloom's. Our results did not show a zero crossing in the region between k = 900 MeV and k = 1100 MeV as did Bloom's experiment, as predicted earlier by Beder. (2) The polarization value at k = 925 MeV (negative in Bloom's experiment, but positive in this experiment) in fact agreed with the 66 Stanford data.

The finer energy binning revealed an interesting structure at k = 1175, 1225, 1275 MeV. whose combined effect agreed excellently with those of Bloom's. The numerical results of this experiment and those of other related experiments are presented in Table 4.1.

For the data taken around $\theta^*_\pi = 93 \pm 8^\circ$, the momentum range of the wire orbiting calibration fitted well into the kinematical range. Therefore we actually were able to use the events with k as low as 650 MeV in the cross section as well as the polarization estimation.

At $\theta^*_\pi = 93 \pm 8^\circ$, our results again agreed well with those of other experiments in the region of overlap (below k = 1000 MeV). The agreement between this experiment and the 67 Stanford data is excellent.

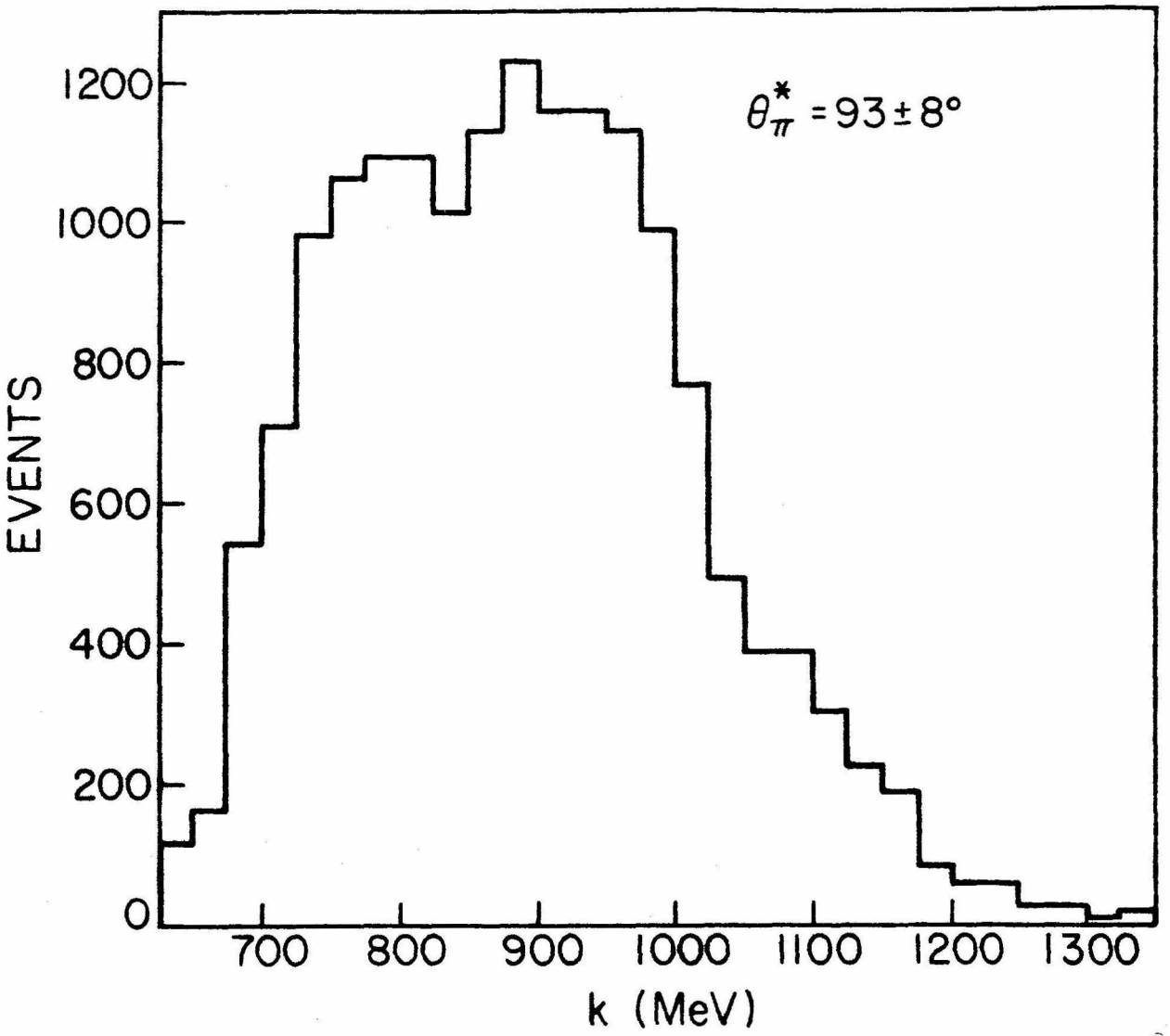

Figure 4.3 k Distribution for scattered events in the region $\theta_\pi^* = 93 \pm 8°$.

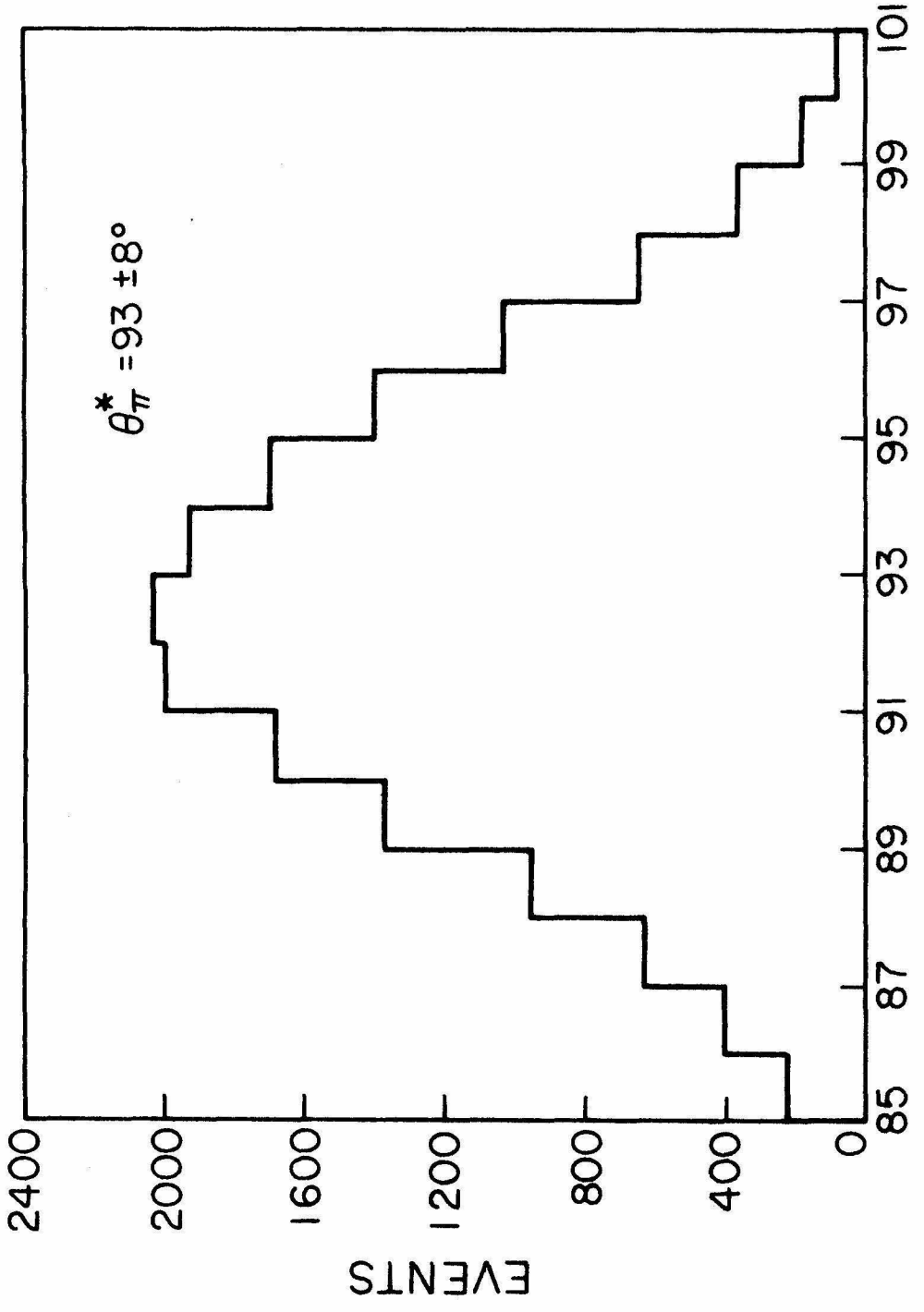

Figure 4.4 Distribution of θ^*_π in the region $\theta^*_\pi = 93° \pm 8°$.

TABLE 4.2 POLARIZATION DATA AT $\theta_\pi^* = 93 \pm 8^\circ$.

k(MeV)	$P_\perp$	$P_{//}$
650	-0.66 ± 0.23	0.02 ± 0.23
700	-0.80 ± 0.09	-0.40 ± 0.10
750	-0.69 ± 0.07	-0.18 ± 0.07
800	-0.47 ± 0.07	-0.04 ± 0.07
850	-0.26 ± 0.08	0.00 ± 0.08
900	-0.29 ± 0.09	0.02 ± 0.09
950	-0.54 ± 0.10	0.15 ± 0.11
1000	-0.42 ± 0.13	0.05 ± 0.14
1050	-0.67 ± 0.20	0.32 ± 0.20
1100	-0.56 ± 0.26	0.07 ± 0.26
1150	-0.49 ± 0.36	0.40 ± 0.41
1200*	0.25 ± 0.60	0.10 ± 0.57
1250*	-0.52 ± 0.69	0.53 ± 0.73

*These settings yielded very few events. We present the results for completeness only - they are essentially useless for fitting purposes.

A consistency check was made to make certain that no appreciable systematic asymmetry was introduced during the data acquisition or during data reduction. For every polarization point, $P_{\perp}$, obtained its corresponding polarization on the production plane, $P_{//}$, was also calculated according to equation 3.4-3 except replacing $\cos \Phi'_p$ by $\sin \Phi'_p$. The law of conservation of parity requires that $P_{//}$ should be zero. The calculated $P_{//}$ (included in Table 4.1 and Table 4.2) confirmed this assumption quite well.

By dividing all the data into four angular bins, namely $\theta^*_\pi = 59 \pm 4^o$, 67 ± 4^o, 89 ± 4^o and 97 ± 4^o, we were able to calculate the polarization as a function of pion production angles in the CMS. The results showed a strong angular dependence for the region covered. The trend of the angular variation from 59 ± 4^o to 67 ± 4^o seemed to agree with Bloom's finding that the higher the pion production angle, the larger the polarization. Figures 4.7, 4.8 and Table 4.3 display the finely binned data. The strong angular dependence of the polarization values appears to be present on the entire energy range of this experiment.

Errors quoted are purely statistical, as obtained from the maximum likelihood method. Systematic errors of the experiment are small, the shifts thus introduced are believed to be insignificant. The errors due to the uncertainties of the carbon analyzing power (good to 15%) were estimated to be less than 30% of the quoted error bars.

In order to estimate the worst possible correction due to the presence of the 7% background events, we assumed that all of

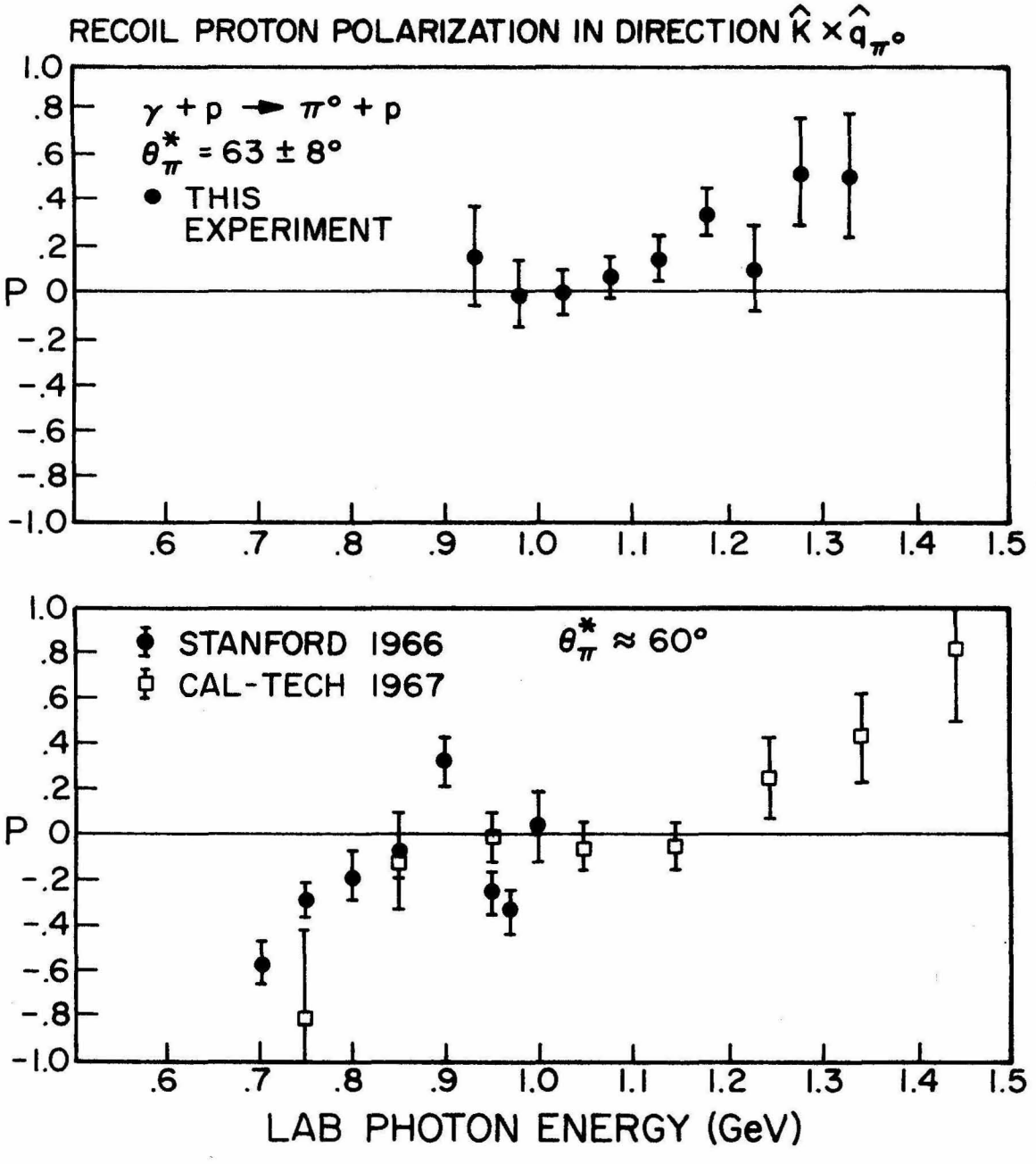

Figure 4.5 Polarization data at $\theta^*_\pi = 63 \pm 8^\circ$.

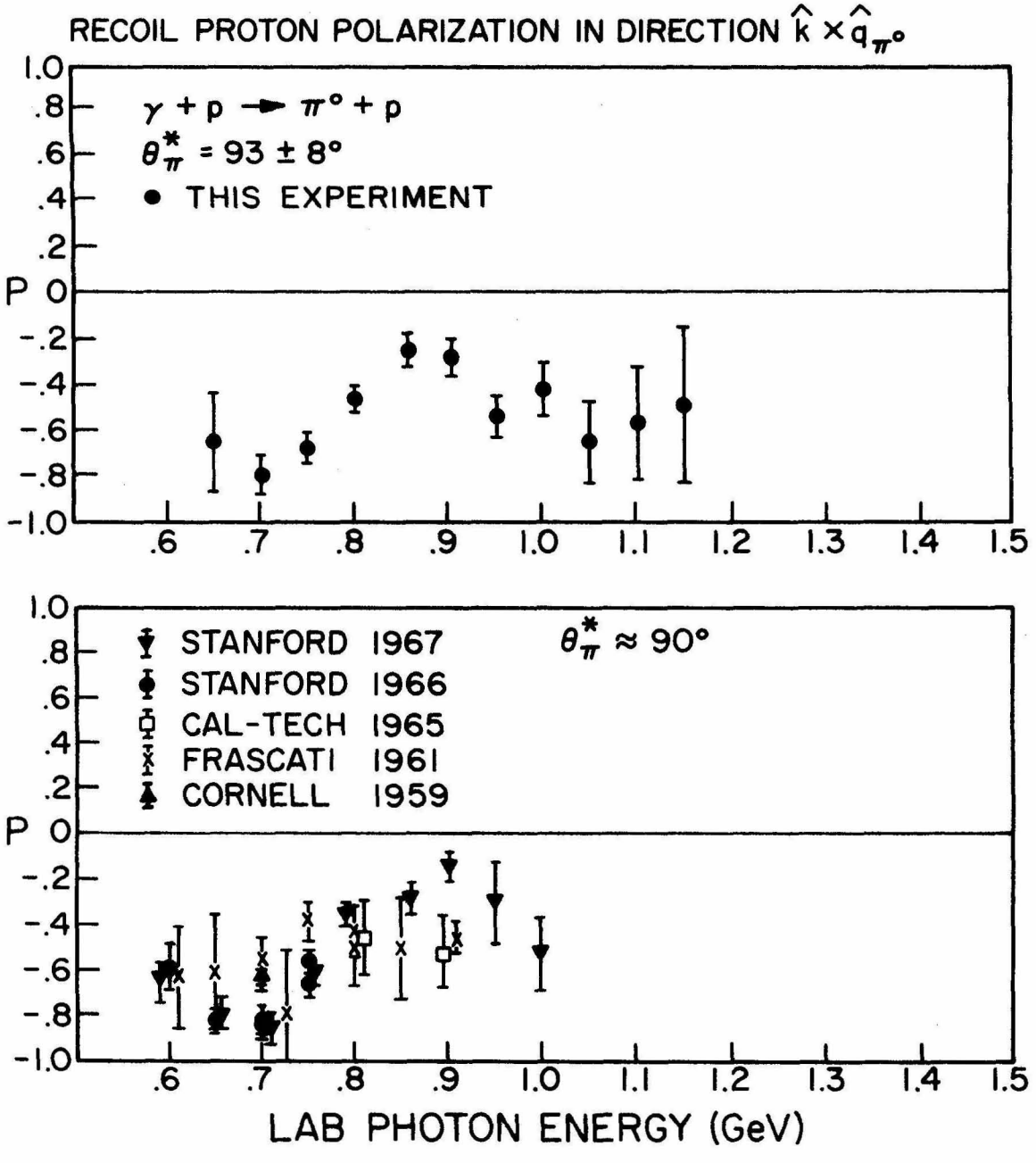

Figure 4.8 Polarization data at $\theta^*_\pi = 93 \pm 8°$.

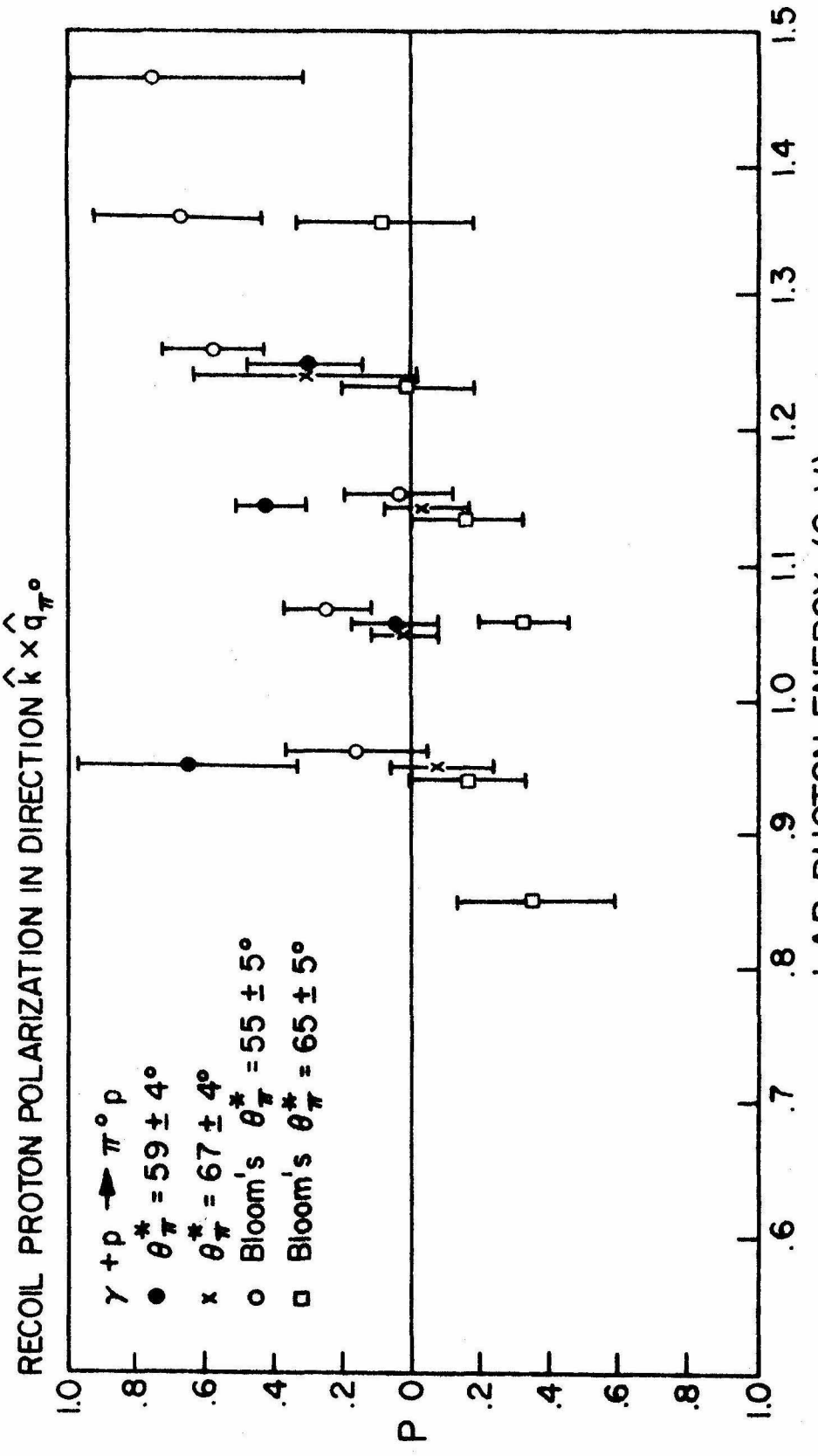

Figure 4.7 Polarization data at $\theta^*_\pi = 59 \pm 4^\circ$ and $\theta^*_\pi = 67 \pm 4^\circ$.

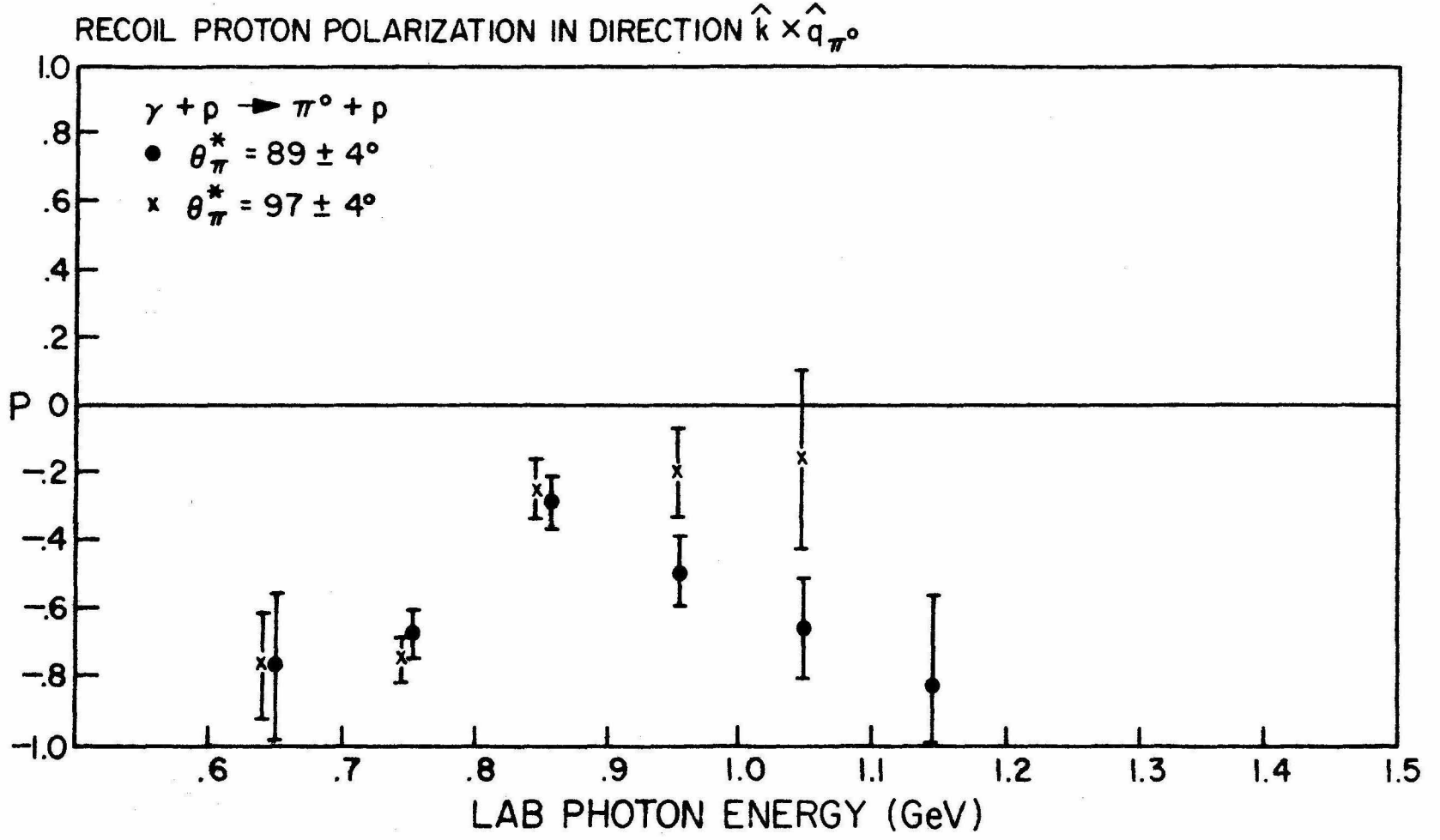

Figure 4.5 Polarization data at $\theta^*_\pi = 89 \pm 4°$ and $\theta^*_\pi = 97 \pm 4°$.

TABLE 4.3: POLARIZATION DATA AT $\theta^*_\pi = 59^\circ, 67^\circ, 89^\circ, 97^\circ$

k(MeV)	$P_\perp$			
	$\theta^*_\pi = 59 \pm 4^\circ$ $< \theta^*_\pi > = 60.7$	$\theta^*_\pi = 67 \pm 4^\circ$ $< \theta^*_\pi > = 65.3$	$\theta^*_\pi = 89 \pm 4^\circ$ $< \theta^*_\pi > = 90.3$	$\theta^*_\pi = 97 \pm 4^\circ$ $< \theta^*_\pi > = 95.4$
650			-0.78 ± 0.22	-0.78 ± 0.16
750			-0.68 ± 0.08	-0.75 ± 0.07
850			-0.29 ± 0.08	-0.26 ± 0.09
950	0.66 ± 0.33	-0.08 ± 0.15	-0.48 ± 0.09	-0.22 ± 0.13
1050	0.05 ± 0.12	0.03 ± 0.10	-0.65 ± 0.16	-0.17 ± 0.28
1150	0.42 ± 0.10	-0.04 ± 0.13	-0.81 ± 0.27	
1250	0.29 ± 0.18	0.32 ± 0.33		

$< >$ = Geometrical center of the bin

them were completely polarized in the same direction; the polarization thus found showed an average change of 40% of the quoted error bars.

4.2 Single Pion Photoproduction Differential Cross Section

Single π^o photoproduction cross section at $\theta^* = 63 \pm 8^o$ and $\theta^*_\pi = 93 \pm 8^o$ in the energy region $650 < k < 1350$ MeV were also determined as a by-product of this polarization experiment. Their good agreement with the known values could serve an indication that the whole system worked correctly in all details. The results are presented in Figure 4.9, Figure 4.10, and Table 4.4.

The energy resolution was on the order of 15 MeV which helped to explain the low peak cross section value at the second resonance at $\theta^*_\pi = 63 \pm 8^o$. The effect of the second and the third resonances appeared at the right energy for both $\theta^*_\pi = 63^o$ and $\theta^*_\pi = 93^o$.

The cross sections were evaluated according to the scheme outlined in Section 3.5. About 20% of the original 600 k events were used for this estimate. Due to the large number of data available, the errors introduced by pure statistics σ_{stat}, were small. The total percentage error σ_{tot}, quoted was defined as follows:

$$\sigma_{tot} = \sqrt{\sigma_{stat}^2 + \sigma_{M.C.}^2 + \sigma_{S.E}^2} \quad ;$$

$\sigma_{M.C.}$ is the percentage accuracy of the Monte-Carlo detection efficiency; $\sigma_{S.E.}$ is the percentage uncertainty associated with the systematic errors of the experiment. The combined effect seldom exceeded 10%. The most deviation these data could possibly suffer is an overall normalization constant because of the nature of the

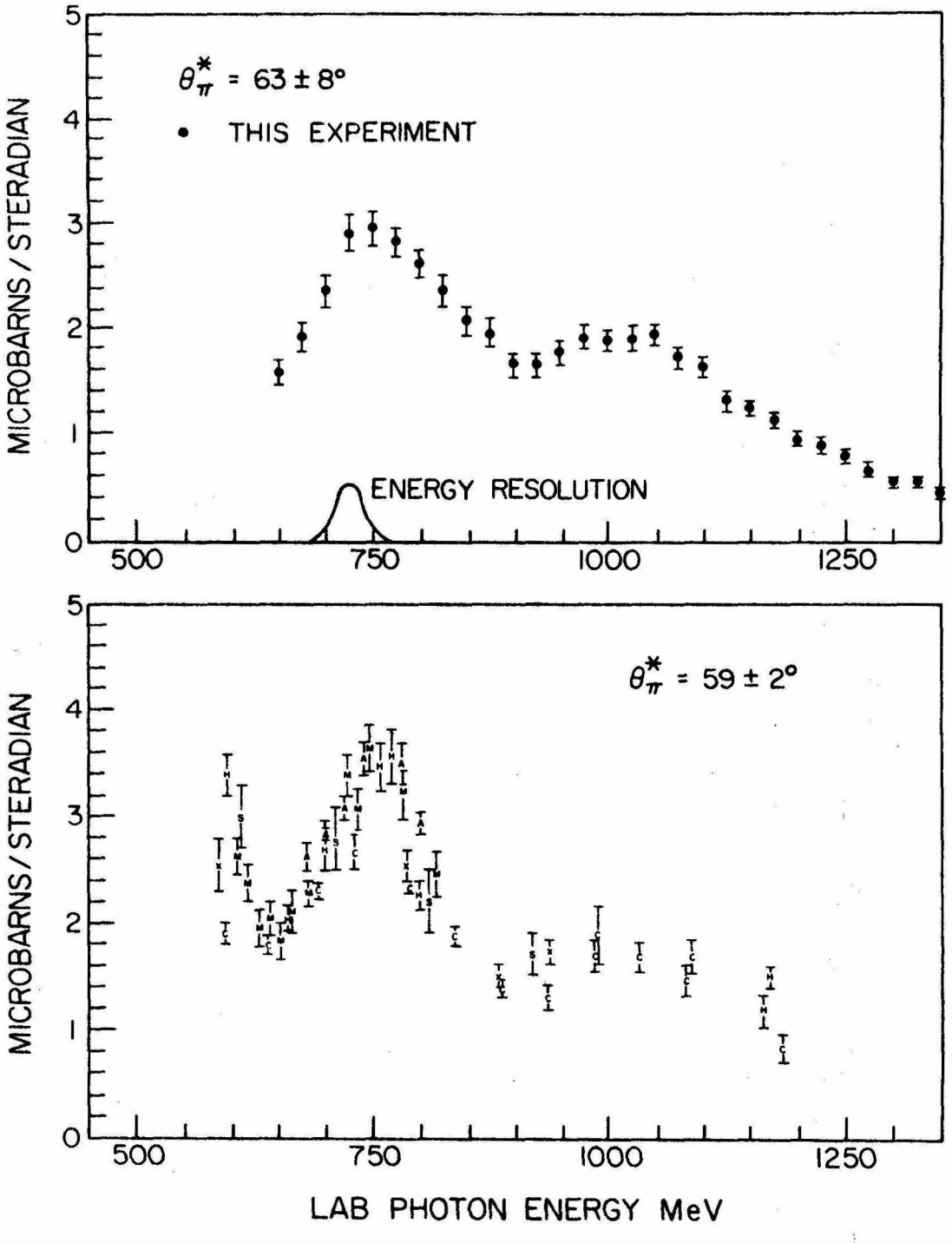

Figure 4.9 π^o differential cross section at $\theta_\pi^* = 63 \pm 8^o$.

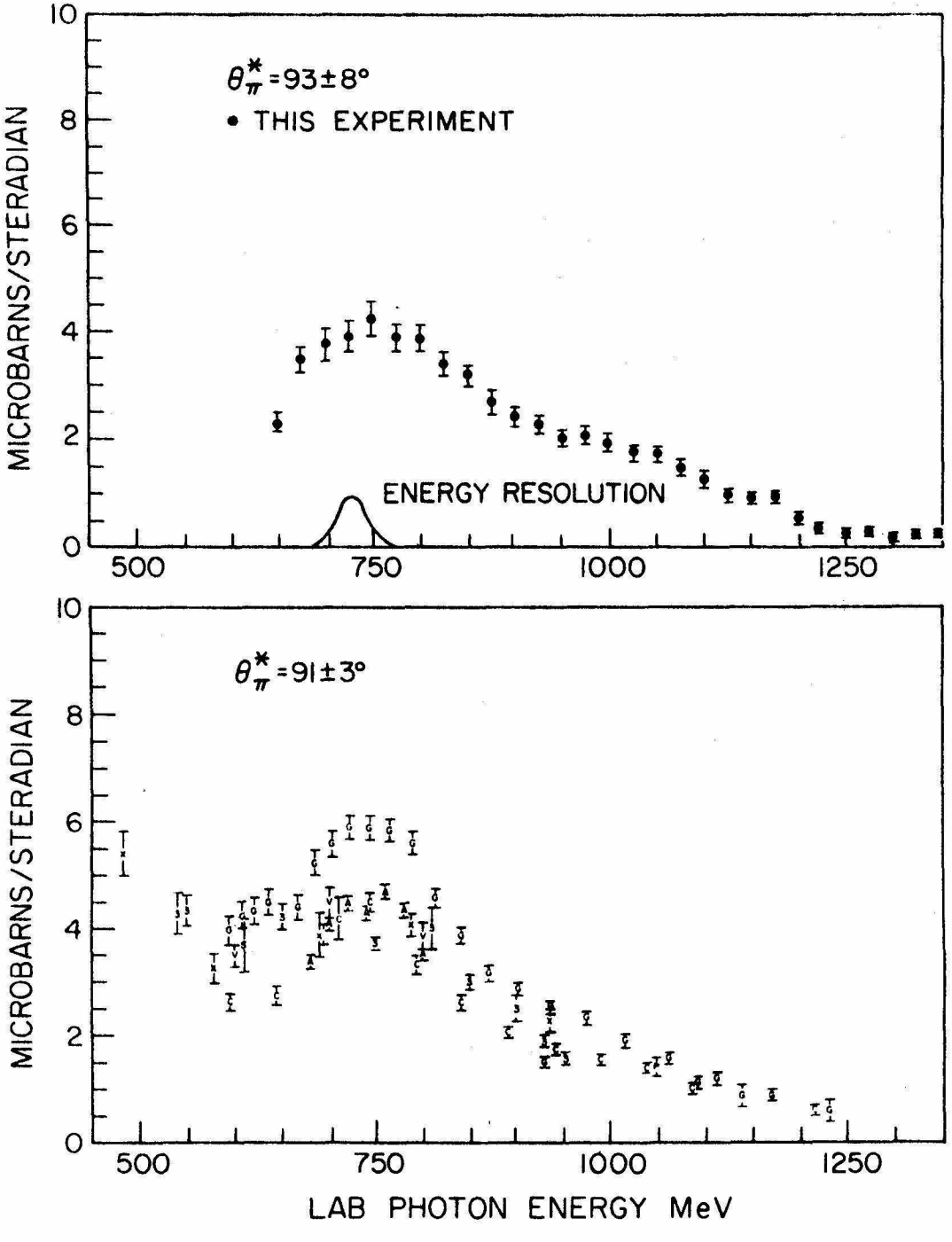

Figure 4.10 π^o differential cross section at $\theta_\pi^* = 93 \pm 8^o$.

TABLE 4.4 DIFFERENTIAL CROSS SECTION DATA AT $\theta^*_\pi = 63 \pm 8^\circ$ AND $\theta^*_\pi = 93 \pm 8^\circ$.

k(MeV)	$\frac{d\sigma}{d\Omega}_{63^\circ}$ ($\mu b/Sr$)	$\frac{d\sigma}{d\Omega}_{93^\circ}$ ($\mu b/Sr$)
650	1.66 ± 0.12	2.33 ± 0.19
675	1.90 ± 0.13	3.42 ± 0.26
700	2.46 ± 0.16	3.82 ± 0.29
725	2.84 ± 0.18	3.96 ± 0.29
750	2.91 ± 0.18	4.27 ± 0.31
775	2.77 ± 0.17	3.93 ± 0.29
800	2.62 ± 0.16	3.86 ± 0.27
825	2.33 ± 0.15	3.41 ± 0.24
850	2.07 ± 0.13	3.26 ± 0.23
875	1.95 ± 0.13	2.72 ± 0.20
900	1.63 ± 0.11	2.46 ± 0.18
925	1.62 ± 0.11	2.26 ± 0.17
950	1.77 ± 0.11	1.97 ± 0.15
975	1.89 ± 0.12	2.00 ± 0.15
1000	1.88 ± 0.12	1.88 ± 0.14
1025	1.91 ± 0.12	1.70 ± 0.13
1050	1.96 ± 0.12	1.65 ± 0.13
1075	1.73 ± 0.11	1.40 ± 0.11
1100	1.64 ± 0.11	1.28 ± 0.11
1125	1.39 ± 0.10	0.96 ± 0.09
1150	1.23 ± 0.09	0.84 ± 0.08
1175	1.12 ± 0.08	0.89 ± 0.08
1200	0.94 ± 0.08	0.53 ± 0.05
1225	0.89 ± 0.07	0.43 ± 0.05
1250	0.78 ± 0.06	0.27 ± 0.04
1275	0.66 ± 0.05	0.30 ± 0.04
1300	0.55 ± 0.05	0.24 ± 0.04
1325	0.56 ± 0.05	0.29 ± 0.04
1350	0.44 ± 0.05	0.31 ± 0.04

experiment. By comparing the data with those compiled by Walker, [1] this normalization constant is believed to be within 10%, which is within the order of magnitude of the quoted error bars.

5. DISCUSSION

In order to better understand the results of this experiment, we first tried to examine how well these results would fit into the existing phenomelogical models.

Since most of the data were taken for $k < 1200$ MeV, we expected that the isobars would dominate the region. Hence, we started from an isobaric model of photoproduction, using the form developed by R.L. Walker. [1] The photoproduction amplitudes of this model consist of the following three terms:

(1) The s channel nuclear isobar resonances in Breit-Wigner forms. Each resonance is characterized by a set of parameters as described by Reference 1.

(2) Born terms, which usually consist of s and u channel nucleon poles both with electric and anomalous magnetic couplings and a t channel pion pole for the production of charged pions. The inclusion of Born terms due to anomalous magnetic coupling in π^{o} photoproduction seems to yield bad fits to the existing data. Therefore, they are excluded in this scheme.

(3) Low-lying partial waves. These terms are essential to describe the non-resonant background. They have to be included to obtain good fits. One assumption of the fits is that these added low-lying partial waves (i. e., $l = 0, 1, 2$) should vary smoothly with respect to energy for credibility. Using this model to fit the existing cross section, recoil

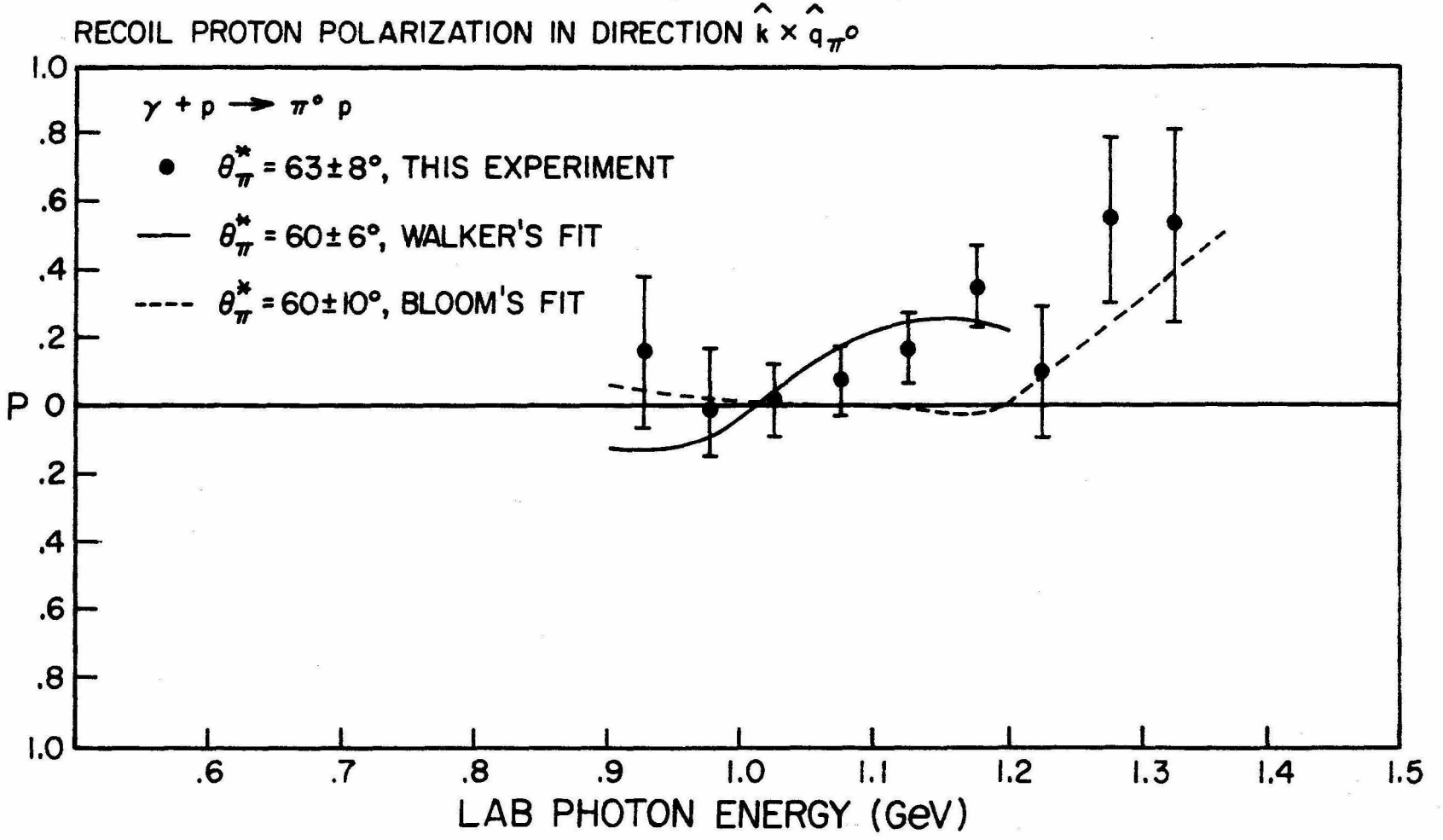

Figure 5.1 Polarization fit at $\theta^*_\pi = 63 \pm 8°$ as a function of energy.

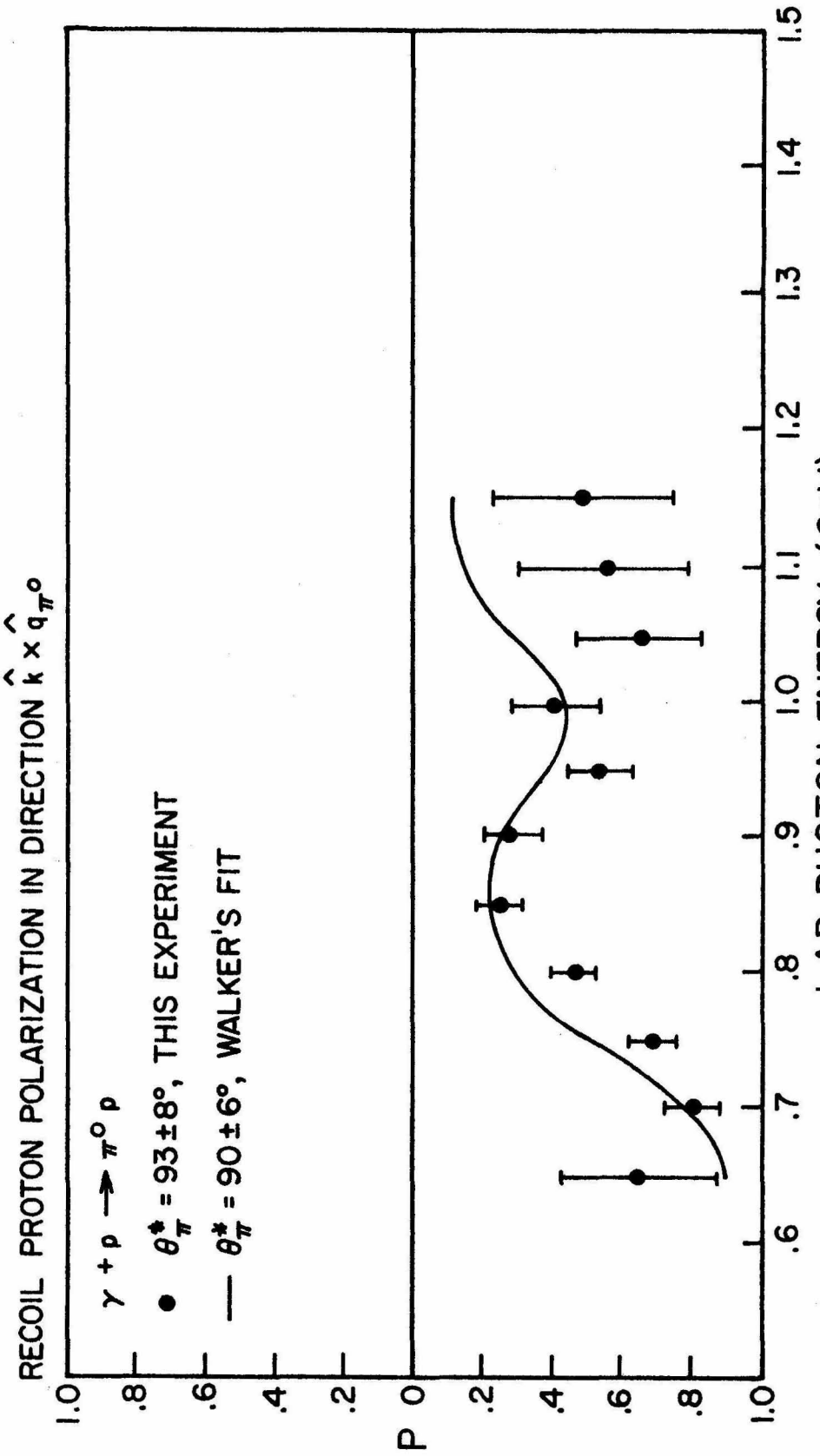

Figure 5.2 Polarization fit at $\theta^*_\pi = 93 \pm 8^\circ$ as a function of energy.

nucleon polarization, and polarized photon data, Walker was able to obtain the initial low-lying partial wave amplitudes as functions of energy.

Figures 5.1 to 5.4 display the polarization and differential cross section calculated according to this scheme, using the same set of low-lying partial wave amplitudes determined by Walker, plus Born terms and resonances.

The agreement between the prediction from isobar model and the measured data was very good at $k < 1000$ MeV. Significant deviation emerged for polarization at $\theta^*_\pi = 93 \pm 8^\circ$, $k > 1000$ MeV. (Presently only amplitudes at $k < 1175$ MeV have been determined, therefore no prediction could be made for k value beyond 1175 MeV.)

Bloom's fitting curve at $\theta^*_\pi = 60^\circ$ is also presented in Figure 5.1; he included a "fourth resonance" $N^*(1924)$ and a slowly turned-on Reggeized ω exchange trajectory in his fitting scheme. [6] Although this scheme fitted his data well, we are reluctant to adopt it, and, in the light of more recent theorectical development, we regard it as too much of an ad hoc ansatz; rather, we believe that a more thorough evaluation of both s and t channel partial wave amplitudes is necessary to avoid double counting.

However, in order to establish a meaningful angular correlation with better statistics, we incorporated the results of this experiment with those of Bloom's wherever possible. We feel justified in this procedure since the experiment of Bloom et al [6] was done by our group, with the assistance of this author, using essentially comparable techniques, albeit using a visual spark chamber system.

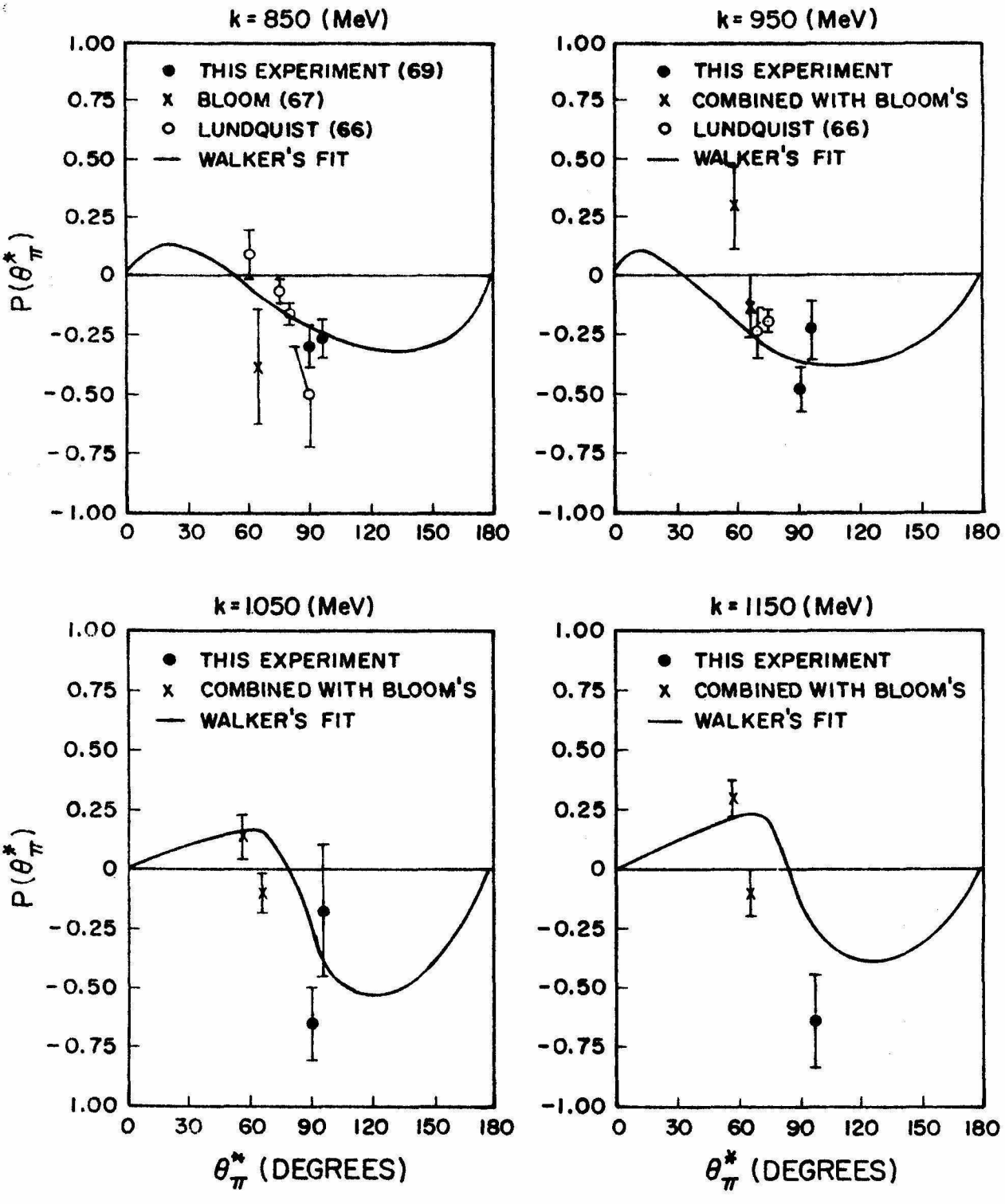

Figure 5.3 Polarization fits as a function of angle at different energies.

Figure 5.3 shows proton polarization as a function of Θ_π^* at different energies with Walker's prediction drawn on top of it. Here again, the prediction agrees with the measured values nicely at low energy. At k = 1150 MeV, the deviation from experiment becomes apparent. Nevertheless, the predicted trends are consistently in qualitative agreement with those of the data points.

Because of the nature of the helicity formalism, the recoil nucleon polarization (equation 1.1-2) is more sensitive to the change of a helicity amplitude than the differential cross section (equation 1.1-1). Aside from this, the differential cross section appears in the denominator of the expression of polarization, the uncertainty associated with the polarization becomes large whenever the corresponding differential cross section is small and ill-determined, like those at k > 1175 MeV. Therefore, a polarization measurement with better statistics included in the isobar model fitting would give a tight constraint to the helicity amplitudes.

The present status of π^o photoproduction fitting scheme may be improved if more resonances at higher energies and more higher partial waves are included when more data become available in the future.

On the other hand, it is obviously doubtful that the very assumption of isobar model mechanism should be valid for k > 1200 MeV and yield consistent and reasonable fits at all. Rather, we believe that in the framework of duality ideas, one will in the longer run strive to find alternate s and t channel descriptions of the intermediate energy region studied here. In order to do this, more data are

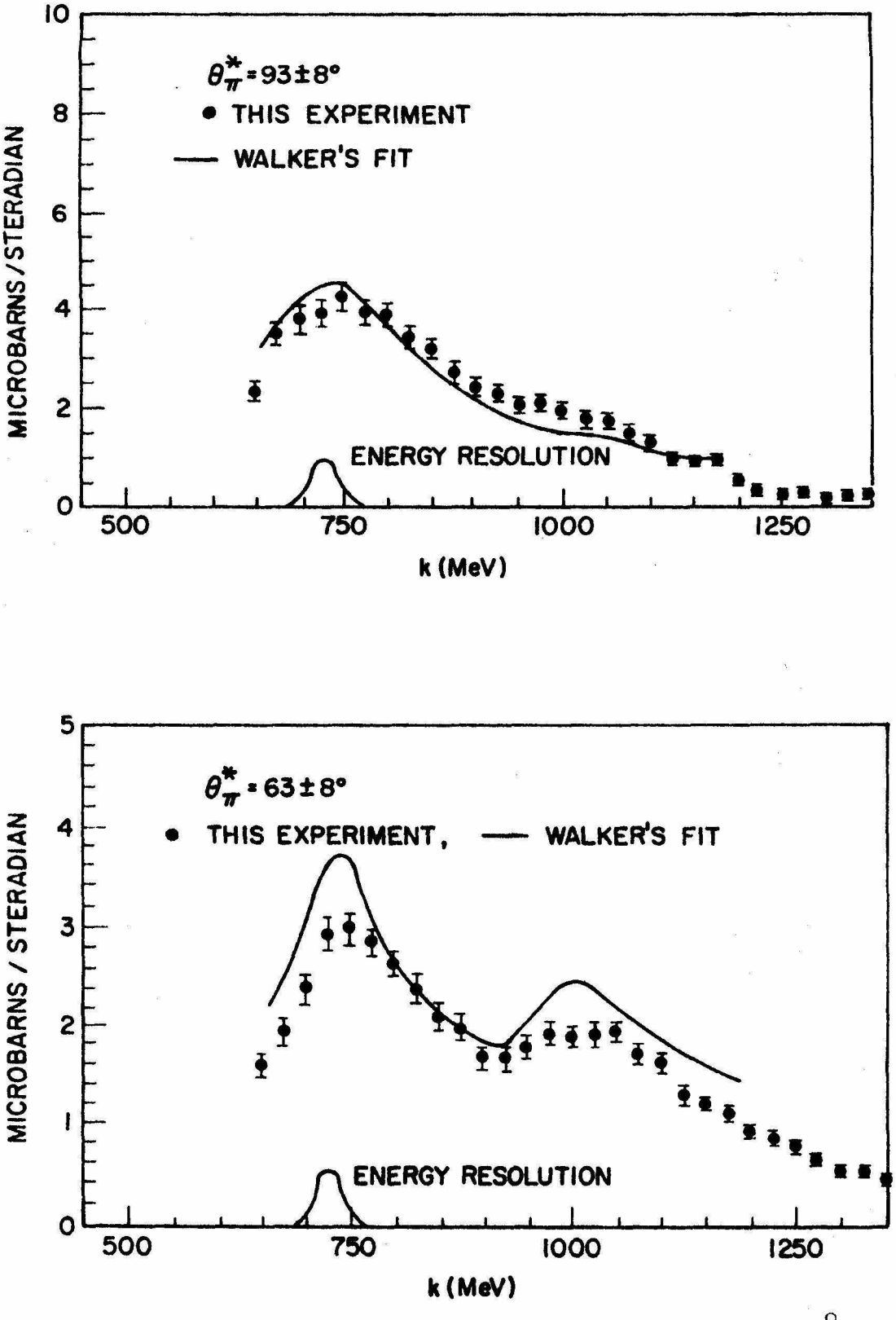

Figure 5.4 Differential cross section fits at $\Theta_\pi^* = 63 \pm 8^\circ$ and $\Theta_\pi^* = 93 \pm 8^\circ$ as a function of energy.

needed.

We doubt that with present methods the recoil nucleon polarization experiments can reasonably be carried much farther, with fuller angular distributions. However, experiments are soon going to start at Bonn and DESY to study π^{o} photoproduction off a polarized target, and also π^{o} production using polarized photons. According to the formulae given in the Introduction, more experiments, in conjunction with the data given here, will put tighter constraints on a really successful model.

6. APPENDICES

6.1 Photon Beam

The photon beam at the Caltech synchrotron was produced by bombarding a tantalum target (Z = 73) of 0.193 radiation length with the circulating electrons which had been accelerated to the energy E_o.

The Bremsstrahlung beam emerging from the synchrotron was collimated and scraped at several points along its path by passing it through lead apertures. Also, before reaching the liquid hydrogen target the beam was passed between the poles of a permanent magnet to deflect the contaminating charged particles (see Figure 2.2). By the time the photon beam reached the target, its diameter was about 2 cm. which was considerably smaller than that of the hydrogen target (3.81 cm. in diameter).

The photons which did not participate in any reaction went into a beam catcher where a Wilson type quantameter [18] was located. The quantameter was to measure the total energy of the photons by way of collecting the charges of the photon-induced shower. The pressure p of the gas in the quantameter and its external temperature T were measured daily. The value p/T, which is proportional to the amount of gas in the quantameter and thus also proportional to the sensitivity of the device, was found to be constant to within 0.2%. The output of the quantameter was fed into a charge integrating circuit. Calibration of the integrator was performed daily during the runs and remained constant to within 0.27%.

The quantameter constant obtained was

$$1 \text{ BIP} = (1.097 \pm 0.0029) \times 10^{13} \text{ MeV}$$

Although in a polarization experiment, an absolute calibration was not necessary, the consistent monitoring of the photon beam throughout the experiment did help to make a better differential cross section estimate.

6.2 Hydrogen Target

The origin of the laboratory coordinates was defined as the geometric center of the liquid hydrogen target. The liquid hydrogen was contained in a cylindrical cup made of 0.005" mylar. The dimensions were 9.18 cm. in length and 3.81 cm. in diameter. A 0.001" aluminum sheet, kept at liquid nitrogen temperature through thermal contact with a liquid nitrogen container, was placed around the cup for heat shielding. The outside shell was a longer cylinder made of 0.035" aluminum sheet with both ends open except for 0.005" mylar. The space between the outside shell and the cup was maintained at high vacuum by a diffusion pump. A temperature dependent carbon resistor was placed on top of the cup. The voltage across it indicated the fullness of the target. An automatic filling system was driven by this voltage reading to keep the target constantly full. A similar device was used to keep the liquid nitrogen container constantly full. Figure 6.1 shows the construction of the target.

6.3 π^o Detector

The apparatus (see Figure 6.2) was designed to detect the neutral pi meson ($\tau = 0.89 \times 10^{-16}$sec) via its decay mode $\pi \rightarrow \gamma + \gamma$

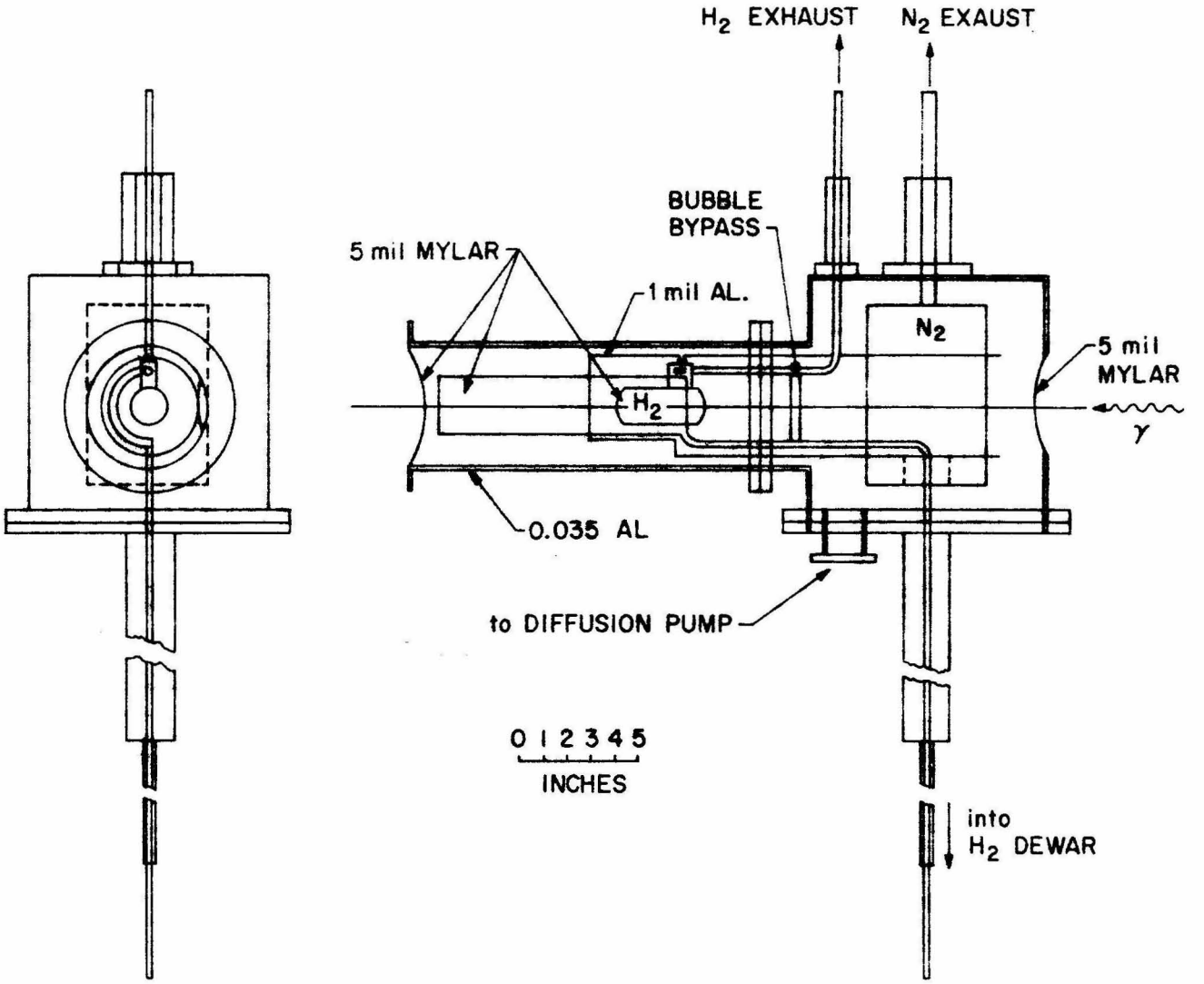

Figure 6.1 The hydrogen target.

(branching ratio 98.8%) and $\pi \rightarrow \gamma + e^+ + e^-$ (branching ratio 1.2%).

Only one shower counter was used to detect the forward decaying photons. In the kinematical region covered, these photons carried energy between 260 MeV and 950 MeV making them capable of inducing cascade showers in lead. The dimensions of the shower counter and its distance from the target were chosen such that at least the forward decaying photons would be detected (photons which decayed in a forward direction in the center-of-mass system. The Lorentz transformation made the C.M. forward going photons into a cone centered at the direction of the π^o's motion in the lab with an opening half angle of $\mathrm{Sin}^{-1}\left(\frac{M_\pi}{E_\pi}\right)$.

In front of the shower counter there was a veto scintillation counter. The purpose of this counter was to exclude charged particles like protons or charged pions so as to make certain that the cascade shower in the shower counter was not induced by the charged particles. A coincidence of no signal from this veto counter and a properly biased signal from the shower counter served as a signature for a high energy gamma ray.

The efficiency of the veto counter was somewhat rate-dependent: about 99% at the settings with θ^*_π = 93 +- 8 degrees, and 97% when the detecting system was moved to a more forward direction of θ^*_π = 63 +- 8 degrees. The efficiency was also slightly dependent on the intensity of the Bremsstrahlung beam. Fortunately, throughout the experiment, only a relatively small beam intensity (averaged 0.6×10^{10} electrons per beam dump) was used so that the master trigger rate would not exceed one per beam dump which was the maxi-

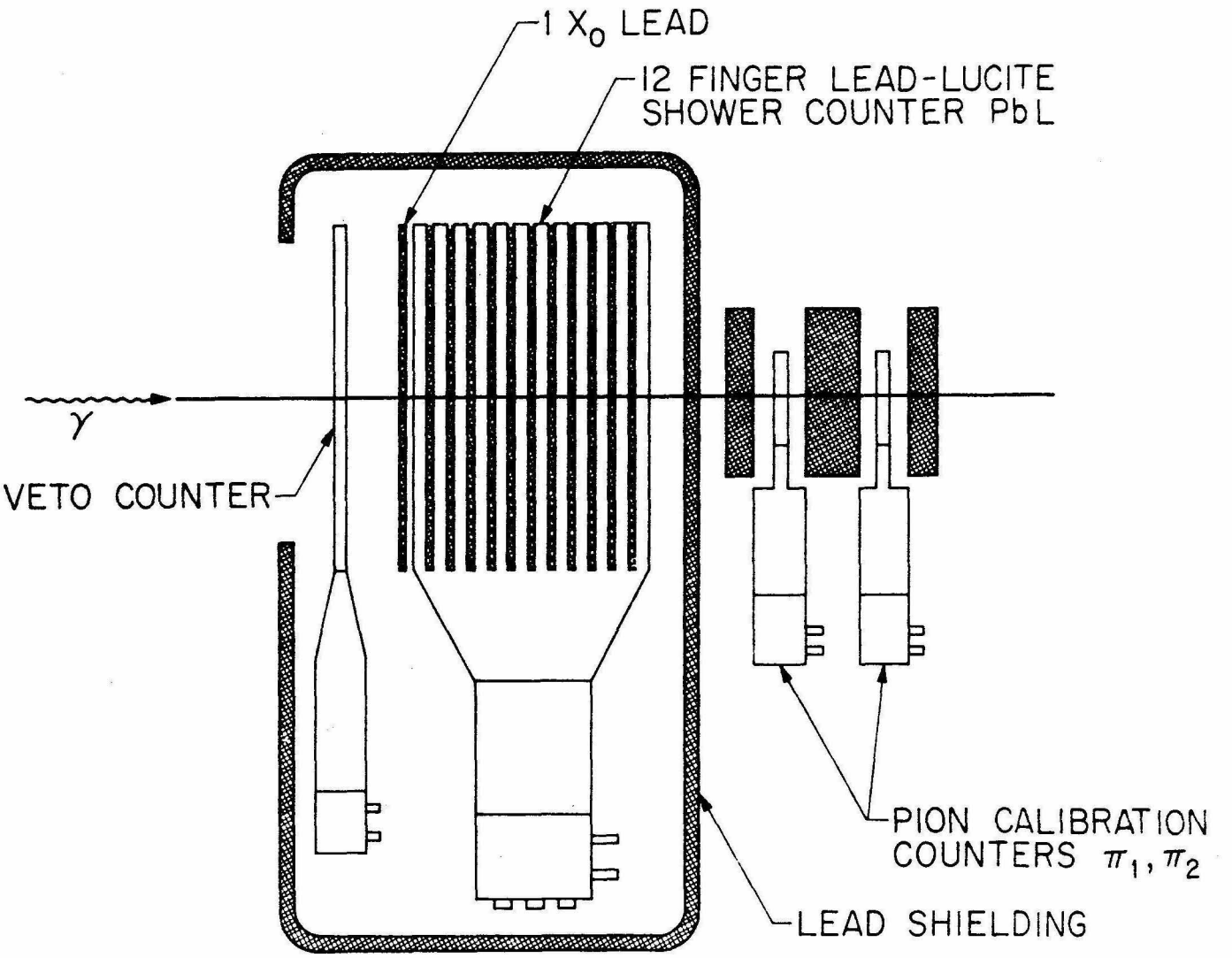

Figure 6.2 γ Detection System

mum data collection rate the on-line PDP-5 computer could handle.

The requirement of a minimum pulse height of 250 MeV from the shower counter in the data analysis (see Section 3.2) would certainly reject any charged particles which slipped through the veto counter without being instantly rejected.

No hodoscope was used to try to determine the location of the shower as was done in the previous optical spark chamber experiments. [6] Since the trajectories, and hence the energy, of the recoil proton could be accurately determined, it became obvious that as long as a clean π^o trigger was provided, the whole kinematics of the reaction could be completely reconstructed without knowing the location of the shower (see Appendix 6.11-D). The sole advantage of knowing the shower location was to discriminate the multipion production background events from the single pion production events. Since the multipion background was estimated to be at most only a few percent effect which was further reduced by a factor of 2 by setting a high energy bias of 250 MeV in the shower counter pulse height, (see Appendix 6.17) it was clear that it would not be worth the trouble to build the hodoscopes and the fast electronic on-line readout system.

Knowledge of the location of the shower would not help much to discriminate against Compton scattering background events. The kinematics of Compton scattering is very similar to that of single pion photoproduction in the presence of a high energy incident photon beam ($k \gg m_\pi$, see also Appendix 6.18). Within the accuracy of the energy resolution of the shower counter ($\Delta E/E < 15\%$) the elastically

scattered photons behaved very much the same as the forward decaying photons from π^o. However, the Compton scattering background was estimated not to exceed 4% on the average (Appendix 6.18) which was tolerable for the statistics intended.

The best way to discriminate against Compton scattering background events is to detect both decaying gamma rays of the π^o by using two shower counters in symmetric locations with respect to the π^o production plane. [17] Thus, a pion trigger would demand a coincidence of both shower counter signals. The reason why this unique method was not used in this experiment was that its counting rate was one order of magnitude smaller than that of the one-shower-counter method. It therefore would not take the full advantage of the fast on-line data collection rate.

A. Shower Counter

The shower counter consisted of alternating layers of lucite and lead. The lucite radiator of the shower counter was constructed out of 12 sheets of 0.43" lucite, 19" wide and 10" long. At one end all the lucite layers were glued to a light pipe with 1/4" lucite spacers in between. The light pipe lucite was tapered to better fit on a 5" XP 1040 photomultiplier tube. The counter was wrapped with 0.005" aluminized mylar and black tape to seal the counter from external light sources. The lead sheets, 0.2" thick and cut to fit in the 40 cm. by 21 cm. aperture of the counter, were inserted in the spaces between the lucite sheets. One additional lead sheet was placed in front of

the shower counter to make the total number of lead sheets 12.

As the cascade shower develops in the lead sheets, the fast-moving positrons and electrons in the shower generate Cerenkov radiation in the lucite slabs. The amount of light generated is proportional to the total path length traveled by the charged particles in the lucite slab. The light is then collected and converted into an electric pulse in the XP 1040 phototube.

Since the lucite is a Cerenkov radiator, only the charged particles traveling faster than the Cerenkov threshold velocity can generate light. Therefore the lead lucite counter has no response to slow protons or low-energy charged pions. This provided a strong argument for favoring the lead lucite system instead of a lead scintillation system for shower detection. (19)

B. Shower Counter Calibration

Since a monoenergetic photon beam was not readily available, the testing of the shower counter was done in a monoenergetic energetic electron beam. For a total absorption counter, the photon initiated shower differs from the electron initiated shower significantly only in the first several radiation lengths where the memory of the incoming charge is still retained to some degree. Since there were altogether 12 X_o (1 $X_o \approx 0.2$" lead is one radiation length) of lead placed in the counter, it was assumed that there was no significant difference between photons and electrons. This has been confirmed in a test by using a tagged photon beam as was explained in CTSL-41 and in the literature (19)

Figure 6.3 shows the response of the lead lucite counter to energetic electrons. In the lower end of Figure 6.4 there were two points each corresponding to a distribution taken by removing all lead sheets from the shower counter. The response was found independent of the incident electron energy in the energy range covered.

It was necessary to set a certain discrimination level on the shower counter during the experiment. For this purpose, a pion telescope was set up (see Figure 6.2) by placing two scintillation counters of smaller aperture, 5" by 6", separated by 6.5 cm. of lead brick, behind the shower counter. This lead brick plus the lead in the shower counter was thick enough to stop all charged particles except fast π's and μ's. For the π's capable of reaching the back pion counter, their kinetic energy would be in excess of 225 MeV or $\beta \geq 0.92$. The radiation produced by the fast moving π's resembles that of the passing electrons. Therefore, the pion telescope provided an on-the-spot calibration of the pulse height of the shower counter.

The electronic bias was set slightly below the minimum-ionizing peak. (In the data anlysis the final energy cutoff was set at 250 MeV.) The minimum ionizing peak was located in the pulse height distribution obtained by letting the charged pions pass through all counters, i.e., trigger = V x PbL x π1 x π2.

Since these two pion scintillation counters were used only for the shower counter calibration, their participation was not needed to form the master trigger of the single π^{o} photoproduction.

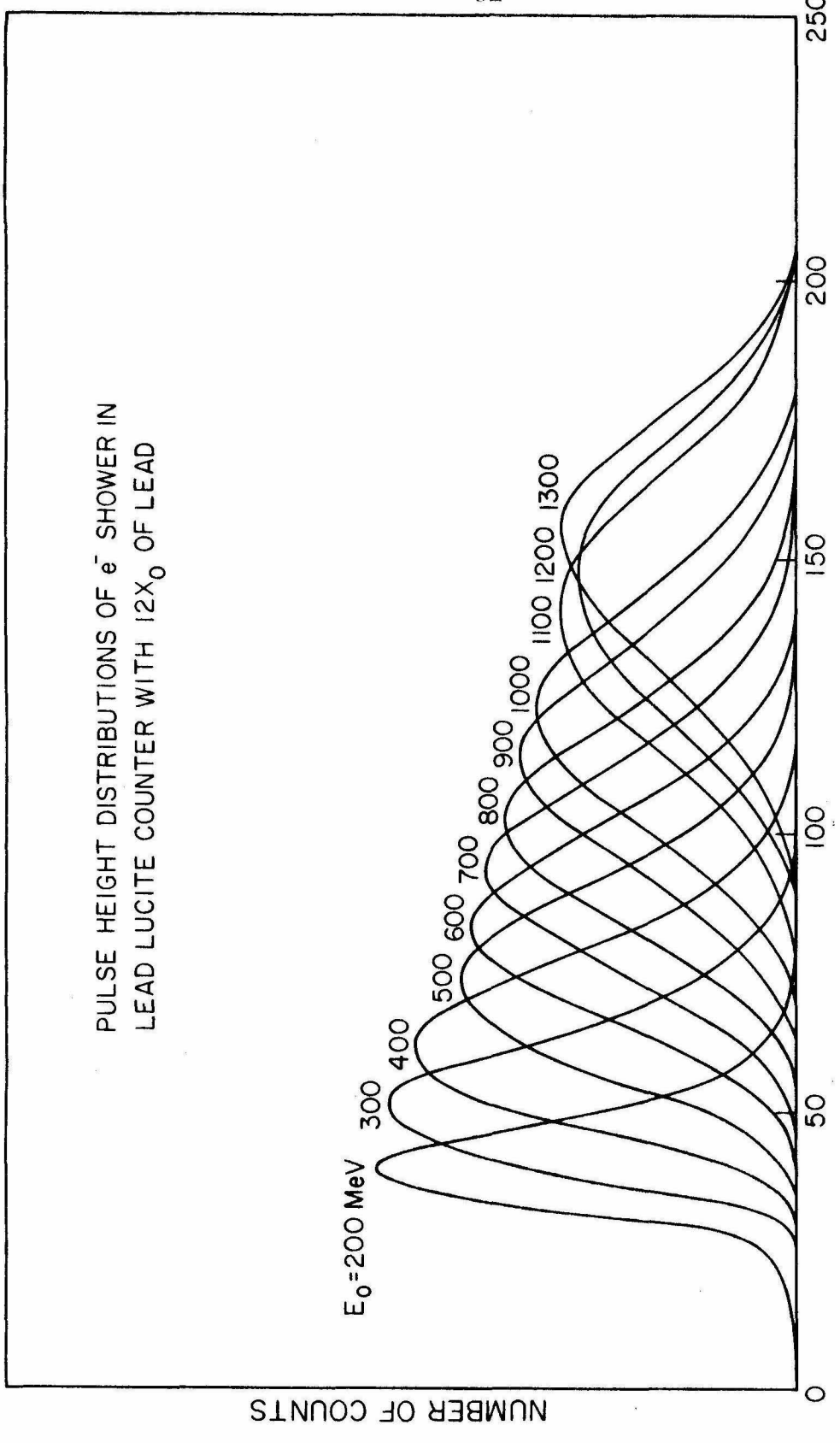

Figure 6.3 Response of lead lucite counter to energetic electrons.

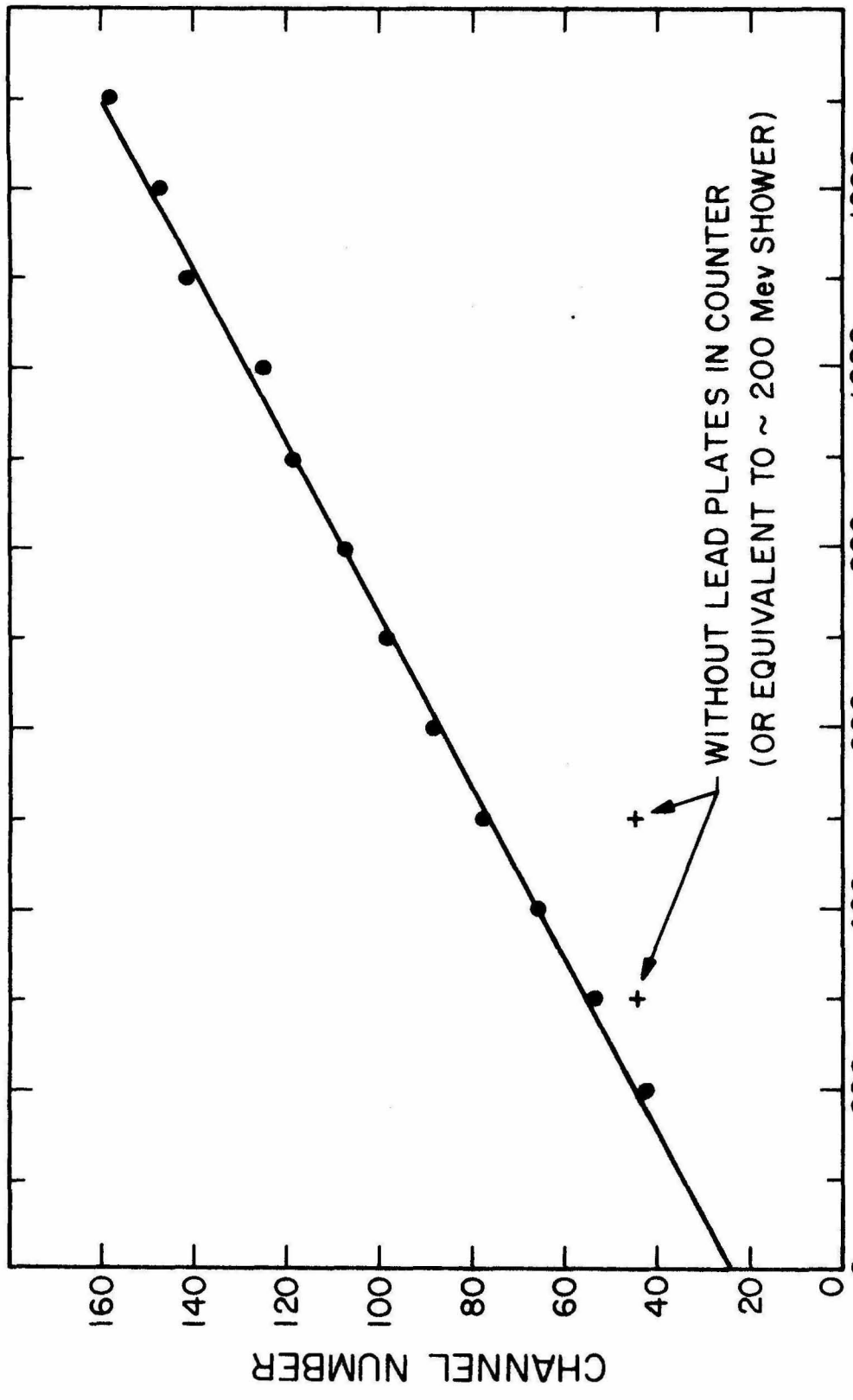

Figure 6.4 Gain-monitor shower calibration curve.

A more elaborate and accurate shower counter calibration was done before and after the data acquisition by placing it in a monoenergetic electron beam as explained in the previous section.

In order to prevent the system from being accidentally triggered by undesired particles, the whole apparatus was shielded by lead sheets except for a front aperture of 40 cm. by 21 cm. and a rear aperture of 5" by 6". The counting rate of the shower counter was found to increase one order of magnitude when the bending magnet was turned to the highest momentum configuration (approximately 14k gauss between pole tips). The trouble was removed by wrapping the whole XP 1040 phototube section with four additional layers of high magnetic shielding material.

The pulse height of the shower counter was converted into digital information in a Nuclear Data multichannel pulse height analyzer. It was recorded in a magnetic data tape along with the spark information of the recoil proton trajectory. Figure 6.5 shows a typical $\pi^{\pm}$ spectrum. The electronic bias was set around 150 MeV.

6.4 Proton Telescope

The proton telescope consisted of three scintillation counters. It was located right behind the bending magnet. The scintillation counters were constructed of 1/4" NE 102 scintillator, 10" in width and 6" in height. Each counter had a flat light pipe which was tapered to fit into a RCA 7850 phototube. The center of the scintillators was coincident with the central ray of the bending magnet

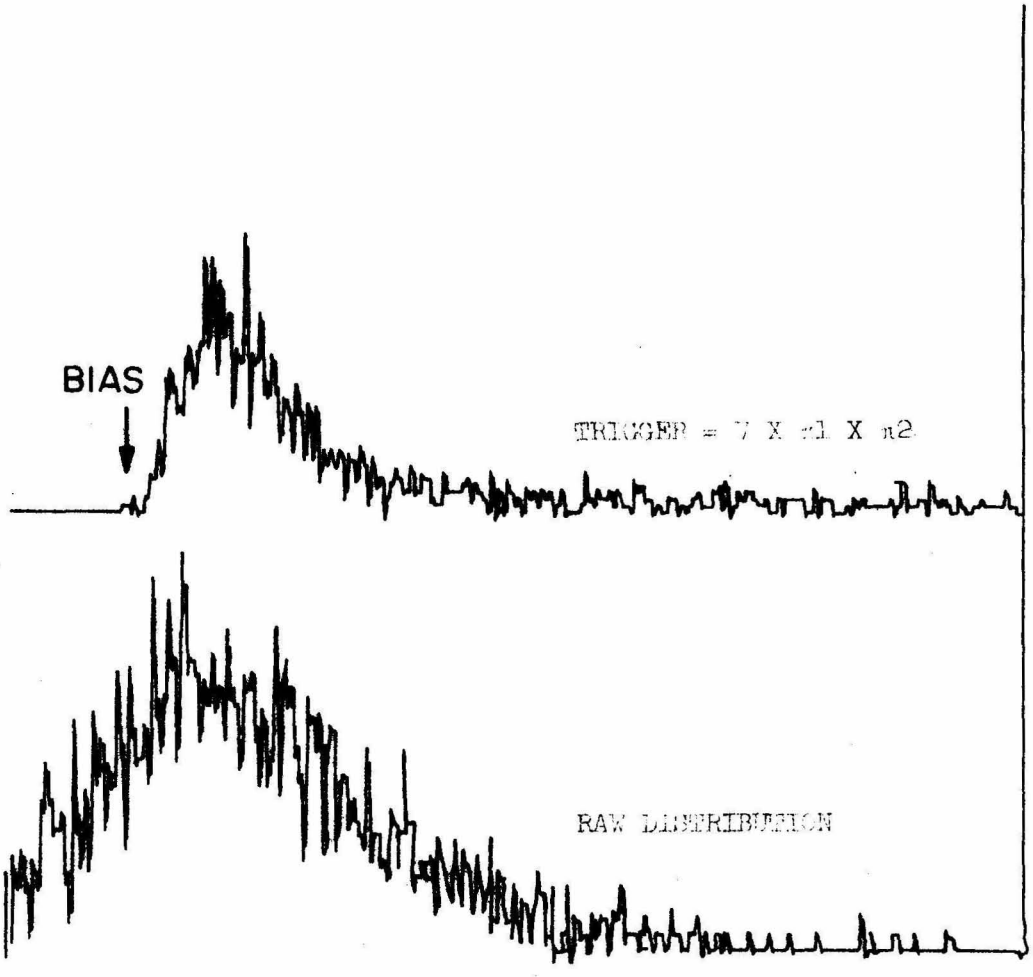

Figure 6.5 Pion pulse height distribution taken in lead-lucite shower counter.

(central ray being the referrence proton trajectory whose momentum was known). The counters were separated from each other by a distance of 3 inches. In front of each of the scintillators, there was a big square wire chamber, 20" by 20", where the trajectory of the charged particle exiting from the bending magnet might be reconstructed. All these wire chambers and the scintillation counters were mounted in an aluminum box with two openings of 4" in height and 20" in width for beam passage. The 4" height of the opening matched the distance between the magnet pole tips.

A coincidence of signals from all three scintillation counters was required in the fast logic. Every master trigger obtained in the experiment corresponded to a charged particle going through an effective area of 4" by 10" of the proton telescope.

The purpose of the proton telescope was to accept protons and to discriminate against charged pions or electrons by putting a suitable pulse height bias on each counter. The conventional method of placing a fourth counter with high pulse height bias behind the range chamber [17] to help to set the bias was not used in this experiment because in the initial setting, protons could never reach the back of the range chamber to trigger the fourth counter for lack of energy. In addition to that, the kinetic energy of the recoil proton could be accurately determined by using the wire orbiting calibration method. Therefore, we could afford to set the bias slightly lower than that of the conventional method so that one hundred percent of useful protons would be accepted. The few percent background events which accidently passed the pulse height require-

ment would be removed when more requirements were imposed during data reduction.

The raw pulse height distribution of a proton scintillation counter was obtained by requiring a coincidence of the other two counters, both in low bias. The bias of that counter was set by adding attenuators in the input signal side of the fast logic. A second pulse height distribution of the same counter with bias would be taken requiring a triple coincidence. The amount of attenuation was finally determined when the biased pulse height distribution began at a place corresponding to the middle of the front shoulder of the raw distribution, thus removing most of the undesired background from it.

The final pulse height distribution of slow protons was obtained when all three counters were properly biased. Figure 6.6 shows a typical set of distribtuions obtained in this way.

The voltage on all phototubes was monitored by means of a precision digital voltmeter. Variation of phototube voltages was within one part in 10^4.

6.5 Characteristics of Wire Spark Chamber

The wire spark chambers built for this experiment were one gap devices; the conducting wires ran vertically on one side and horizontally on the other side. The spacing between the adjacent wires was 0.04". The frame of the chambers was made of benelex. An enclosure made of 0.002" mylar sheet shielded the whole active region from the exterior.

Since the spacing was 0.04", the spatial resolution of a

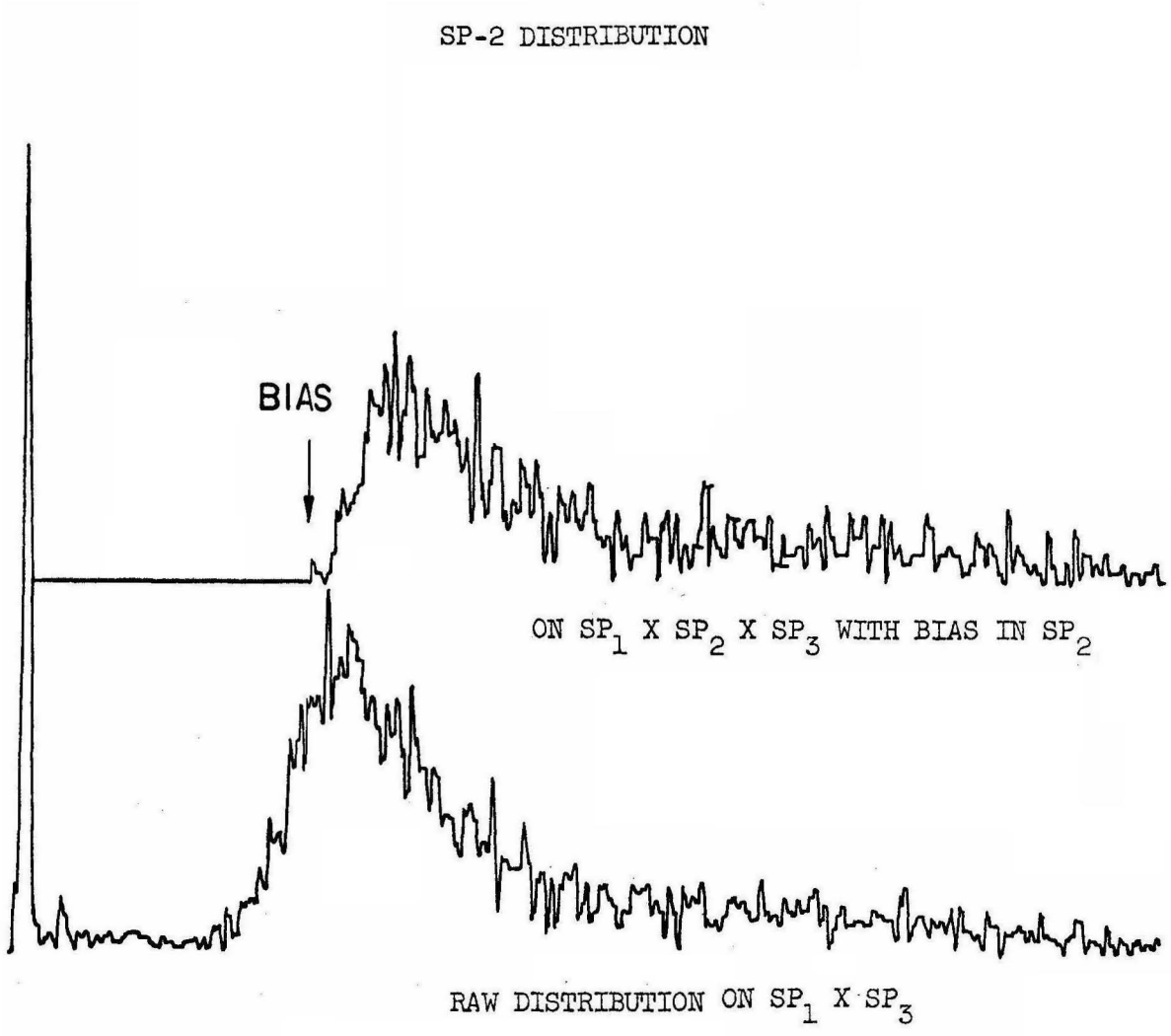

Figure 6.6 Pulse height distribution of a typical SP counter.

spark was not expected to be better than 0.02". When a few sparks, each with such accuracy, were fit into a straight line the fitted line was expected to be closer to the physical trajectory than its constituent sparks. The delay time of our chambers was measured to be 500 nsec when operating in the system. This was the time between the recognition of a proton and the application of high voltage across the wire chamber to induce sparks.

This delay time together with the counting rate of the proton telescope determined the number of tracks one saw in the chamber per trigger. In this experiment, both were such that only one track was seen in the back chambers, and occasionally two tracks might appear in the front chambers. This was due to an intense Bremsstrahlung beam or the geometry of the apparatus.

A high chamber efficiency could be maintained with a wide range of sweeping voltages. Since the intrinsic delay of the wire chambers was 500 nsec., we chose a sweeping voltage just below the voltage at which the efficiency dropped away from 100%. At 500 nsec delay and 45 volts, a minimum amount of background, consistent with the maximum efficiency, was obtained.

Aside from the application of a sweeping field, we shortened the memory of the chambers by adding a quenching agent, such as pure alcohol, to the inert gas which was flowing in the chambers at all time. During the experiment, part of the neon-helium gas mixture was saturated with alcohol before entering into the system.

The operation of the wire chambers was found to be strongly dependent on three factors.

(1) The H.V. pulse applied across the chambers, which was set around 10 kv in the experiment.

(2) The purity of the gas mixture. A slight contamination of air or water vapor always resulted in malfunction.

(3) The amount and the purity of alcohol in the system.

A sample of the gas mixture used in the experiment was chemically analyzed. Table 6.1 shows its composition.

6.6 Carbon-Plate Wire Chamber System

The carbon plate wire chamber system, consisting of alternating wire chambers and modular carbon plates, served to slow down and to stop the recoil proton and provided the target material for p-C scattering from which information on proton polarization might be derived.

There were up to 20 wire chambers and 43 carbon-plates used in the system. The thickness and the number of carbon-plates varied with the synchrotron end point and the kinematics of the setting. For the data taken around θ^*_π = 93 degrees, all 43 carbon-plates were needed to stop a proton of 310 MeV kinetic energy.

The thickness of a wire chamber was 3/8", that of carbon module frame was 3/8" or 1/2" depending on whether it held a 0.5 or a 1 cm. plate. The system, with all 20 wire chambers and 43 carbon-plates tightly packed together, occupied a span of 26".

Gas flowed in parallel through the gap of the wire chamber to prevent a pressure differential within the chamber. In order to maintain a faster flow rate and minimize the gas consumption, a closed

TABLE 6.1: COMPOSITION OF GAS SAMPLE

Mass Spectrometer Analysis

	Mol. %	
Helium	19.16	
Neon	77.45	Min.
Nitrogen	.64	
Oxygen	.23	
Argon	None Detected	
Freon 12	None Detected (20 PPM Sens.)	
Water (Vapor)*	2.51	Approx.
Alcohols	Less than 10 PPM, if Present	
	100.00	

* Water value reported is approximate only due to adsorptive and desorptive effects on glass container and inlet system of mass spectrometer utilized.

gas system was employed. It circulated at a rate of about 15 ft^3/hr. Usually it took about one and one half hours to fill up the system. (The residual gas in the chambers dies out according to an exponential law.)

Electrical contacts to the chamber were mounted in the sides of the chamber. The high voltage was applied to one side of the chamber while the ground leads were connected to the other side. The aperture of the wire chamber was 20" by 20". Each wire chamber or carbon module could be slid in and out by loosening the steel frame which held them tightly together as a unit.

To permit accurate measurement of the spark positions in the laboratory system, fiducial marks were added to all views of the wire chambers. Whenever an event triggered the system, along with the sparks which registered the passage of charged particles, the first and the last conducting wires of each view (or each side) of a wire chamber were fired simultaneously. The interval between these two signals was used to normalize the locations of sparks in space. Before and after the experiment, the distance between the first and the last wires of each view of each chamber was measured to within 0.01". Before the major data reduction, the time interval between the arrivals of the first fiducial signal and that of the second one was calculated by averaging them through a large sample of events. The mean interval was then used as an input in the preliminary data reduction. The advantage of using a mean value instead of doing normalization individually was to suppress the statistical fluctuation of the time interval between two fiducials, and to supply a reasonable value to

those events whose fiducials either failed to fire or failed to be registered.

When a recoil proton entered into the system, the trajectory was manifested by the sparks it generated. Its energy was determined by the amount of carbon it traversed before stopping. The arrangement of alternating wire chambers and carbon modules ensured that sufficient information could be extracted about the trajectory of the recoil proton. When a p-C interaction with an appreciable scattering angle (4 degrees at one view) was observed, not only the energy of the incoming proton would be determined by using the energy range relation (also can be determined by the wire orbiting method as will be discussed in Appendix 6.11) but also the inelasticity of the scattering.

The intrinsic uncertainty of the range measurement was given by the amount of carbon between the stopping wire chamber and the next one. Throughout the experiment, this uncertainty in terms of proton kinetic energy was put at about 10 MeV. A more detailed explanation is given in Appendix 6.11.

A big aluminum house was built to hold all the wire chambers and the carbon modules. Great care was taken to ensure an easy access and rearrangement of the chambers. The whole house was mounted on top of a flat steel frame where fine adjustments were provided to easily locate the whole house in the desired orientation and position.

6.7 On-Line Readout System

The spark and fiducial signals from one view of a wire

TABLE 6.2: THE COUNTERS AND COUNTING RATES OF THE EXPERIMENT

Counter	Use in Experiment	Horizontal Size	Vertical Size	Thickness	Material	Typical Counting Rate Per Second
SP-1	Proton telescope counter	25.4 cm.	15.24 cm.	0.635 cm.	NE 102	2×10^3
SP-2	Proton telescope counter	25.4 cm.	15.24 cm.	0.635 cm.	NE 102	3×10^3
SP-3	Proton telescope counter	25.4 cm.	15.24 cm.	0.635 cm.	NE 102	3×10^3
Veto	Used in π^o side in coincidence with PbL counter to veto charged particles	45.7 cm.	25.40 cm.	0.635 cm.	NE 102	0.7×10^6
PbL	Lead lucite shower counter used on π^o side to detect photons	40.00 cm.	21.91 cm.	1 X_o lead in front of counter. 12 sheets of UVT lucite fingers each 1.1 cm. in thickness interspaced with 11 sheets of lead 1 X_o thick		0.5×10^4
π-1, π-2	Used to calibrate PbL counter, not used in π^o trigger	15.2 cm.	12.70 cm.	1.27 cm.	NE 102	Not relevant

chamber propagated to both ends of the wire chamber frame. A wand, with its magnetostrictive ribbon perpendicularly pressed against the conducting wires, picked up the signals by induction into the ribbon at one end of the chamber. The signals then propagated along the ribbon at the speed of sound (about 5000 meters/sec). A rubber pad was attached to one end of the ribbon to damp and to terminate the signals with minimum reflection. On the other end, there was a pick-up coil made of a few turns of copper wire, where an electric pulse was induced upon the arrival of a signal on the magnetostrictive ribbon. This pulse was immediately pre-amplified and shaped in the small amplifier of the wand. The output signal was then sent back to the control area via a 50 Ω cable. The signal was again amplified and shaped to a standard form of two negative peaks sandwiched between a larger positive peak. A proper bias was set to exclude possible noise pulses. The pulse output of the second stage amplifier was fed into a Lecroy electronic time digitizer. The time interval between the arrivals of the first pulse (presumably the first fiducial signal) and any of the subsequent pulses was digitized in clock units. It was found that a clock unit (generated by a quartz oscillator) corresponded to a distance of 0.267 mm. in space. For a typical wand, a full Lecroy digitizer unit was assigned so that up to four sparks could be registered in that wand. The arrival of the first fiducial pulse turned on the gates of all four scalers such that the quartz clock pulses would be registered continuously as long as the gates remained open. The arrival of a second pulse, which could be a spark, a filtered noise signal, or the second fiducial signal, would close

the gate of the first scaler. Whatever was left inside the 12-bit flipflop of this scaler indicated the time interval between the two signals. Likewise, the arrival of a third pulse terminated the counting of clock pulses in the second scaler. The signal of the second fiducial signal was treated on the same footing as the previous sparks.

Most of the time, there were not enough sparks to exhaust all four scalers. The contents of the unterminated scalers always showed 7777_8 (that is, all 12 flipflops in "on" positions). This provided a very easy pattern to recognize when the data were processed by a real time computer. However, there were occasions, particularly in the front chambers, when the beam was so intense that more scalers were needed to accomodate all the sparks and the fiducials. This situation would result in only registering the first four sparks and truncating the rest of them by sending out a flag signaling the condition of overflow.

After studying the chambers' and wands' performance, a decision was reached to assign a full Lecroy unit of four scalers to each view of the first eight wire chambers (five in the front and three behind the bending magnet, sandwiched with the proton scintillation counters), and only a half Lecroy unit to each view of the wire chambers in the carbon plate range house. This assignment turned out to be reasonable: no event was lost for lack of digitizer units.

In addition to the spark and fiducial locations, the pulse height from the lead-lucite shower counter, and the time of flight

between the signals of the third proton scintillation counter and that of the shower counter were digitized in a 256 channel Nuclear Data pulse height analyzer.

The run number and the magnet configuration number were typed into the PDP computer manually at the beginning of every run. The event number was incremented by one whenever a new event triggered the system. A complete format of an event is shown in Table 3.2. The event information was first stored in the data buffer of the PDP. Its contents were displayed on the RM 561 A oscilloscope while waiting for the next event. The triggering of a second event would transfer the information of the previous event in the PDP buffer into a seven track magnetic tape. It took about 3" of tape in low density to record a complete set of event information. The records were separated from each other by a 3/4" record gap. Therefore, a full size tape of 2400 ft. contained up to 7200 records which, for sake of convenience, usually made up one run.

At the end of a run the teletype typed out the run number and the total number of events. Then the accumulated pulse height distribution and the time-of-flight distribution would be dumped into the tape in a predetermined format. Finally, the end of file mark (which is 1717_8 in the PDP and 360 machines) was put into the magnetic tape to signal the end of a run.

These two accumulated distributions were redundant in the sense that their constituent components could be found scattered all over the tape. However, they provided a quick check on the whole distributions without looking into the records one by one. Frequently,

it was necessary to get the whole shower counter pulse height distribution, and to decide where to put the bias of 250 MeV.

6.8 Alignment and Surveying Method

The accuracy associated with the location of the apparatus was of crucial importance. Much time was spent on a surveying system which aligned the wire chambers to better than 0.02". This was accomplished by putting all wire chambers into three well machined boxes. Before inserting the wire chambers, an empty wire chamber frame of the same size was inserted into each possible location one at a time. The distance from the predetermined central orbit to the intersection of the central cross hair of the empty frame was recorded. Since the chambers in the same box were tightly locked against a machined edge, it was possible to reproduce the chamber locations to within 0.02". Most of the error in spark localization came from the uncertainty of the transit location.

Great care was taken to survey the bending magnet to the predetermined position. We used a transit in the target position. At both the entrance and the exit sides of the magnet, a cross hair frame attached with a horizontal ruler was mounted facing the transit. The cross hair and the reference frame were made of non-ferromagnetic material so that when the magnet was turned on, the strong magnetic field ($\leq$ 14 k gauss) would not dislocate the reference frames or the cross hair.

The laboratory coordinate system was defined by scribed pieces of aluminum. Some were epoxied to the floor below the

bremsstrahlung beam line, and others at known angles relative to the beam line. Beam height was defined by similar metal pieces epoxied onto the wall of the laboratory. The location of the transit was kept calibrated using these reference marks. Transits were used mainly for the angular measurements and sometimes for distance measurements when a fine inscribed ruler was attached to the object which was to be surveyed.

Less care was taken in placing and surveying the π^{o} system, since the kinematics were less sensitive to this information, and the precise location of the shower was not used for the analysis. Both the π^{o} and the proton detection systems were moved only once during the experiment. One alignment was for pion C. M. production angle near 90 degrees, the other for 60 degrees. Although various synchrotron end points were used for the same C. M. pion angle, the kinematics made a change of geometry unnecessary.

6.9 Electronics

Figure 6.7 shows the general layout of the logic and the electronic readout system. The fast logic consisted of a two-fold master coincidence between the π^{o} side and the proton side of the experiment.

The signals from all counters were brought into limiters before entering into the logic. The outputs of the limiters were clipped and fed into discriminators. The signals from the discriminators were used in various coincidence circuits determining the trigger. The delay curves of the coincidence circuits showed a typical

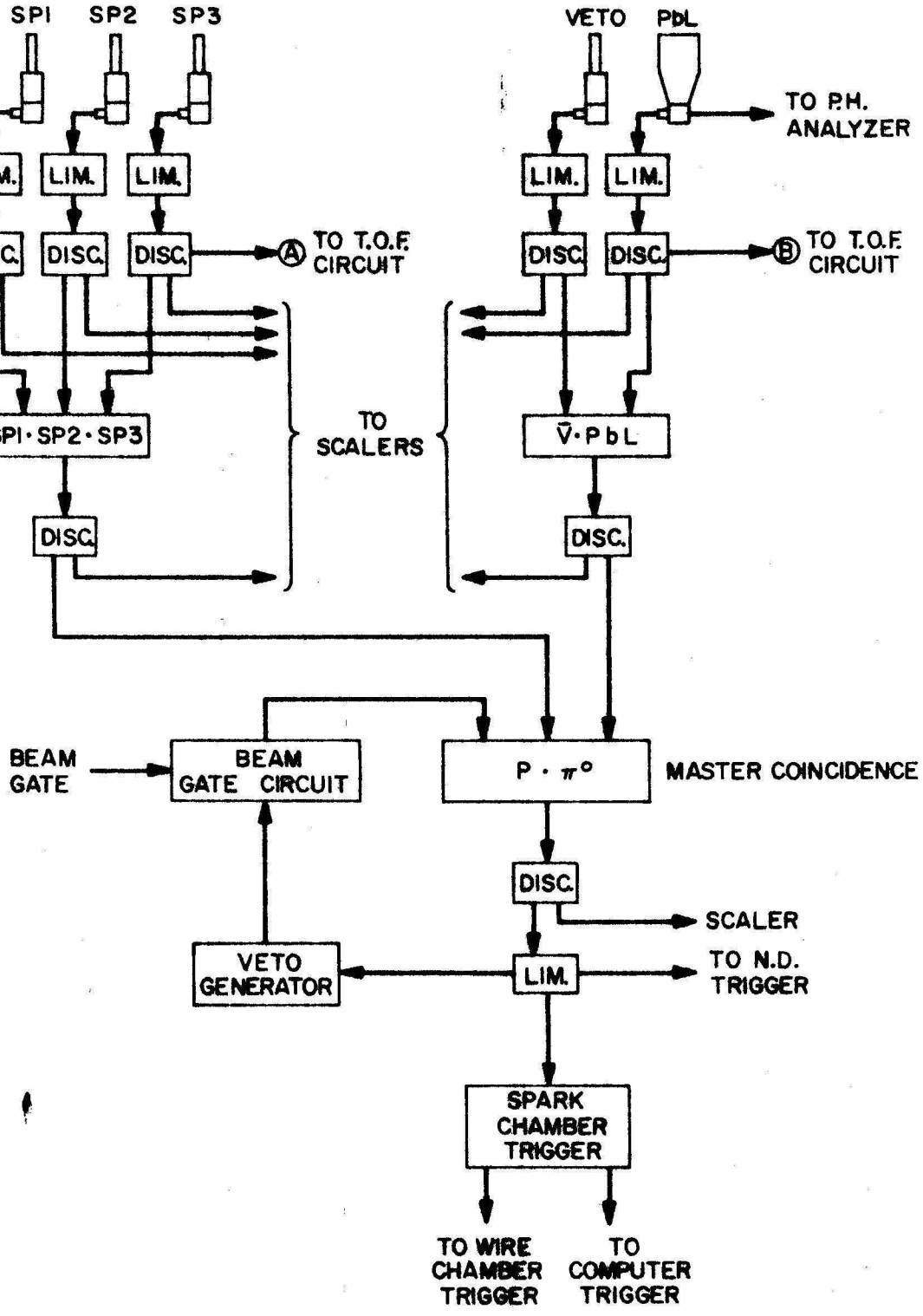

Figure 6.7 A: Fast logic for pion trigger.

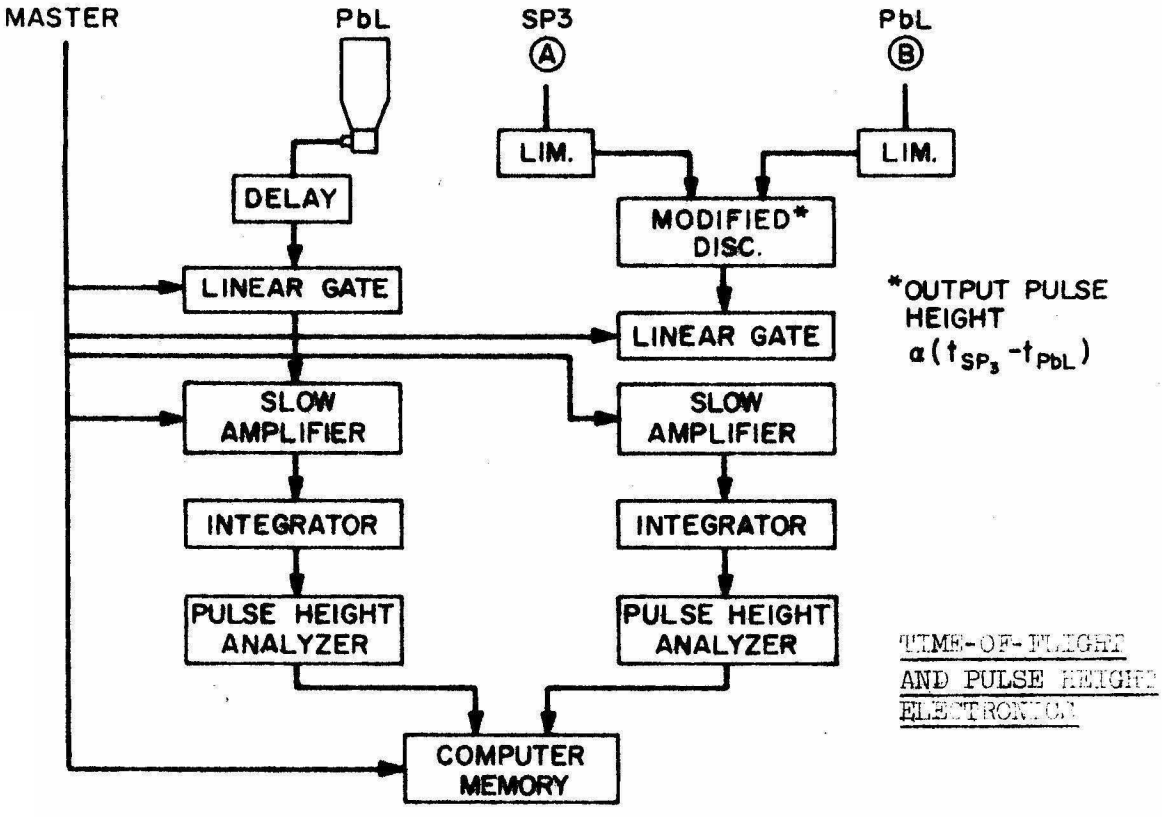

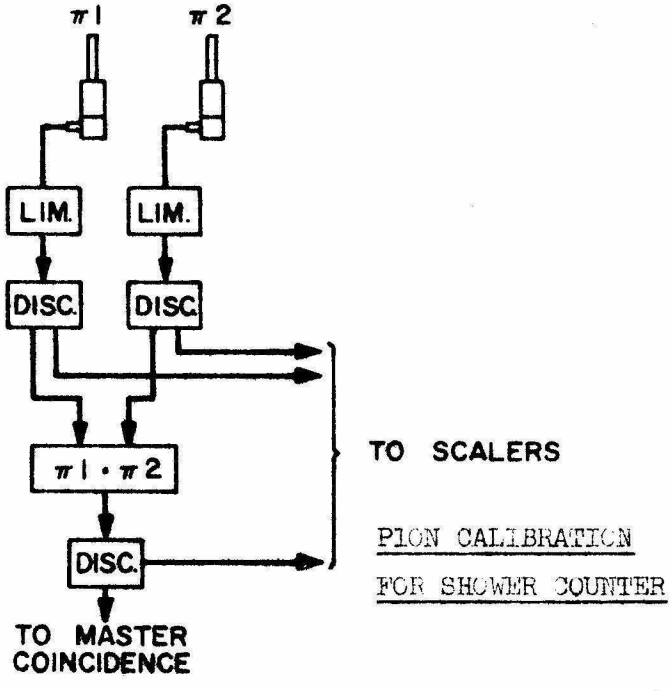

Figure 6.7 B: Readout and calibration system.

width of 25 nsec. determined by the width of the standard discriminator output. The counting rates combined with such typical delay curve width gave negligible accidental coincidence rates at all levels of the logic and kept the dead time corrections down to a minimum (see Table 6.2).

The master trigger initiated a series of actions:

(1) The wire chambers were triggered.

(2) The locations of sparks and fiducials of all wire chambers were recorded by means of the Lecroy digitizers.

(3) The pulse height of the shower counter and the time-of-flight between the third proton scintillation counter and the shower counter were digitized in a 256 channel pulse-height analyzer.

(4) The information of the previous event was dumped into the magnetic tape before the current event information occupied the data buffer of the on-line computer. In the meantime, the current event would be displayed on a RM 561 A oscilloscope.

The sequence of actions required approximately 300 msec. and was therefore limited to occurring once per beam pulse. To insure that a second master pulse did not occur during this time, a veto circuit prevented the master circuit from operation.

6.10 On-Line and Off-Line Check of System Performance

As mentioned at the beginning of Section 3, the PDP-5 computer, with its 4k memory and 6 microsecond cycle time, was too small to perform any programmed on-line check of the system performance. However,

with an average rate of as many as 2000 triggers per hour, visual and photographic-assisted methods were developed to monitor the system performance on a semi-on-line basis. The method was to give an immediate and reliable overall picture of the experiment.

When an event triggered the system, the information of fiducials and sparks was digitized and stored at the output data buffer of the PDP-5. This information, in the meantime, was displayed on a RM 561 oscilloscope. A typical display can be found in Figure 6.8-A. The number at the top left corner is the event number in decimal. V stands for the vertical view and H for the horizontal view. (Information in the vertical view actually comes from the horizontal conducting wires of wire chambers and vice versa.) The spacing between the chambers shown on the picture was not proportional to the actual distance in the laboratory. It merely gave a qualitative idea of the sequencing of the chambers. However, by constantly watching the display, it was easy to pick up failures (like, e.g., the second fiducial missing, multi-tracks in the front chambers, etc.).

To get an even better quantitative view of the performance, an additional display scope 535 was connected to the system showing the same display as the RM 561 A scope. By taking a multi-exposure picture of this display with a polaroid film, we were able to pin down not only the above mentioned trivial symptoms, but also the more subtle ones like the inefficiency of a particular chamber, the inefficiency of a certain region of a chamber, edge sparks, wands' failures, and even the mismatch of signal cables to the Lecroy digitizers (there were 56 signal cables).

Figure 6.8-C shows a typical multi-track picture. The systematic variation of the track length in the horizontal view of the range chamber clearly indicates the influence of the sweeping magnet. Those with longer range are less bent and have higher energy, and vice versa.

Aside from these two semi-on-line checks, options were built into the displaying program so that the accumulated shower counter pulse height distribution and the time-of-flight distribution could also be immediately displayed on the oscilloscope. A run with clean π^0 triggers always resulted in well-behaved distributions. For instance, if there were too many points appearing beyond both shoulders of the peak of a time-of-flight distribution, it was a good indication that these were accidental background events, probably due to too intense a beam. Figure 6.10 shows a typical set of pulse height and time-of-flight distributions taken at the end of a run.

Among the first off-line checks of the system performance was the adaptability of the PDP generated magnetic tape to the IBM-360 machine. Although the PDP tape unit was built to be compatible with the IBM unit, there was a lot of worry as to how well the PDP generated tapes might be accepted. If a record of a tape was unreadable by IBM 360 unit, the rest of the tape might be completely disregarded. Fortunately, not a single tape was rejected because of incompatibility of of the two tape units.

A standard off-line check was to dump the contents of the first few hundred records of a tape into printed form. They were carefully examined. Any inconsistency would be thoroughly investigated.

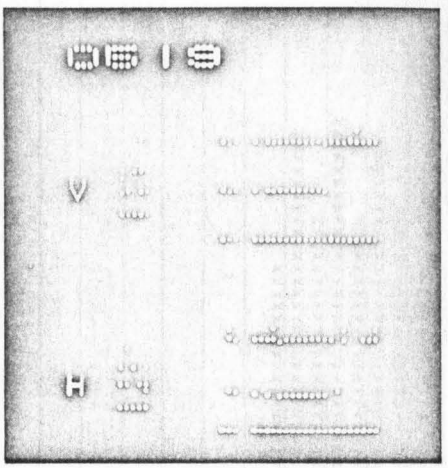

(A)

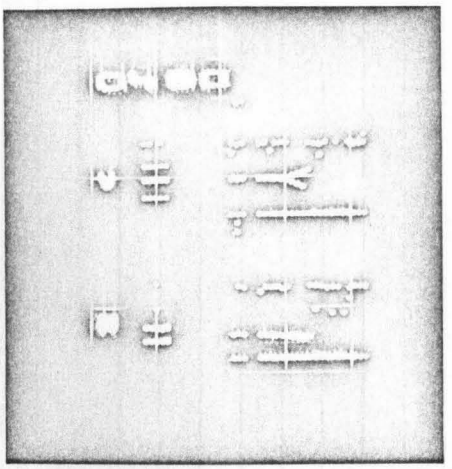

(B)

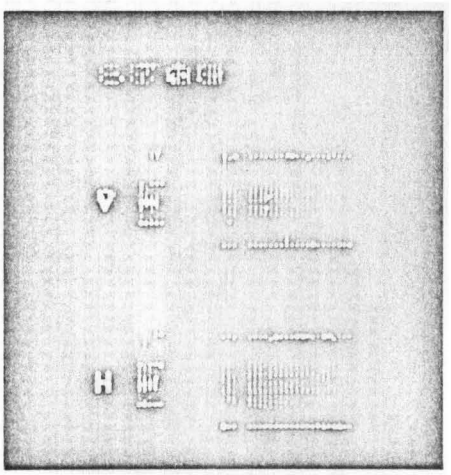

(C)

Figure 6.8 On-line event display (A) a p-C scattered event (B) a V-type event and (C) a multiple exposure of tracks.

Figure 6.9 A Pulse height distribution of shower counter in a typical run.

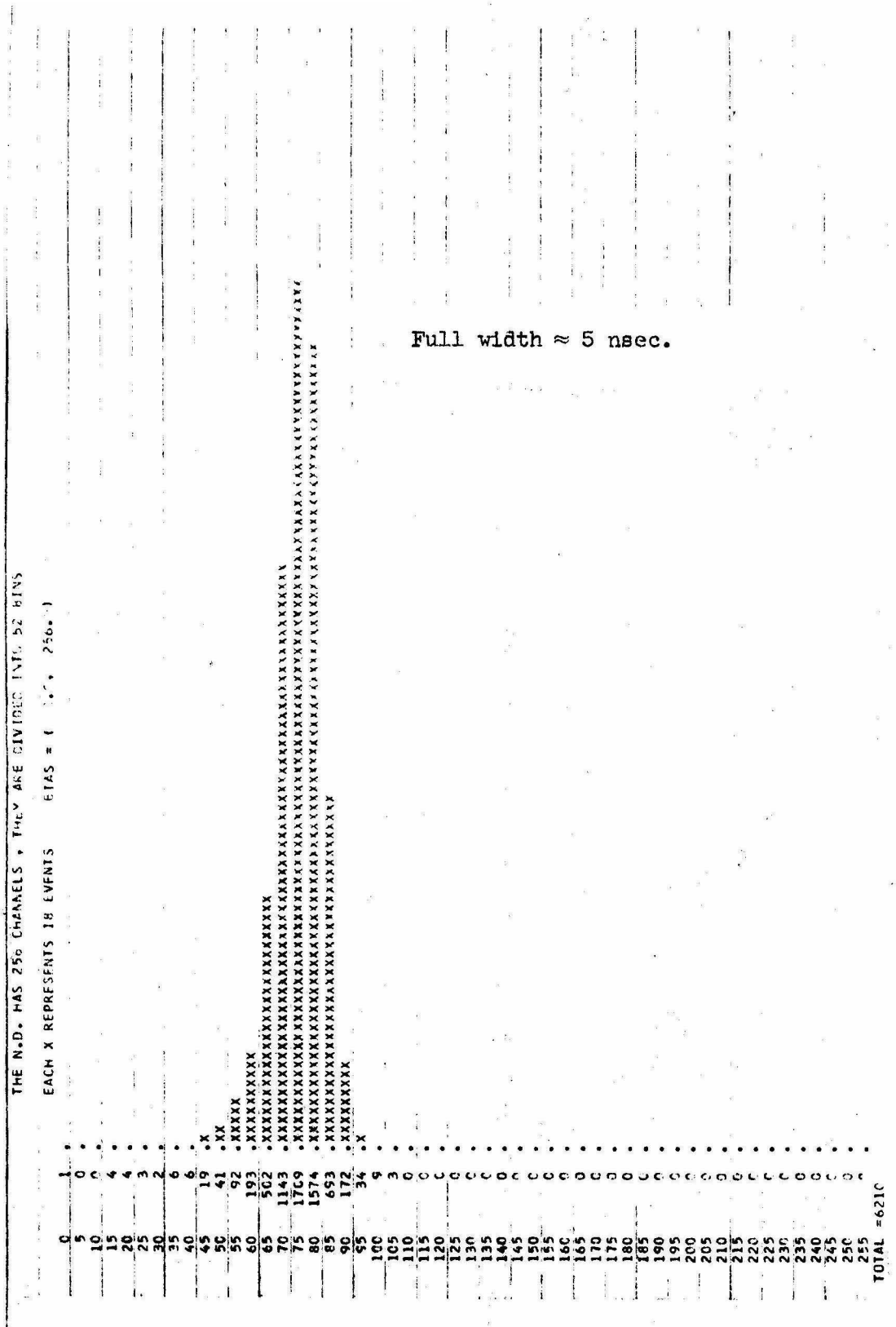

Full width ≈ 5 nsec.

Figure 6.9 B Time-of-flight distribution in a typical run.

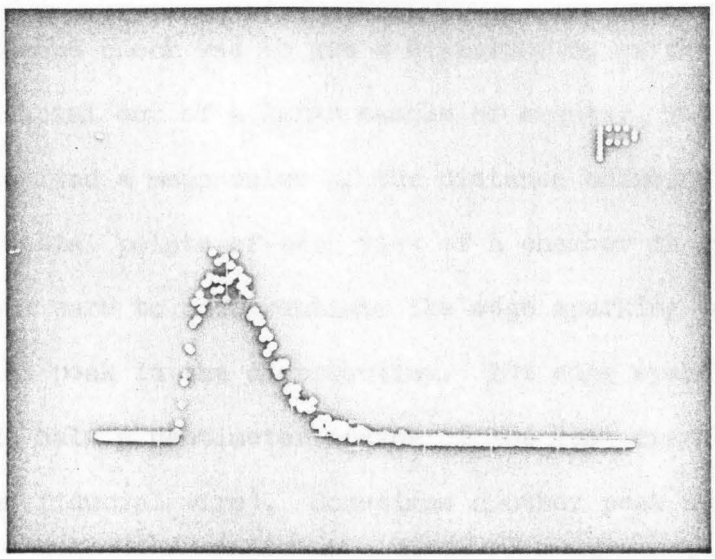

(A)

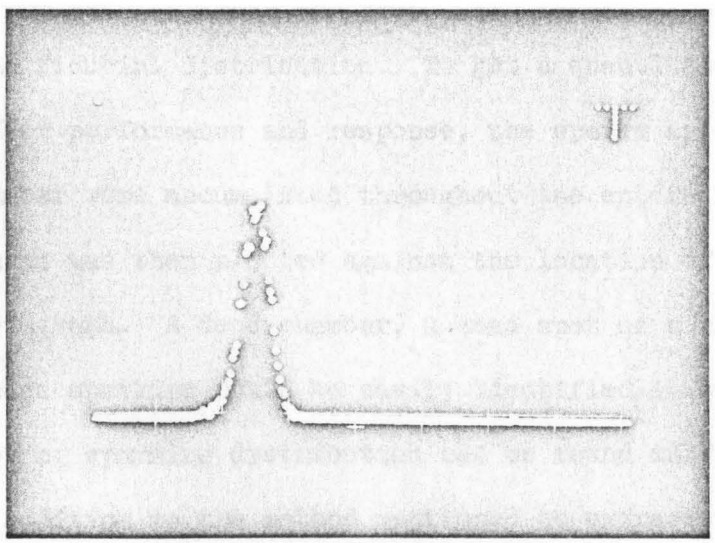

(B)

Figure 6.10 On-line (A) lead-lucite counter pulse height distribution and (B) time-of-flight distribution.

During the experiment, certain minor malfunctions of the Lecroy digitizers were discovered through this kind of check.

A second check was to get a distribution of the locations of the second fiducial out of a large sample of events. The primary purpose was to find a mean value of the distance between the first and the second fiducial points of each view of a chamber in quartz clock units. We took care to differentiate the edge sparking peak from the second fiducial peak in the distribution. The edge spark usually appeared about half a centimeter inside of the last conducting wire (or the second fiducial wire). Sometimes another peak appeared behind the second fiducial peak, corresponding to the reflected spark signals, due to an imperfection of the damping device on the other side of the magnetostrictive ribbon. Should an ambiguity arise as to which peak was the right one, it always helped if more tapes of the same geometrical setting were searched and compared. Figure 6.11 shows a typical second fiducial distribution. To get a quantitative idea of the wire chamber performance and response, the sparks appearing in one view of a chamber were accumulated throughout the entire run. The number of sparks was then plotted against the location of its appearance in a histograph. A dead chamber, a dead spot of a chamber, or a region of edge sparking could be easily identified in such a plot. A typical plot of sparking distribution can be found in Figure 6.12.

In addition to the method mentioned to extract the system performance by correlating a large number of sample events, one could inspect the event on an individual basis by either playing back the magnetic tape for an oscilloscope display or call the "CAL-COMP"

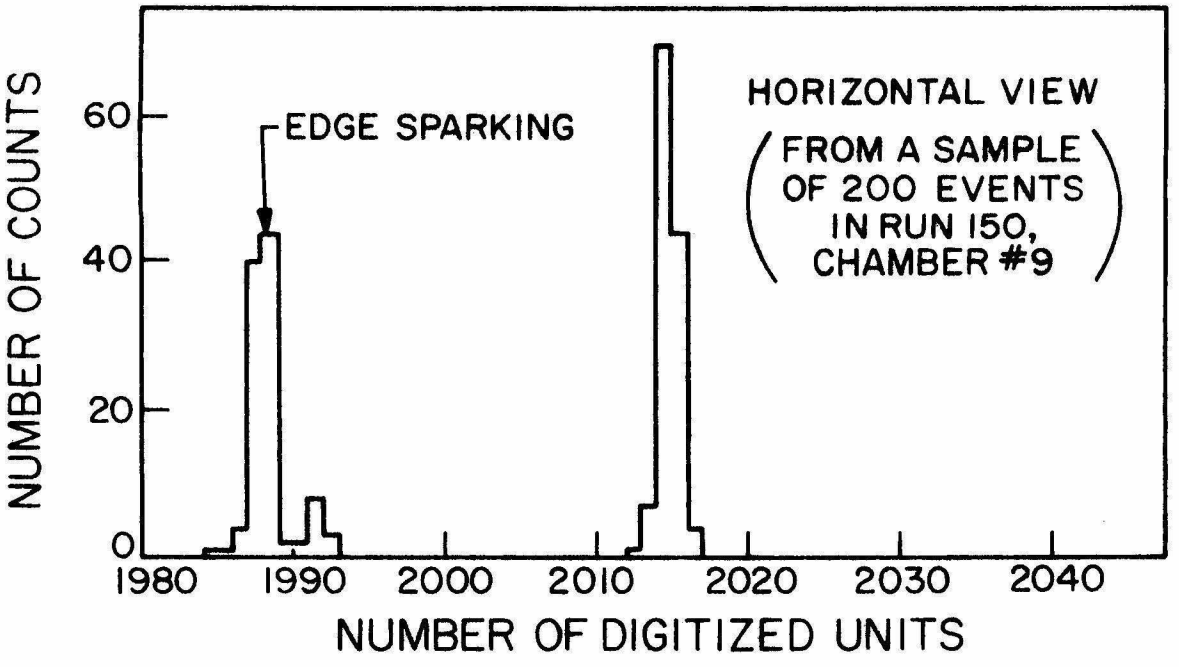

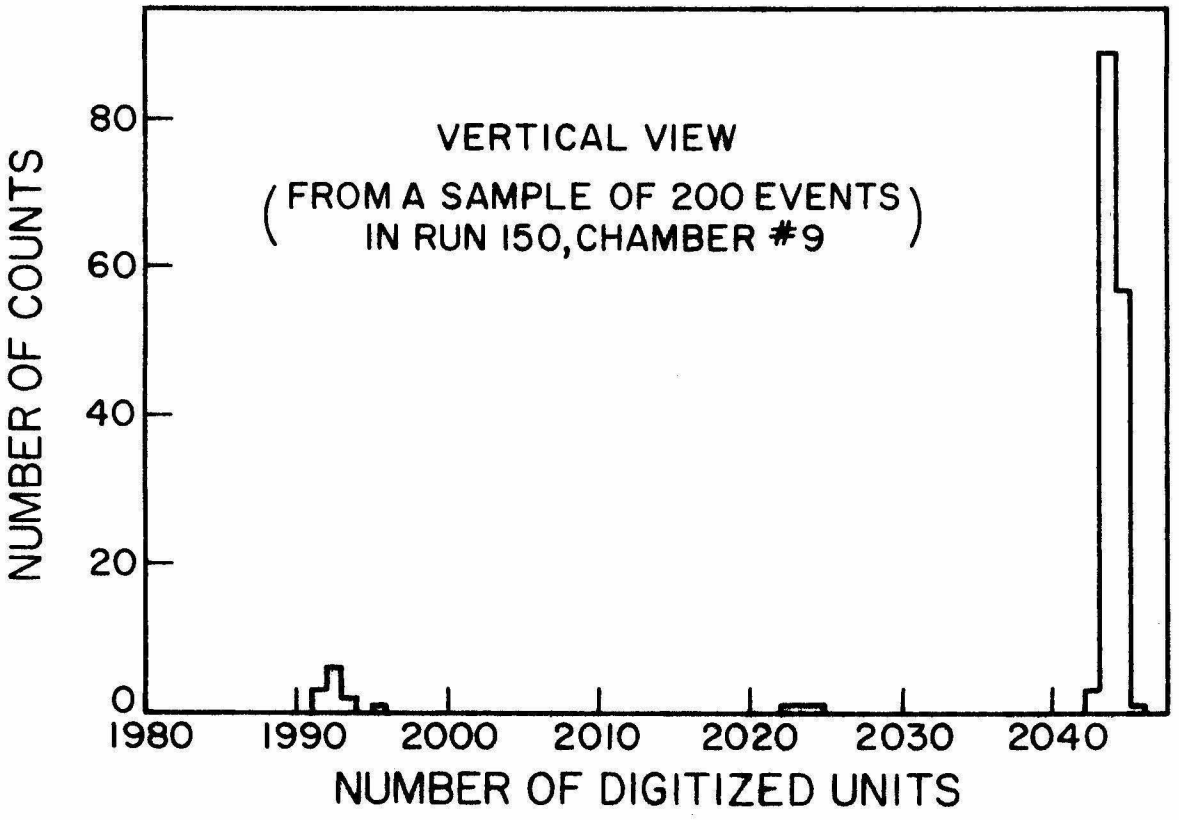

Figure 6.11 Distribution of second fiducial locations.

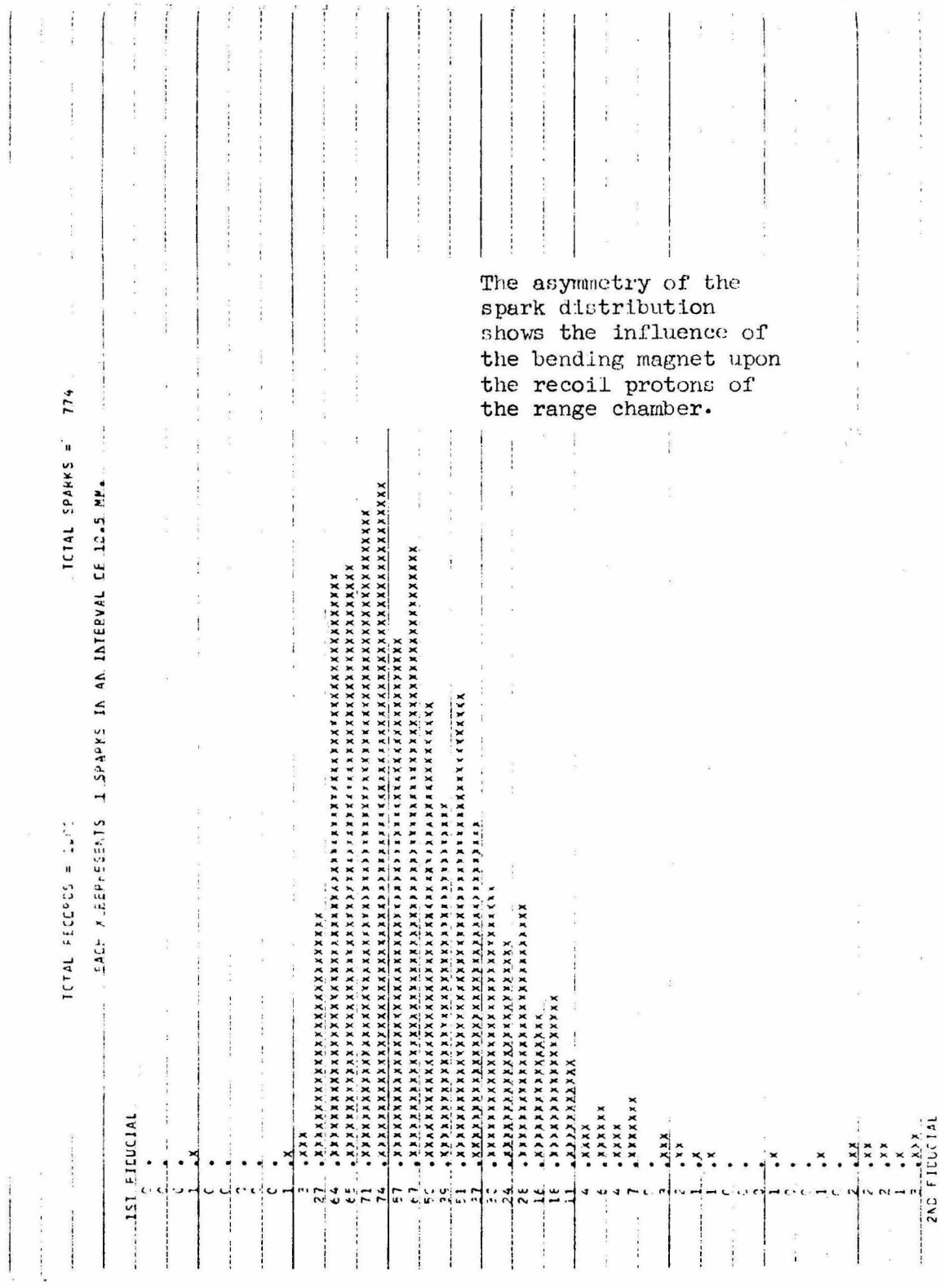

The asymmetry of the spark distribution shows the influence of the bending magnet upon the recoil protons of the range chamber.

Figure 6.12 A: Spark distribution in the horizontal view of a typical wire chamber.

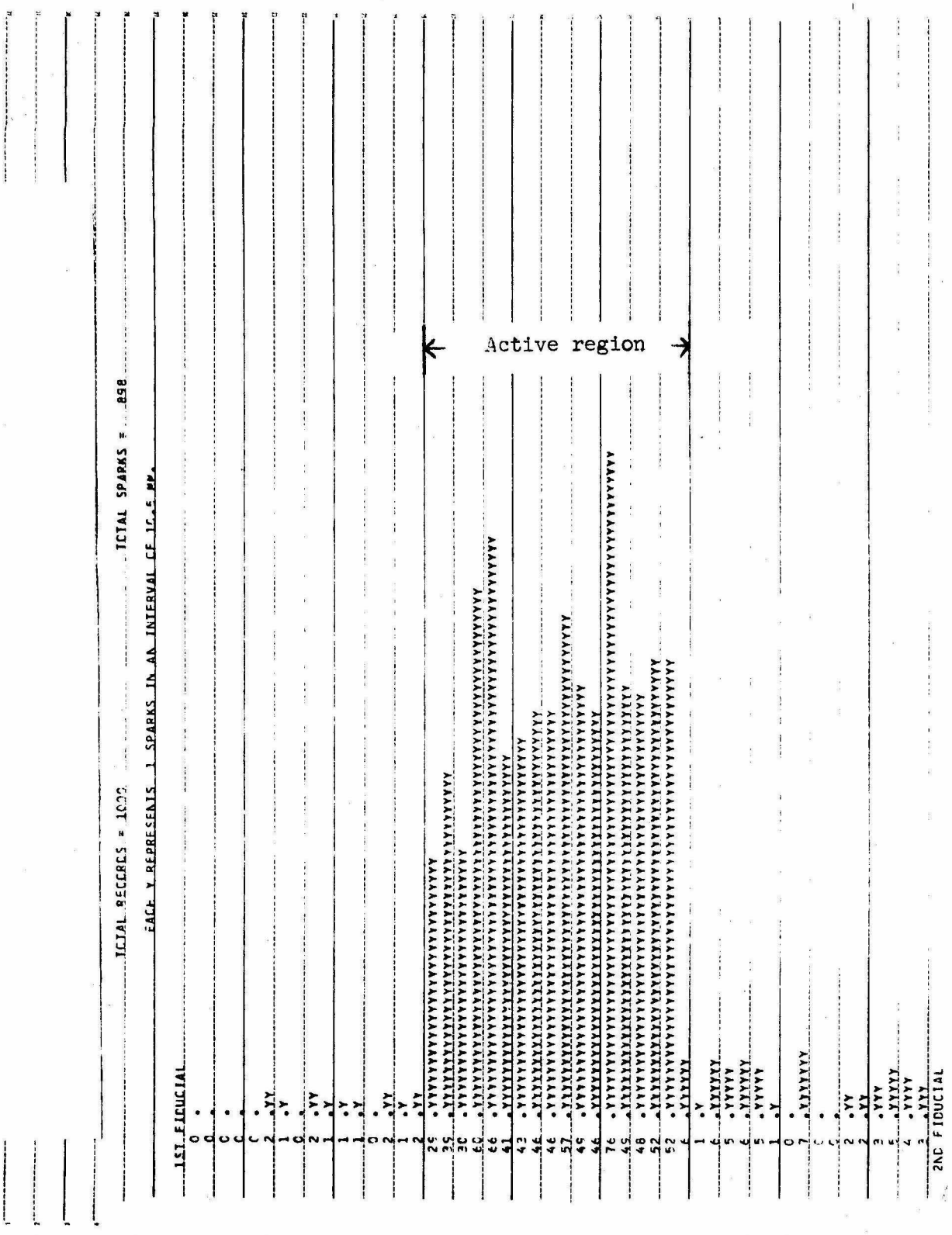

Figure 6.12 B Spark distribution in the vertical view of a typical wire chamber.

plotter in the computing center to make an exact scale plot for the particular event in question. The latter method, though very expensive ($1 per event), provided the best qualitative means to perfect the techniques of the track recognition schemes. Figure 3.1 shows such plots with computer-found tracks drawn on top of the raw sparks.

6.11 Proton Energy Determination

A. Wire Orbiting Calibration of Proton Momentum in a Bending Magnet

The recoil proton momentum of this experiment was first determined by a bending magnet. In a given magnet configuration (or a certain fixed field strength) with known trajectories of the recoil proton before and after the bending magnet, we were able to calculate the proton momentum provided a thorough momentum calibration was done before the experiment. In the past, trajectories were measured visually and individually. This is not only time consuming, but also inaccurate; the fitted coefficients usually reproduced the momentum to about 1%.

The method developed for this experiment was to combine the well-known floating wire technique of tracing particle orbits through magnetic fields and electronic readout using magnetostrictive delay lines similar to those used in wire spark chambers. The advantage lay in the rapid and accurate measurement of many particle trajectories in a short period of time. The use of magnetostrictive readout electronics eliminated the tedious work of measuring individual trajectories visually and provided a means by which the procedure could be computer

controlled.

Briefly, the magnetostrictive readout system was used to determine the position of the floating wire in the same way as it detected the position of a wire carrying current from a spark discharge in a wire chamber. Five magnetostrictive pickups were placed at known positions in the plane of the floating wire on both sides of the bending magnet. After the wire, with a D. C. current flowing in it, assumed its equilibrium trajectory through the magnet, a current pulse was sent down it which generated sound waves in the magnetostrictive ribbons. The time-of-flight of these sonic pulses with respect to the fiducial pulses was digitized and stored on magnetic tape by an on-line computer. Further analysis on an IBM 7094 computer used these data, plus the D. C. current, the tension of the wire, and the magnet configuration to generate the momentum calibration of the magnet. Thus, the calibration was conducted in quite the same way in which the magnet was used in an experiment to determine a particle's momentum. (14)

The floating wire technique is based on the fact that the curvature of a stretched D. C. current carrying wire in a magnetic field is the same as that of the trajectory of a charged particle of a particular momentum in the same magnetic field. Given a D. C. current I and tension T, and provided that the locations at which the floating wire is supported do not fall on the magnet foci, the resulting trajectory of the wire is that of a singly charged particle passing through those two fixed

points with momentum given by

$$p(\text{MeV/c}) = 2.94\ T\ (\text{gm})/\ I\ (\text{amp}). \qquad (6.11\text{-}1)$$

By varying the current or the tension, one is able to select trajectories of different momentum. By varying the positions of the fixed points, trajectories of different entrance and exit positions can be obtained. Thus, one can map out the entire family of trajectories of interest in a given magnet configuration. In the external region where no appreciable field exists, the trajectories are straight lines. We placed five magnetostrictive ribbon pickups at uniform spacings, parallel to one another, on the exit side and similarly on the entrance side of the magnet. The floating wire lay just at the surface of the pickup devices, lightly touching them (see Figure 6.13). To obtain the positions of the wire, a large instantaneous current pulse was superimposed on the steady D. C. current standing on the wire by discharging a capacitor through a spark gap connected to the floating wire. The fiducials which provided the start and stop signals for the electronics were placed at known positions at the beginning and the end of the magnetostrictive ribbon. Currents were induced in the fiducial wire by connecting separate capacitors to the spark gap, thus insuring that all signal currents were triggered at the same instant. The position of the floating wire was digitized by the Lecroy digitizers to an accuracy of about 0.2 mm. at five points at each side of the magnet.

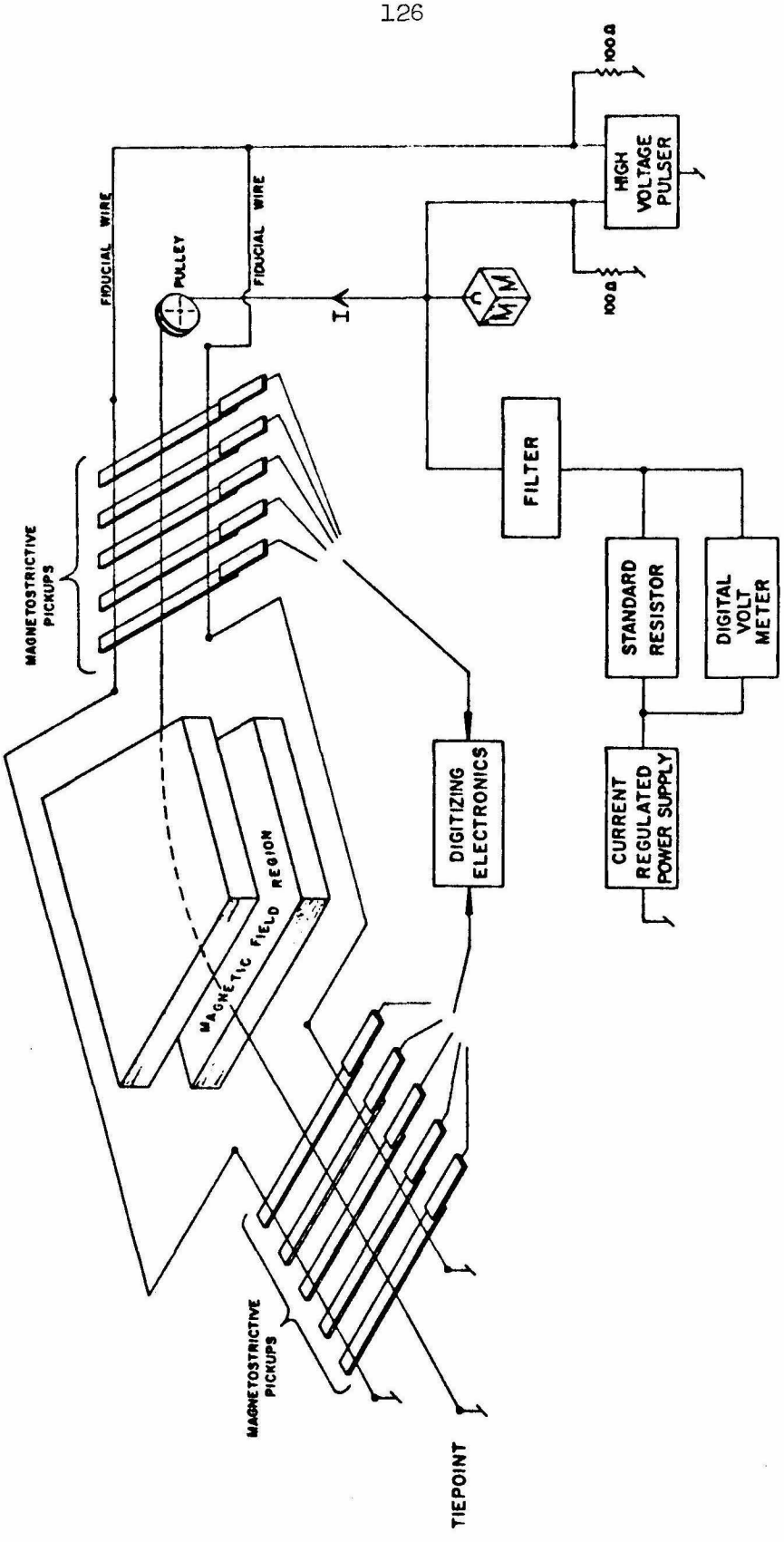

Figure 6.13 Wire orbiting calibration layout.

These values were used to fit two straight lines. The errors in a fit of the form

$$Y = mX + b \qquad (6.11\text{-}2)$$

for the external part of the trajectory were typically

$$\Delta m \approx \pm 0.004 \text{ and } \Delta b \approx \pm 0.08 \text{ mm.}$$

After finding the incoming and outgoing trajectories of the floating wire, a method was needed to fit the momentum using this information. Here only the method we used for the case of a simple bending magnet is described. No attempt is made to claim that this is a generalized method.

Consider a single trajectory through a region of magnetic field lying in a plane perpendicular to the field direction. The trajectory is uniquely defined by a position on the entrance and the exit sides and by an angle of bend. The momentum p is expressed by three parameters: x_1, x_2, and $\Delta m = (\tan \theta - \tan \theta_o)$ in the generalized form

$$p = f(x_1, x_2, \Delta m) \qquad (6.11\text{-}3)$$

A central momentum is chosen in which $x_1 = x_2 = 0$ and $\tan \theta = \tan \theta_o$, where θ_o is the angular bend of the central orbit (see Figure 6.14). The momentum of the central orbit is measured to be p_o. Expanding the $f(x_1, x_2, \Delta m)$ about p_o using Taylor's expansion gives

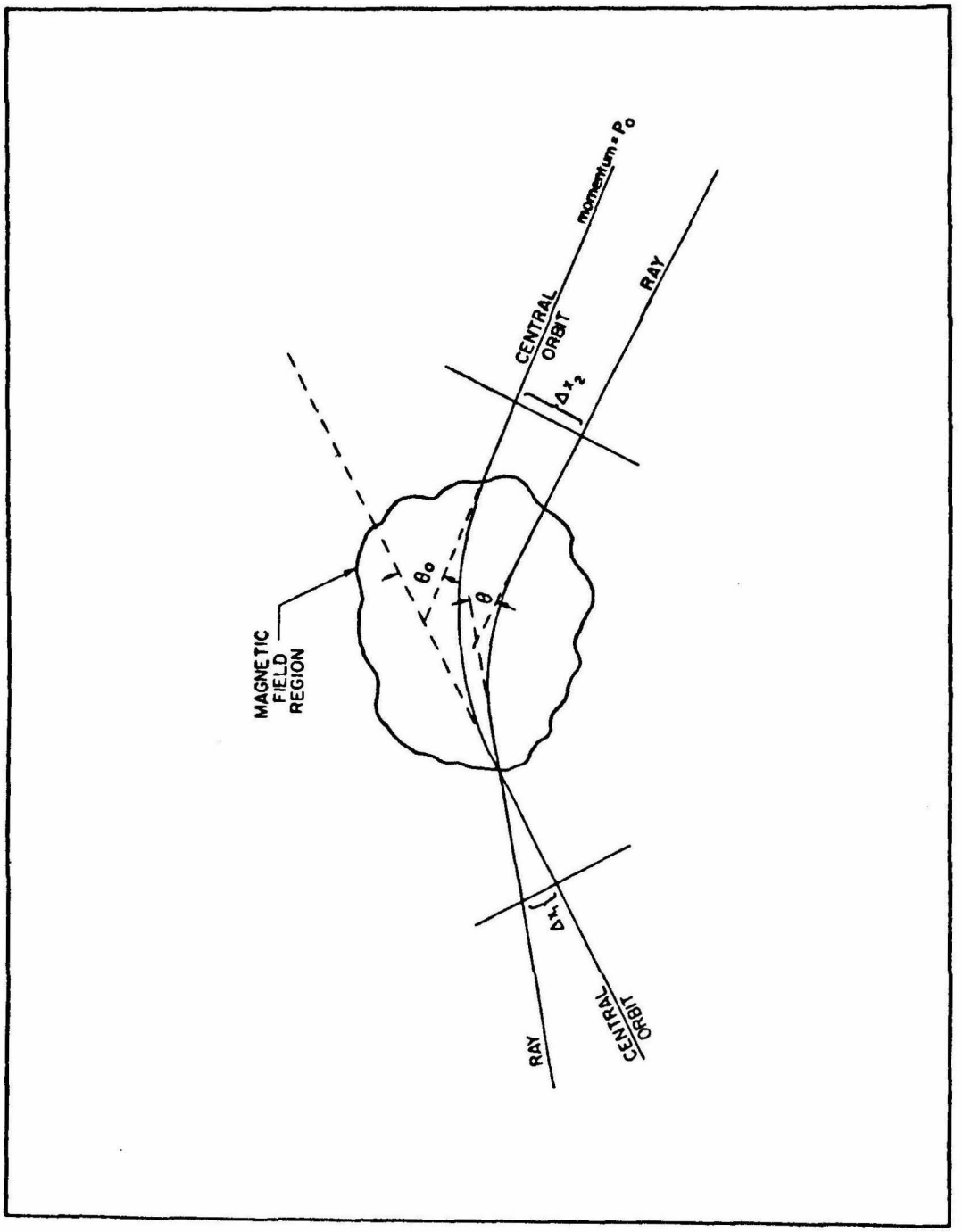

Figure 6.14 Definition of momentum fitting parameters.

$$p = p_o + a_1 x_1 + a_2 x_2 + a_3 \Delta m + a_4 x_1^2 + a_5 x_2^2 + \ldots \quad (6.11\text{-}4)$$

We kept all terms through fourth order in x_1, x_2 and Δm, and performed a least-squares fit to our data. Mathematically,

$$\begin{aligned} p_o &= f(0, 0, 0) \\ a_1 &= \left.\frac{\partial p}{\partial x_1}\right|_{x_2,\ \Delta m} \\ a_2 &= \left.\frac{\partial p}{\partial x_2}\right|_{x_1,\ \Delta m} \\ a_3 &= \left.\frac{\partial p}{\partial \Delta m}\right|_{x_1,\ x_2} \\ a_4 &= \left.\frac{\partial^2 p}{\partial x_1^2}\right|_{x_2,\ \Delta m} \\ &\text{etc.} \end{aligned} \quad (6.11\text{-}5)$$

There are 34 adjustable parameters to be fitted to a much greater number of separate trajectories. The ratio of the number of trajectories to that of the parameters was about 12 to 1. Clearly, the higher the ratio the better the reconstructed momentum. However, since the fitting scheme is only a mathematical one, the momentum fit is not guaranteed to be convergent if the parameters x_1, x_2 or Δm of a real trajectory fall outside the range of calibration. Events of this nature were discarded at the beginning of the momentum fit.

For particle trajectories not falling in the median plane of the bending magnet, the magnetic field in the region of the

fringe fields will be different from that seen in the median plane. However, to first order in the pitched angle, the corrections to the fitted coefficients vanish. For best results, wire orbits should be chosen which uniformly span the ranges of x_1, x_2 and Δm.

The various orbits measured covered a momentum range of 400 MeV/c to 1200 MeV/c in three magnet configurations with a certain region (600 to 1000 MeV/c) overlapped. Using the coefficients calculated by the least square fittings, we can obtain a p (calc.) for each orbit. From the measured values of the D. C. current and the tension in the floating wire, we can also obtain a value p (meas.) from equation (6.11-1). The quantity

$$\delta = \frac{p(\text{calc.}) - p(\text{meas.})}{p_o} \qquad (6.11\text{-}6)$$

is an indication of the goodness of the fit. Figure 6.15 shows that the accuracy of the fit in a typical magnet configuration is good. The p(calc.) agreed with the p(meas.) to about 0.2%.

B. Energy Calculation From Range Measurement

A fast-moving charged particle loses energy via electromagnetic interactions when passing through matter. The range energy relation for a given material enables us to caluclate one quantity if we know the other. This relationship allows the determination of the proton energy. The total range was calculated from the point of π^o production all the way to where it stopped. The total range, containing liquid hydrogen, air,

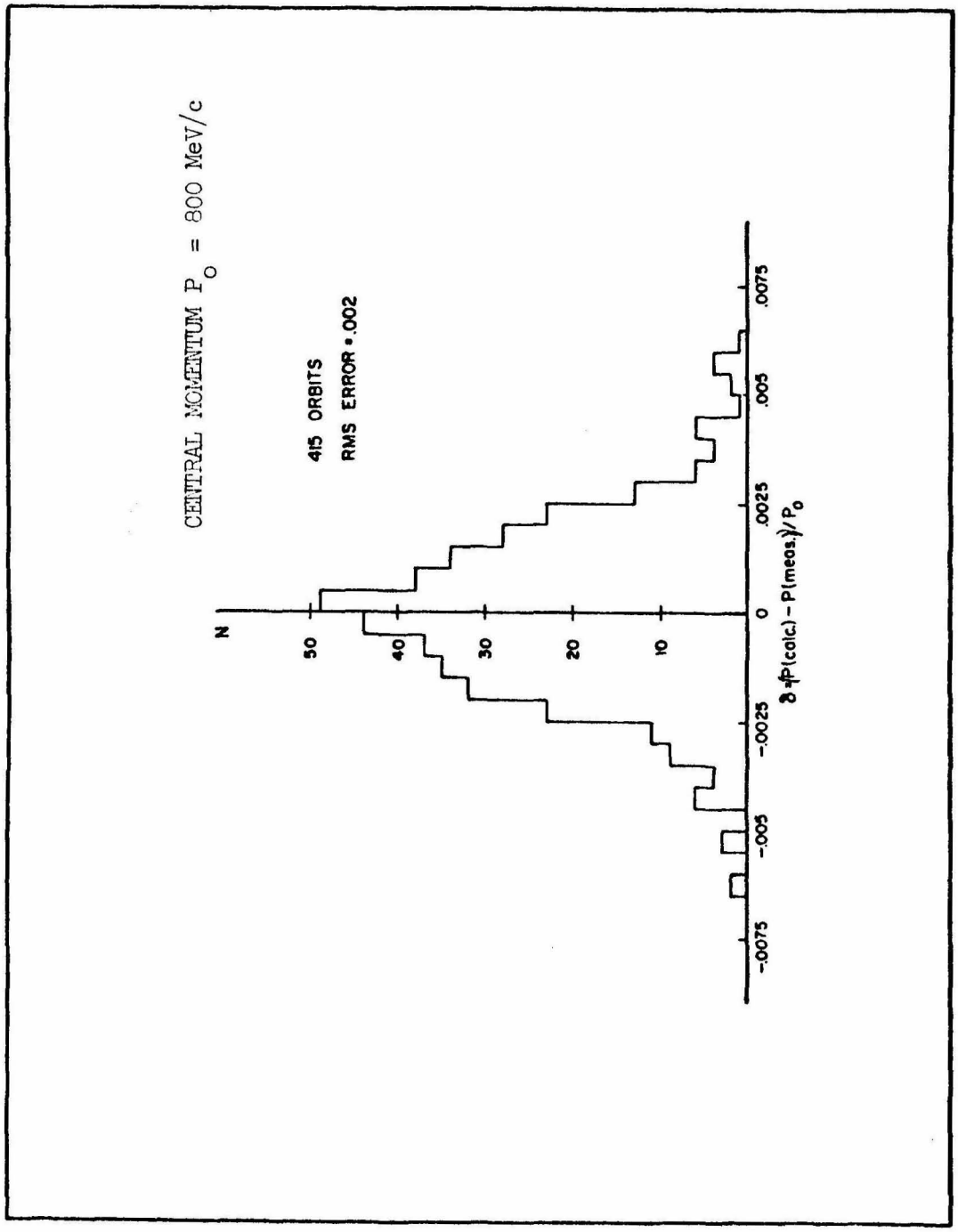

Figure 6.15 Accuracy of the momentum fitting.

mylar, scintillator, masking tape, and carbon was then converted into an equivalent amount of carbon in gm/cm^2 . The point of π^o production in principle could be anywhere in the target; the trajectory in the front chambers could only suggest which direction the proton recoiled from. The multiple scattering in the front chambers might even make it seem as if the recoil proton trajectory missed the target. To simplify the situation, we always considered the center of target as the starting point of the range calculation. This is justified because the range measurement in the chamber intrinsically had an uncertainty of the order of 2 gm/cm^2 carbon while the uncertainty of the point of π^o production was on the order of 0.1 gm/cm^2 liquid hydrogen. (Liquid hydrogen density $\approx$ 0.07 gm/cm^3.)

The range energy relation was expressed empirically in the form

$$\log T_p = \sum_{i=1}^{4} A_i [\log_{10} (R + \Delta R)]^{i-1} \qquad (6.11\text{-}7)$$

where ΔR and A_i's are constants, R is the range in gm/cm^2 of carbon equivalent, T_p is the proton kinetic energy in MeV. The coefficients reproduced the proton kinetic energy to within 0.03%, provided the measurement of R was exact.

C. Comparison of the Two Methods

If a recoil proton stopped inside the range chamber, our program provided two schemes to calculate its energy. A comparison of the results would indicate the accuracy of the fits

As mentioned in Section A, the percentage deviation of the momentum fit using the wire orbiting calibration method was 0.2% (which amounted to at most 0.4% in the deviation of kinetic energy in the non-relativistic limit, while in the relativistic limit $T_p \sim p_p$, $\Delta T_p/T_p \approx \Delta p/p_p \approx 0.2\%$). For a typical incoming proton with T_p = 300 MeV, the uncertainty would amount to 1.2 MeV. This uncertainty was increased because the intrinsic uncertainty of the locations of the wire chambers and the multiple scattering all tended to obscure the trajectories. However, the uncertainty of the proton kinetic energy derived by the wire orbiting method was estimated to be on the order of 1%.

The major uncertainty of the proton kinetic energy derived by the range energy relation came from the fact that there was no way of knowing the exact location of the proton's stopping point. The amount of carbon between two adjacent wire chambers was typically 2.0 gm/cm^2, which corresponds to roughly 10 MeV in the kinetic energy region covered.

Figure 6.16-A shows a plot of number of events against $\Delta T_p = T_p(\text{Mag}) - T_p(\text{Range})$ for the nonscattered events. The plot is well centered at zero, and the width of the distribution is roughly 15 MeV as expected. Such distribution was calculated for every tape processed. The center of the distribution was never off by more than 5 MeV and the width was always between 10 and 20 MeV, with 15 MeV the most frequent value.

Therefore, the kinetic energy of a proton stopping inside

```
                                        DTP     DISTRIBUTION

              RUN # = 132                                    DTP = TPRNG-TPMAG

                              EACH X REPRESENTS    9  EVENTS IN AN INTERVAL OF   0.500E 01

     DIFF      # EVENT
  -190.0000     0  .
  -185.0000     0  .
  -180.0000     0  .
  -175.0000     1  .
  -170.0000     0  .
  -165.0000     1  .
  -160.0000     1  .
  -155.0000     1  .
  -150.0000     1  .
  -145.0000     0  .
  -140.0000     0  .
  -135.0000     2  .
  -130.0000     2  .
  -125.0000     3  .
  -120.0000     4  .
  -115.0000     4  .
  -110.0000     8  .
  -105.0000     5  .
  -100.0000     9  .X
   -95.0000    10  .X
   -90.0000    14  .X
   -85.0000    12  .X
   -80.0000    11  .X
   -75.0000    15  .X
   -70.0000    12  .X
   -65.0000    24  .XX
   -60.0000    35  .XXX
   -55.0000    32  .XXX
   -50.0000    48  .XXXXX
   -45.0000    46  .XXXXX
   -40.0000    50  .XXXXX
   -35.0000    65  .XXXXXXX
   -30.0000   106  .XXXXXXXXXXX
   -25.0000   131  .XXXXXXXXXXXXXX
   -20.0000   188  .XXXXXXXXXXXXXXXXXXXX
   -15.0000   347  .XXXXXXXXXXXXXXXXXXXXXXXXXXXXXXXXXXXXXX
   -10.0000   549  .XXXXXXXXXXXXXXXXXXXXXXXXXXXXXXXXXXXXXXXXXXXXXXXXXXXXXXXXXXXXX
    -5.0000   769  .XXXXXXXXXXXXXXXXXXXXXXXXXXXXXXXXXXXXXXXXXXXXXXXXXXXXXXXXXXXXXXXXXXXXXXXXXXXXXXXXXXXXX
     0.0      897  .XXXXXXXXXXXXXXXXXXXXXXXXXXXXXXXXXXXXXXXXXXXXXXXXXXXXXXXXXXXXXXXXXXXXXXXXXXXXXXXXXXXXXXXXXXXXXXXXXXXXXXX
     5.0000   590  .XXXXXXXXXXXXXXXXXXXXXXXXXXXXXXXXXXXXXXXXXXXXXXXXXXXXXXXXXXXXXXXXX
    10.0000   362  .XXXXXXXXXXXXXXXXXXXXXXXXXXXXXXXXXXXXXXXX
    15.0000   153  .XXXXXXXXXXXXXXXXX
    20.0000    86  .XXXXXXXXX
    25.0000    47  .XXXXX
    30.0000    31  .XXX
    35.0000    19  .XX
    40.0000    15  .X
    45.0000    13  .X
    50.0000     3  .
    55.0000     3  .
    60.0000    26  .XX

 TOTAL = 4751
```

Figure 6.16 A: Proton energy resolution for non p-C scattered events in a typical run.

INELASTICITY DISTRIBUTION

RUN # = 67 INELAS. = TPI-TPRNG (MEV)

EACH X REPRESENTS 1 EVENTS IN AN INTERVAL OF 0.500E 01

DIFF	# EVENT	
-60.0000	10	.XXXXXXXXX
-55.0000	4	.XXXX
-50.0000	1	.X
-45.0000	4	.XXXX
-40.0000	5	.XXXXX
-35.0000	11	.XXXXXXXXXX
-30.0000	11	.XXXXXXXXXX
-25.0000	18	.XXXXXXXXXXXXXXXXX
-20.0000	26	.XXXXXXXXXXXXXXXXXXXXXXXXX
-15.0000	24	.XXXXXXXXXXXXXXXXXXXXXXX
-10.0000	27	.XXXXXXXXXXXXXXXXXXXXXXXXXX
-5.0000	38	.XXXXXXXXXXXXXXXXXXXXXXXXXXXXXXXXXX
0.0	37	.XXXXXXXXXXXXXXXXXXXXXXXXXXXXXXXXX
5.0000	39	.XXXXXXXXXXXXXXXXXXXXXXXXXXXXXXXXXXX
10.0000	42	.XXXXXXXXXXXXXXXXXXXXXXXXXXXXXXXXXXXXXX
15.0000	32	.XXXXXXXXXXXXXXXXXXXXXXXXXXXXX
20.0000	32	.XXXXXXXXXXXXXXXXXXXXXXXXXXXXX
25.0000	25	.XXXXXXXXXXXXXXXXXXXXXXXXX
30.0000	21	.XXXXXXXXXXXXXXXXXXXX
35.0000	20	.XXXXXXXXXXXXXXXXXXX
40.0000	16	.XXXXXXXXXXXXXXXX
45.0000	25	.XXXXXXXXXXXXXXXXXXXXXXXXX
50.0000	11	.XXXXXXXXXXX
55.0000	9	.XXXXXXXXX
60.0000	13	.XXXXXXXXXXXXX
65.0000	13	.XXXXXXXXXXXXX
70.0000	10	.XXXXXXXXXX
75.0000	10	.XXXXXXXXXX
80.0000	9	.XXXXXXXXX
85.0000	4	.XXXX
90.0000	10	.XXXXXXXXXX
95.0000	3	.XXX
100.0000	3	.XXX
105.0000	5	.XXXXX
110.0000	6	.XXXXXX
115.0000	6	.XXXXXX
120.0000	1	.X
125.0000	6	.XXXXXX
130.0000	5	.XXXXX
135.0000	2	.XX
140.0000	2	.XX
145.0000	1	.X
150.0000	0	.
155.0000	0	.
160.0000	1	.X
165.0000	3	.XXX
170.0000	2	.XX
175.0000	1	.X
180.0000	0	.
185.0000	0	.
190.0000	2	.XX

TOTAL = 604

Figure 6.16 B: Inelasticity distribution for p-C scattered events.

the range chamber could be determined by two methods with the understanding that the wire orbiting method provided a more reliable result.

However, the events in which the information of the recoil proton polarization might be derived are those scattered inside the range house. The proton carbon scattering may be accompanied by a certain energy loss (inelastic scattering). For this type of events, the range measurement alone was not sufficient to determine the proton energy. Therefore, the incoming proton energy could only be determined by the wire orbiting method. By integrating along the path to the scattering vertex using the dE/dX relation we were able to find the proton energy before the interaction. If the scattered track was stopped inside the range chamber, the energy corresponding to the scattered track could be easily found by the same set of range energy relation coefficients in Equation (6.11-7). Aside from a small correction due to the recoil energy of the C nucleus which seldom exceeded 1 MeV, the difference of these two energies is called the inelasticity of the p-C scattering. Figure 6.16-B shows a typical inelasticity distribution. Aside from the elastic peak there is a long tail in the positive side which corresponds to the superimposed effect of inelastic events. The inelasticity of a p-C scatter was generally needed to find the carbon analyzing power; a more detailed description will be found in Appendix 6.14. Thus, for the p-C scattered events (or the events of interest), both methods of energy determination were used in a complementary

fashion.

D. Reconstruction of Bremsstrahlung Energy Spectrum

Once the recoil proton momentum was calculated by the wire orbiting method, it was used to reconstruct the incident photon energy. To find the kinematics of the two body reaction

$$\gamma + p \dashrightarrow \pi^{o} + p, \qquad (6.11\text{-}8)$$

we need three unknown parameters: the photon energy k, the π^{o} momentum, and its production angle with respect to the photon beam in the laboratory system. All the rest of kinematical quantities are known. By relating these qunatities with the law of conservation of energy and that of momentum in the production plane, we can obtain the three needed constraints.

The reconstructed photon energy can be expressed in terms of the known quantities in the form

$$k = \frac{m_{\pi}^{2}/2 + m_{p}T_{p}}{p_{p}\cos\theta_{p} - T_{p}} \qquad (6.11\text{-}9)$$

where θ_{p} is the recoil proton angle with respect to the photon beam in the laboratory system.

By accumulating k's over a large number of events, we reconstructed the bremsstrahlung energy distribution (see Figure 6.17). Since the experiment was contaminated by a few percent background events from Compton scattering and $2\pi^{o}$ photoproduction, the calculated k according to Equation 6.11-9 for the Compton

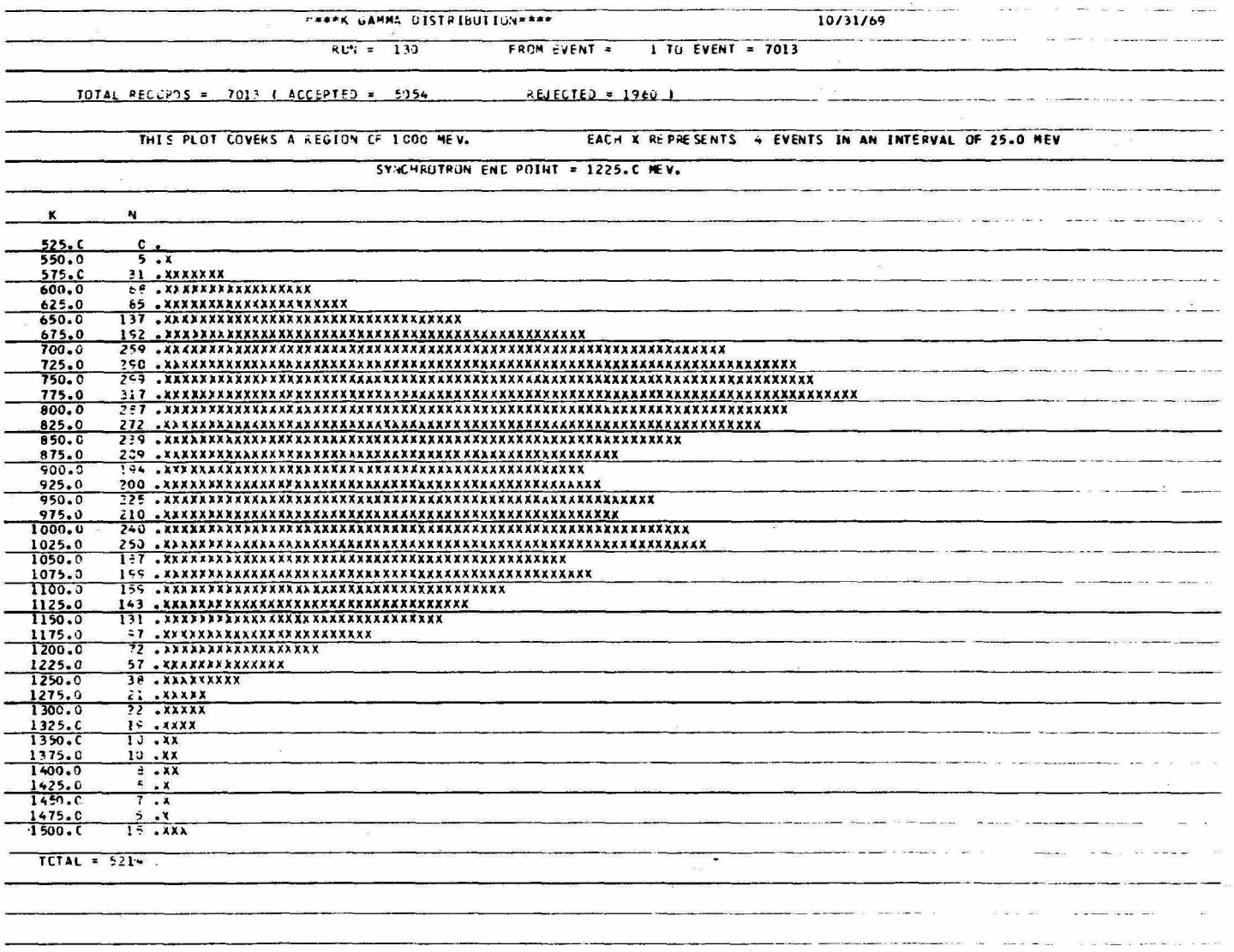

****K GAMMA DISTRIBUTION**** 10/31/69

RUN = 130 FROM EVENT = 1 TO EVENT = 7013

TOTAL RECORDS = 7013 (ACCEPTED = 5054 REJECTED = 1960)

THIS PLOT COVERS A REGION OF 1000 MEV. EACH X REPRESENTS 4 EVENTS IN AN INTERVAL OF 25.0 MEV

SYNCHROTRON END POINT = 1225.0 MEV.

K	N	
525.0	0	.
550.0	5	.X
575.0	31	.XXXXXXX
600.0	68	.XXXXXXXXXXXXXXXX
625.0	85	.XXXXXXXXXXXXXXXXXXXX
650.0	137	.XXXXXXXXXXXXXXXXXXXXXXXXXXXXXXXX
675.0	152	.XXXXXXXXXXXXXXXXXXXXXXXXXXXXXXXXXXXXXXXXXXXX
700.0	259	.XXXXXXXXXXXXXXXXXXXXXXXXXXXXXXXXXXXXXXXXXXXXXXXXXXXXXXXXXXXXXXXXXXXX
725.0	250	.XXXXXXXXXXXXXXXXXXXXXXXXXXXXXXXXXXXXXXXXXXXXXXXXXXXXXXXXXXXXXXXXXXXXXXXXXXXX
750.0	269	.XXXXXXXXXXXXXXXXXXXXXXXXXXXXXXXXXXXXXXXXXXXXXXXXXXXXXXXXXXXXXXXXXXXXXXXXXXXXXXXXX
775.0	317	.XXXXXXXXXXXXXXXXXXXXXXXXXXXXXXXXXXXXXXXXXXXXXXXXXXXXXXXXXXXXXXXXXXXXXXXXXXXXXXXXXXXXXXXXXXX
800.0	257	.XXXXXXXXXXXXXXXXXXXXXXXXXXXXXXXXXXXXXXXXXXXXXXXXXXXXXXXXXXXXXXXXXXXXXXXXXXXXXXXXXXXX
825.0	272	.XXXXXXXXXXXXXXXXXXXXXXXXXXXXXXXXXXXXXXXXXXXXXXXXXXXXXXXXXXXXXXXXXXXXXXXXXXXXXXXXXXXXXXX
850.0	239	.XXXXXXXXXXXXXXXXXXXXXXXXXXXXXXXXXXXXXXXXXXXXXXXXXXXXXXXXXXXXXXXXXXXXXXXXXXXXXXX
875.0	209	.XXXXXXXXXXXXXXXXXXXXXXXXXXXXXXXXXXXXXXXXXXXXXXXXXXXXXXXXXXXXXXXXXXXXXXXXXXXX
900.0	194	.XXXXXXXXXXXXXXXXXXXXXXXXXXXXXXXXXXXXXXXXXXXXXXXXXXXXXXXXXXXXXXXXXXXXX
925.0	200	.XXXXXXXXXXXXXXXXXXXXXXXXXXXXXXXXXXXXXXXXXXXXXXXXXXXXXXXXXXXXXXXXXXXXXXXXX
950.0	225	.XXXXXXXXXXXXXXXXXXXXXXXXXXXXXXXXXXXXXXXXXXXXXXXXXXXXXXXXXXXXXXXXXXXXXXXXXXXXXXXX
975.0	210	.XXXXXXXXXXXXXXXXXXXXXXXXXXXXXXXXXXXXXXXXXXXXXXXXXXXXXXXXXXXXXXXXXXXXXXX
1000.0	240	.XXXXXXXXXXXXXXXXXXXXXXXXXXXXXXXXXXXXXXXXXXXXXXXXXXXXXXXXXXXXXXXXXXXXXXXXXXXXXXXXXXX
1025.0	250	.XXXXXXXXXXXXXXXXXXXXXXXXXXXXXXXXXXXXXXXXXXXXXXXXXXXXXXXXXXXXXXXXXXXXXXXXXXXXXXXXXXXXXXXXX
1050.0	187	.XXXXXXXXXXXXXXXXXXXXXXXXXXXXXXXXXXXXXXXXXXXXXXXXXXXXXXXXXXXXXXX
1075.0	199	.XXXXXXXXXXXXXXXXXXXXXXXXXXXXXXXXXXXXXXXXXXXXXXXXXXXXXXXXXXXXXXXXXXXXXXXXXXXXXXXXXXX
1100.0	159	.XXXXXXXXXXXXXXXXXXXXXXXXXXXXXXXXXXXXXXXXXXXXXXXXXXXXXXXXXXXXXXX
1125.0	143	.XXXXXXXXXXXXXXXXXXXXXXXXXXXXXXXXXXXXXXXXXXXXXXXXXXXXXXXXXXXXXX
1150.0	131	.XXXXXXXXXXXXXXXXXXXXXXXXXXXXXXXXXXXXXXXXXXXXXXXXXXXXXXXXXXXXXX
1175.0	87	.XXXXXXXXXXXXXXXXXXXXXXXXXXXXXXXXXXXXXXXXXXXXXXXXXXXXXXXXXXXXXX
1200.0	72	.XXXXXXXXXXXXXXXXXX
1225.0	57	.XXXXXXXXXXXXXX
1250.0	38	.XXXXXXXXX
1275.0	21	.XXXXX
1300.0	22	.XXXXX
1325.0	16	.XXXX
1350.0	10	.XX
1375.0	10	.XX
1400.0	8	.XX
1425.0	5	.X
1450.0	7	.X
1475.0	5	.X
1500.0	15	.XXX

TOTAL = 5214

Figure 6.17 Reconstructed incident photon energy distribution.

background tended to be too high (due to $m_\gamma = 0$). For $2\pi^o$ production Equation 6.11-9 would give too low a k value (a correct expression should replace m_π by $2\ m_\pi$). Since the bremsstrahlung spectrum is continuous, a small distortion due to the background did not show up strongly in the reconstructed spectrum. Therefore, it was difficult to impose any condition to get rid of the background events. The only bias applied was to remove events with reconstructed k greater than the synchrotron end point energy (see also Section 3.2). These events were presumably all of Compton scattering origin.

The uncertainty of k can be expressed in a differential form,

$$\Delta k = \frac{\partial k}{\partial T_p} \Delta T_p + \frac{\partial k}{\partial \theta_p} \Delta \theta_p \ . \qquad (6.11\text{-}10)$$

T_p is typically good to 1%. The contribution of the first term seldom exceeded 1 MeV in the kinematic region covered. Most of the uncertainty came from the second term. With $\Delta\theta_p \approx 0.3^o$ due to the multiple scattering between the H_2 target and the first front chamber, Δk ranged from 8 to 11 MeV.

The shape of the recontructed k distribution was determined mainly by a combination of π^o production differential cross section, the geometrical detection efficiency of the system, and the undistorted bremsstrahlung energy spectrum of electrons scattered off tantalum. The differential cross section of π^o photoproduction was unfolded from the calculated k distribution using the scheme described in Section 3.5.

6.12 System Introduced Asymmetry and Scanning Criteria

In a polarization experiment, one must be certain that no left/right bias is introduced by the experimental method, or by the handling of data. Several tests were made to be certain that there was no such a bias. The first consideration was the purity of events. As discussed in Section 2.5, the combined background of Compton scattering and multipion production was estimated to be on the order of 7 percent. The influence of this percentage on the proton polarization was not certain, but we were able to set an upper limit (see Section 4.1). We assumed that we started with a relatively pure sample of protons from single π^{o} photoproduction.

The efficiency for seeing protons scattered to the left or to the right might be a function of particle position in the range chamber. The main possible source of trouble consisted of scattered tracks leaving through the sides of the range chamber. For the data taken around θ^{*}_{π} = 63 degrees, no events were observed leaving the range chamber. At θ^{*}_{π} = 93 degrees the recoil protons were more energetic, and about 2 percent of them left through the sides of the range chamber after scattering. In order that these events would not present a potential source of left/right asymmetry, they were all disregarded for further use. After this biasing, a small residual asymmetry still could be retained. Because in the horizontal view, due to the influence of the bending magnet, the spark distribution was not uniform throughout the whole span, i.e., higher energy protons (or less bent protons) stayed in one side and the lower energy protons stayed on the other side (see Figure 6.12-A). Therefore, more high

energy protons would be removed for exiting the range chamber after p-C scattering than the low energy ones whose scattered tracks seldom had enough energy to escape the range chamber. The cancellation therefore was not expected to be perfect. However, the residual asymmetry thus introduced was estimated to be only a small fraction of the total 2 percent events. Their presence was at worst not expected to introduce errors anywhere near to the quoted errors of the polarizations (typically 10%). Other possible problems, such as the dependence of sparking efficiency, were found to be negligible. A misalignment of of the wire chambers might also cause a certain bias. An estimate was made displacing each wire chamber randomly by 0.02" (which was the accuracy of the wire chamber location). To carry out the estimate, a few points were picked up along a straight line, and then displaced randomly, perpendicular to the original line. A least-squares fit routine was then called upon to fit these displaced points into a straight line. The results showed an excellent agreement with the original one. The chi-square value of the fit was generally far less than that of a typical fit in a real event. The reason for this surprisingly small effect is the combined effect on the apparent spark location of the wire spacing (1 mm.) and the multiple scattering. The latter effect alone sometimes could be six times as bad as the misalignment of chambers.

One great advantage of using the wire chamber electronic readout system was that the data processing was completely computer handled. A possible preferential selection of left or right scattered events due to a visual scanning could thus be avoided. The cost of

data processing prohibited us from scanning every event twice. Therefore a well tested and well instructed scanning program was of the greatest importance. Several means of testing and checking were utilized to make certain that the scanning program was doing what it should do. The philosophy of the scanning scheme was to accept every event which satisfied the scanning criteria, at the same time trying to minimize the number of false events which leaked through the tests. It was estimated that 1/3 of the data processing cost was devoted to perfecting the line fitting and scanning scheme.

One of the criteria for event selection was the values of $\theta_p'^{H}$, $\theta_p'^{V}$; the p-C scattering angle (θ_p') projected on the horizontal or the vertical view in the laboratory. The limits allowed were 4 to 45 degrees in at least one view. In order to be included in the final polarization determination, an event had to have θ_p' between 4 and 30 degrees. The only loss of events came from those with

$$4^{\circ} < \theta_p' < \tan^{-1} (\sqrt{2} \tan 4^{\circ})$$

with neither of its projected angles exceed 4 degrees. To be exact, when an event has

$$4^{\circ} < \theta_p' < \tan^{-1} (\sqrt{2} \tan 4^{\circ}),$$

its being picked up or not depended on the azimuthal angle Φ_p' for

$$\theta_p'^{H} = \tan^{-1} (\tan \theta_p' \cos \Phi_p')$$

$$\theta_p'^{V} = \tan^{-1} (\tan \theta_p' \sin \Phi_p') .$$

Our criteria would reject completely the events with $\theta'_p \leq 4^o$ and accept completely events with

$$\theta'_p > \tan^{-1} (\sqrt{2} \tan 4^o) .$$

Figure 6.18 shows a plot of events as a function of θ'_p, the sharp rise between 4 and 6 degrees is due to the fact that events with θ'_p in that range were only partially accepted. Fortunately, the effective analyzing power for θ'_p less than 5 degrees is too small to be useful at all energies. Since the weight of each event in determining the final polarization is proportional to its analyzing power, the events with

$$4^o < \theta'_p < \tan^{-1} (\sqrt{2} \tan 4^o)$$

had a disproportional small weight in the analysis.

Among the other criteria were

1. An event must have a track length of at least three sparks, because it takes at least three sparks for a least square line fit.
2. Every event must be correlated in all views. Minimum distance in space between the incoming proton and the scattered proton fitted trajectories should be less than 1 cm.
3. If the scattered track stopped inside the range chamber, the inelasticity ($\Delta T_p = T_p(\text{mag}) - T_p(\text{range})$) was required to be between - 60 and 190 MeV. This requirement was aimed to discriminate against the highly inelastic events like the double-scattered events and two prong events (v type events, see Figure 6.8-C) which the line fitting scheme

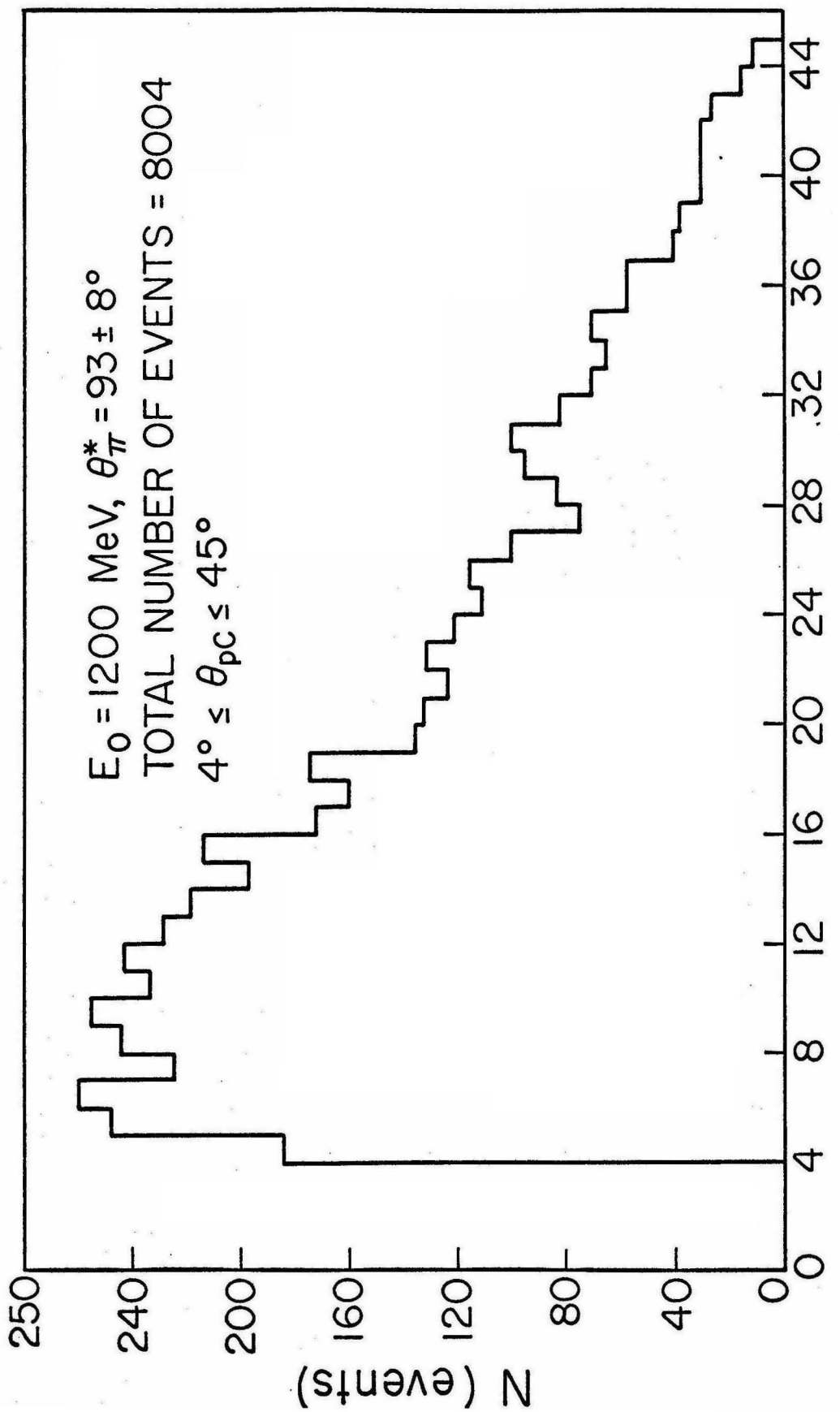

Figure 6.18 Distribution of p-C polar scattering angle with E_o = 1200 MeV, $\theta^*_\pi = 93 \pm 8°$.

usually failed to reject.

4. We rejected events with the scattered track leaving through the sides of the range chamber, but keep events with the scattered track leaving the back of the range chamber. At θ^*_π = 93 degrees and synchrotron end point energy 1375 MeV, the recoil proton of this setting could have a kinetic energy of as much as 500 MeV. The range chamber can only stop protons up to 310 MeV. For events with T_p > 310 MeV, only the energy at the scattering vertex can be determined, but not the precise inelasticity of the scattering. Events without a calculable inelasticity gave rise to a problem as to how an analyzing power might be assigned to them. Our solution is demonstrated in Appendix 6.14.

The scanning program further provided a pre-selection of events based on the energy in the p-C scatter as roughly determined by the number of carbon modules after the scatter. The cutoff was placed at 90 MeV, because the carbon analyzing power drops sharply to zero at all θ'_p below this energy.

The computer output of the preliminary data reduction was a single list of supposedly good events, each accompanied with pertinent information, like the location of the scattering vertex, the module of track stop, inelasticity, pion production angle, p-C scattering angles θ'_p, Φ'_p, etc. However, to be certain that the criteria were being consistently applied, a data tape would regularly be selected to be scanned visually by playing it back on the computer scope. The event number of the seemingly good events were recorded independent of the

computer output. This list was then checked against that of computer output. Any inconsistencies were checked one by one until either we were satisfied with the computer output, or a correction was applied to remove the inconsistency.

To summarize, the bias introduced in this experiment by either the scanning procedure or the data handling appears to be consistent with zero, and certainly is much smaller than the purely statistical errors of the measurement.

6.13 Maximum Likelihood Theorem

The maximum likelihood theorem can be stated as follows: [20] Let $f(x_1, x_2, x_3 \ldots x_m, a)$ be a normalized probability distribution of known analytical form of random events that can be described by m random variables and an unknown parameter a. Let successive samples $s_k (k = 1, 2, 3, \ldots)$ be taken, each sample containing n events described by $(x_1, x_2, x_3, \ldots x_m)_j$ where $j = 1, 2, \ldots n$. If there exists any estimate a^* of the parameter a from the data sample s_k such that the likelihood function defined as

$$L(n,k,a) = \prod_{j=1}^{n} f(x_1, x_2, x_3, \ldots x_m, a)_j \qquad (6.13\text{-}1)$$

satisfies the maximum condition

$$\left[\frac{\partial}{\partial a} \ell n\ L(n,k,a)\right]_{a = a^*} = 0, \qquad (6.13\text{-}2)$$

Then the estimate a* is unique and is the most probable value that can be obtained from a measured sample, $(x_1, x_2, x_3, \ldots x_m)_j$, $j = 1, \ldots n$.

For n -->,$^{\infty}$ the likelihood function approaches a gaussian, as can be shown using the central limit theorem. In that case, its variance is estimated using

$$\Delta a = \left\{ - \frac{\partial^2}{\partial a^2} (\ln L(n,k,a)_{a = a^*} \right\}^{-\frac{1}{2}} \qquad (6.13\text{-}3)$$

In our experiment, the gaussian approximation was always a good one. Cramer, in proving the maximum likelihood theorem [21] shows that in the limit of large n, a* approaches the true physical value of the parameter a, with no other method of estimate more accurate.

6.14 Analyzing Power of Carbon

As stated in Section 3.4, the analyzing power A is a property of the analyzer. In the case of carbon, the analyzing power was generally obtained from experiments in double proton carbon scattering. [22] A brief description can be found in E.D. Bloom's thesis. [6]

W. McNeely made an independent survey of the analyzing power of carbon in 1967 in support of Bloom's thesis. The program covers a range of incident proton energies, T_p, between 90 and 300 MeV, of the scattering angle θ_p' between 3 and 30 degrees, and inelasticities up to 50 MeV. The complete account of this investigation can be found in Caltech Synchrotron Internal Report 30. [22]

In this experiment, for the data taken around $\theta_\pi^* = 93^\circ$, T_p could be as high as 500 MeV. To make matters worse, a large percentage of the events did not even stop inside the range chamber after scattering. Hence no precise inelasticity for the scattering could

possibly be evaluated. Therefore McNeely's scheme of analyzing power cannot be applied to these events.

Considerable efforts were made to find a scheme which could cover the events in the range interested. Kinematically they are classified into three categories.

A. $90 < T_p < 300$ MeV, $4 < \theta'_p < 30$ degrees with inelasticity less than 50 MeV.

B. $90 < T_p < 250$ MeV, $4 < \theta'_p < 30$ degrees without inelasticity.
$250 < T_p < 440$ MeV, $4 < \theta'_p < 20$ degrees without inelasticity.

C. $440 < T_p < 640$ MeV, $4 < \theta'_p < 27$ degrees without inelasticity.

For the events belonging to category A, which consisted of all events in $\theta^*_\pi = 63 \pm 8$ degrees and about 65% of the events in $\theta^*_\pi = 93 \pm 8$ degrees, McNeely's scheme was used. A brief summary will be presented in the following.

The scheme takes into account the contributions from the elastic scattering and the first 4 levels of inelastic scattering. The first 4 excitation energies of C_{12} are 4.43, 9.63, 15, and 19 MeV respectively. The effective analyzing power of an event is defined as the statistical mean of the individual analyzing power $A_n(T_p, \theta_p)$ over all excitation levels (n = 0, being the elastic channel, n = 1 first excitation level, etc.). The resolution τ, our experiment obtained for T_p, was on the order of 15 MeV (see Figure 6.16). It was folded into the calculation of the effective analyzing power. The probability that the scattering excited the carbon nucleus to the nth excitation level is proportional to a gaussian statistical factor

$$\omega_n(\Delta T_p, \tau) = \exp\left\{ -\frac{(\Delta T_p - E_n)^2}{2\tau^2} \right\} \qquad (6.14\text{-}1)$$

where E_n is the excitation energy of the nth level in C_{12}. Therefore, the effective analyzing power was defined for each event by

$$A_{eff}(T_p, \theta'_p, \Delta T_p, \tau) = \frac{\sum_{n=0}^{4} \frac{d\sigma_n}{d\Omega} \omega_n(\Delta T_p, \tau) A_n(T_p, \theta'_p)}{\sum_{n=0}^{4} \frac{d\sigma_n}{d\Omega} \omega_n(\Delta T_p, \tau) + EXTRA} , \qquad (6.14\text{-}2)$$

where $\frac{d\sigma_n}{d\Omega}$ is the differential cross section for the nth level excitation. "EXTRA" is a contribution in differential cross section from the region beyond the 4th level of excitation where no contribution to the polarization is expected. In McNeely's program EXTRA was defined as

$$EXTRA = \int_{22}^{\infty} \frac{d^2\sigma}{d\Omega dE} \, e^{-\frac{(\Delta T_p - E)^2}{2\tau^2}} \, dE \qquad (6.14\text{-}3)$$

$$= \left(\overline{\frac{d^2\sigma}{d\Omega dE}} \right) \Bigg|_{E=22} \sqrt{\frac{\pi}{2}}\,\tau \left(1 - ERF \left(\frac{\Delta T_p - 22}{\sqrt{2}\tau} \right) \right) \qquad (6.14\text{-}4)$$

The lower limit of 22 MeV was selected because the 4th level excitation energy at 19 MeV was assumed to have a half width of 3 MeV. The contribution between 19 MeV and 22 MeV inelasticity was included in the summation of the denominator of Equation 6.14-2. In evaluating the expression EXTRA from step 6.14-3 to 6.14-4 McNeely made an assumption that the double differential cross section $\frac{d^2\sigma}{d\Omega dE}$ stayed constant

(1mb/str) at all angles and at all energies (from 22 to ∞) . This assumption tends to make EXTRA slightly larger than it should be, or the effective analyzing power smaller than it should be. The difficulty arises from the fact that the best available experimental data [22] (up to date) indicates that $\frac{d^2\sigma}{d\Omega dE}$ at 22 MeV of inelasticity converges to the value of 1mb/str at all angles and at all energies. No detailed information beyond that is available. However, the law of conservation of energy does impose an upper limit on the inelasticity; i.e., the double differential cross section should be zero beyond that upper limit. Since in a p-C scattering, the carbon nucleus only takes a small amount of recoil energy, it is therefore reasonable to approximate the upper limit of inelasticity to be the proton kinetic energy just before the scattering, namely $\Delta E_{max} \tilde{=} T_p$.

A simpleminded model of double differential cross section was devised to meet the need in the region of inelasticity of 22 MeV to ΔE_{max}. The model assumed that $\frac{d^2\sigma}{d\Omega dE}$ decreases uniformly from $\overline{\frac{d^2\sigma}{d\Omega dE}}$ = 1 mb/str at an inelasticity of 22 MeV to zero at maximum inelasticity ΔE_{max}, according to an expression

$$\frac{d^2\sigma}{d\Omega dE}(T_p, \theta'_p, E) = \overline{\frac{d^2\sigma}{d\Omega dE}} \left(1 - \frac{E-22}{\Delta E_{max}-22}\right) \qquad (6.14\text{-}5)$$

With the above two approximations, the expression EXTRA is now

$$\text{EXTRA} = \int_{22}^{\Delta E_{max}} \overline{\frac{d^2\sigma}{d\Omega dE}} \; e^{-\left(\frac{\Delta T_p - E}{\sqrt{2}\tau}\right)^2} dE$$

$$\simeq \left(\overline{\frac{d^2\sigma}{d\Omega dE}}\right) \int_{22}^{T_p} \left(1 - \frac{E-22}{T_p-22}\right) \; e^{-\left(\frac{\Delta T_p - E}{\sqrt{2}\tau}\right)^2} dE$$

$$= \left(\overline{\frac{d^2\sigma}{d\Omega dE}}\right) \frac{\tau}{T_p-22} \left\{ \sqrt{\frac{\pi}{2}} \left(1 + \text{ERF}\left(\frac{\Delta T_p - 22}{\sqrt{2}\tau}\right)\right) (T_p - \Delta T_p) - \tau e^{-\left(\frac{22-\Delta T_p}{\sqrt{2}\tau}\right)^2} \right\}$$

(6.14-6)

The slight modification of EXTRA from McNeely's version only increased the overall effective analyzing power by about 1%, which is smaller than the intrinsic statistical error of data. These errors are roughly 10% for the elastic data and 15% for the inelastic data where they exist. The uncertainty in the polarization values due to this effect is small, as explained in Section 4.1.

The events falling into category B either have their track leaving the back of the range chamber, or their kinetic energy at the point of scattering greater than 300 MeV. Therefore, they could not be handled by McNeely's scheme. These events constitute about 25% of the data taken around $\theta^* = 93$ degrees. The reference used for this set of data was compiled by V.Z. Peterson. [23] He plotted the carbon analyzing power at $T_p = 95, 135, 155, 180, 220, 289, 313$, and 424 MeV as a function of polar scattering angle θ'_p in a range from 3.5 to 30 degrees. In Figure 6.19 each curve is assigned a value of energy

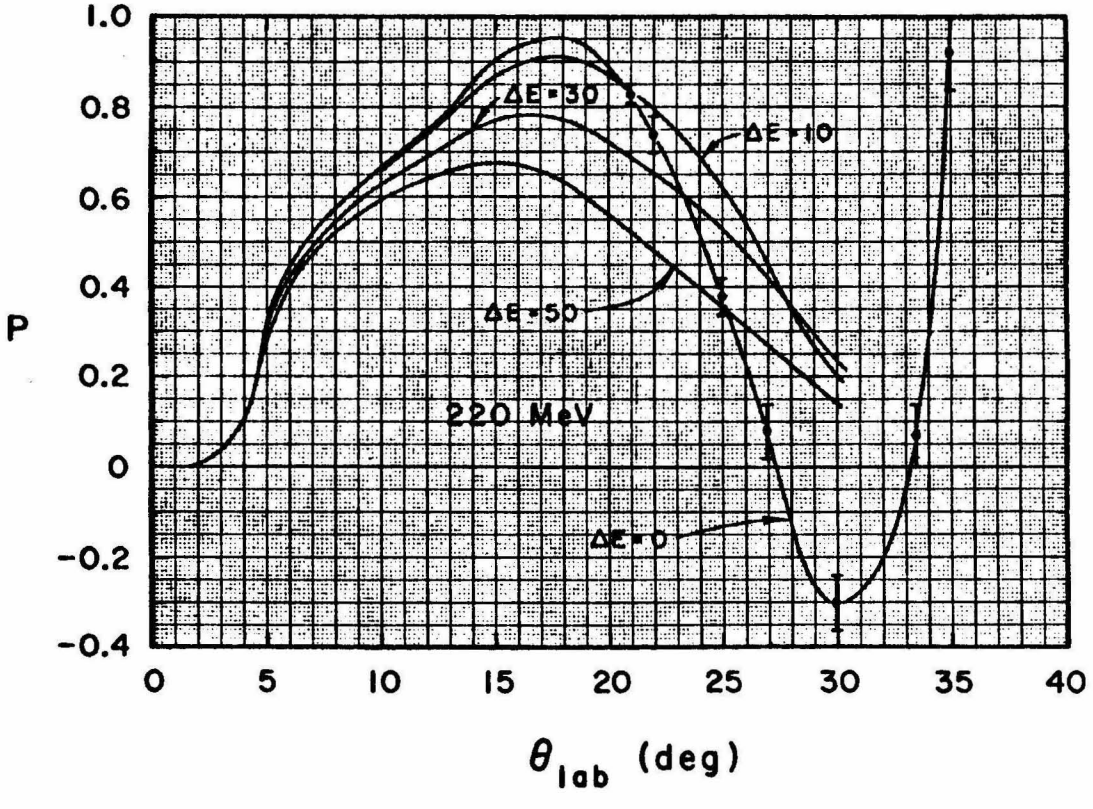

Figure 6.19 Effective carbon analyzing power at T_p = 220 MeV.

acceptance (ΔE). The curve with ΔE = 0 represents the elastic analyzing power. The curve with ΔE = 30 MeV represents the mean analyzing power, averaged over a region of inelasticity up to 30 MeV, etc. To be consistent with the events in category A, we chose the ΔE = 50 MeV curve for our use. Table 6.3 shows the numerical values of the analyzing power at the eight given energies. The interpolation and extrapolation method was used to find the analyzing power throughout the region designated.

We then raised the question: How do we decide whether the event in question whose scattered track most likely left the back of the range chamber, had an inelasticity less than 50 MeV in order to be included in the analyzing power calculation? It was obvious that we could not decide the matter on an individual basis. However, a statistical model was introduced which assigned every event a weight factor of less than 1. The weight factor actually represents the probability that a p-C scattering would result in an inelasticity of less than 50 MeV. This factor is a function of proton kinetic energy T_p and polar scattering angle θ'_p.

To obtain such a factor, we took advantage of the fact that there were nearly 35,000 p-C scattering events which survived the preliminary data reduction. Even after removing the events whose scattered tracks left the back of the range chamber (mostly with high T_p), there were still sufficient events to give us the percentage of events in a given (T_p, θ'_p) bin whose inelasticities were less than 50 MeV. T_p was divided into 30 MeV bins and θ'_p into 3 degree bins. This percentage (or weight factor) tended to decrease inversely with respect

TABLE 6.3 CARBON ANALYZING POWER WITH ENERGY ACCEPTANCE ΔE = 50 MeV.*

θ_p' (degrees)	T_p							
	95	135	155	180	220	289	313	424
4	0.100	0.270	0.335	0.345	0.107	0.085	0.255	0.230
5	0.220	0.420	0.383	0.357	0.278	0.280	0.400	0.270
6	0.230	0.450	0.412	0.382	0.400	0.390	0.467	0.280
7	0.225	0.460	0.430	0.410	0.470	0.462	0.520	0.290
8	0.220	0.470	0.453	0.440	0.520	0.510	0.550	0.300
9	0.217	0.480	0.472	0.471	0.560	0.530	0.562	0.335
10	0.215	0.485	0.495	0.500	0.595	0.547	0.568	0.380
11	0.212	0.492	0.520	0.530	0.620	0.550	0.560	0.354
12	0.215	0.500	0.550	0.557	0.640	0.540	0.545	0.260
13	0.220	0.510	0.580	0.582	0.657	0.517	0.522	0.143
14	0.232	0.526	0.610	0.604	0.670	0.475	0.480	0.063
15	0.250	0.550	0.645	0.623	0.675	0.420	0.430	0.007
16	0.262	0.570	0.670	0.641	0.670	0.367	0.360	-0.014
17	0.282	0.600	0.705	0.643	0.657	0.306	0.300	-0.010
18	0.302	0.620	0.720	0.641	0.632	0.260	0.260	0.007
19	0.322	0.637	0.718	0.629	0.596	0.240	0.243	0.028
20	0.340	0.645	0.707	0.592	0.558	0.220	0.206	0.060
21	0.360	0.650	0.685	0.532	0.520			
22	0.371	0.645	0.655	0.462	0.476			
23	0.382	0.635	0.600	0.400	0.436			
24	0.385	0.610	0.538	0.342	0.395			
25	0.376	0.565	0.475	0.280	0.357			
26	0.358	0.513	0.420	0.220	0.360			
27	0.330	0.460	0.370	0.150	0.267			
28	0.300	0.400	0.330	0.100	0.121			
29	0.170	0.340	0.295	0.089	0.181			
30	0.235	0.290	0.255	0.105	0.139			

*From UCRL - 10622 or Ref. (23)

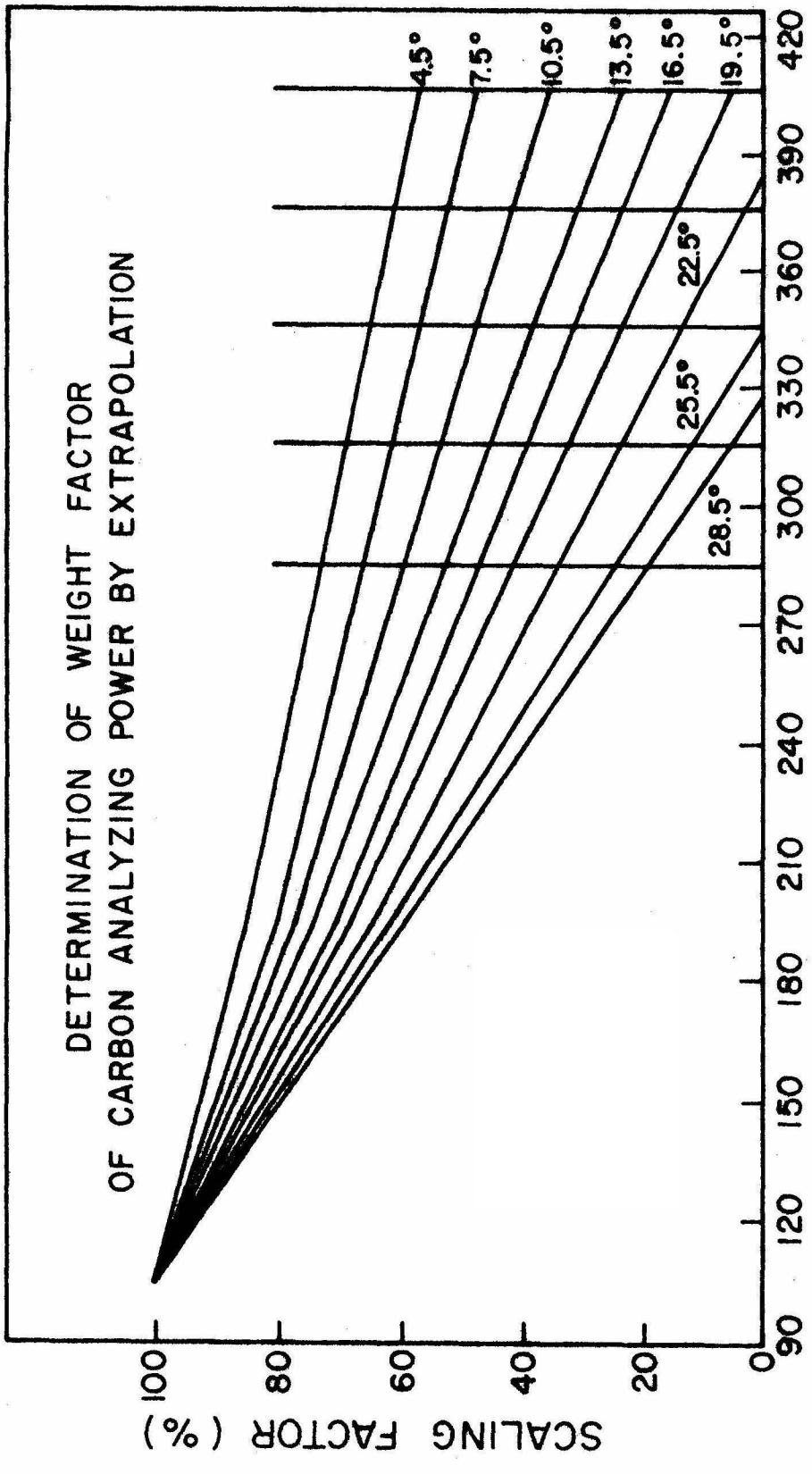

Figure 6.20 Weight factor of carbon analyzing power as a function of T_p.

Incident proton K.E. = 115 ± 15 MeV.
Percentage of events with inelasticity
less than 50 MeV = 96.41%

```
                         INELASTICITY DISTRIBUTION OF P-C SCATTERING

                                 INCIDENT PROTON K. E. = 135.0 +-  15.0
                                 PC POLAR SCATTERING ANGLE =  13.5 +-   1.5
                                 TOTAL # OF EVENTS =   585
                                 EACH X REPRESENTS  1 EVENTS
                                 % EVENTS WITH INELASTICITY .LT. 50. MEV =  96.41
                     # LEFT =    12       # RIGHT =     9 CL =    -7.25     CR =     6.61 FOR EVENTS WITH DTP .GT. 50 MEV
```

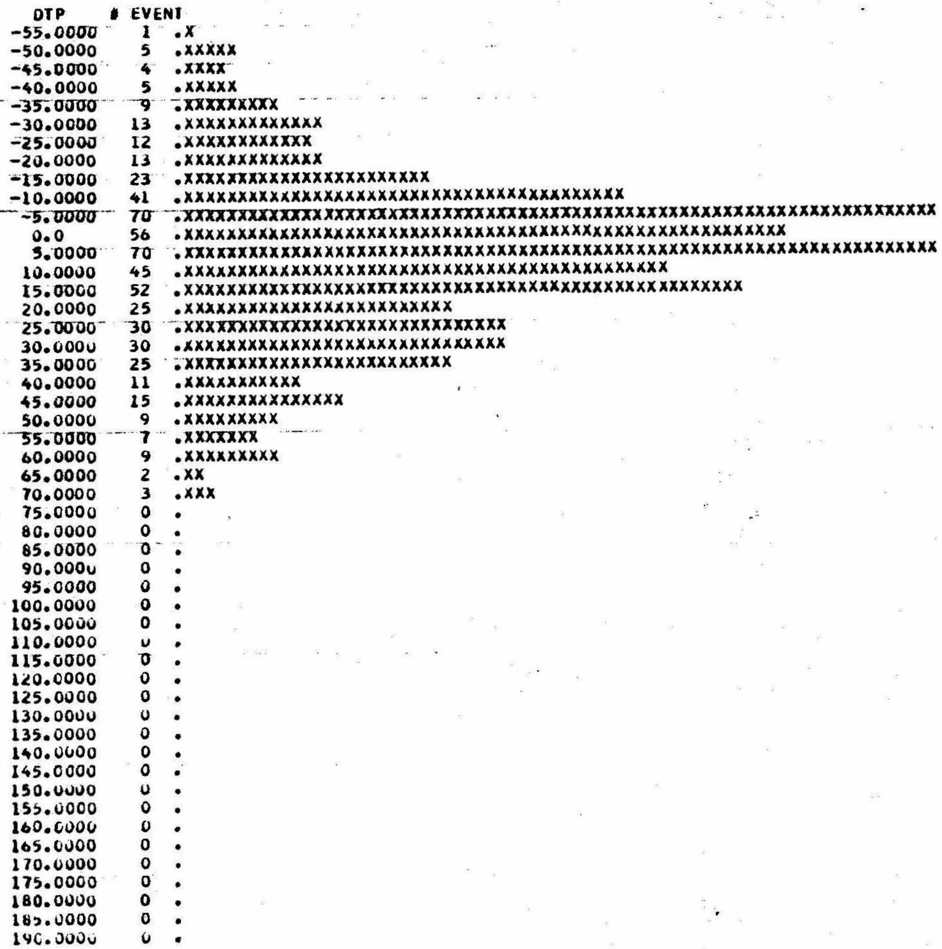

```
      DTP    # EVENT
   -55.0000    1  .X
   -50.0000    5  .XXXXX
   -45.0000    4  .XXXX
   -40.0000    5  .XXXXX
   -35.0000    9  .XXXXXXXXX
   -30.0000   13  .XXXXXXXXXXXXX
   -25.0000   12  .XXXXXXXXXXXX
   -20.0000   13  .XXXXXXXXXXXXX
   -15.0000   23  .XXXXXXXXXXXXXXXXXXXXXXX
   -10.0000   41  .XXXXXXXXXXXXXXXXXXXXXXXXXXXXXXXXXXXXXXXXX
    -5.0000   70  .XXXXXXXXXXXXXXXXXXXXXXXXXXXXXXXXXXXXXXXXXXXXXXXXXXXXXXXXXXXXXXXXXXXXXX
     0.0      56  .XXXXXXXXXXXXXXXXXXXXXXXXXXXXXXXXXXXXXXXXXXXXXXXXXXXXXXXX
     5.0000   70  .XXXXXXXXXXXXXXXXXXXXXXXXXXXXXXXXXXXXXXXXXXXXXXXXXXXXXXXXXXXXXXXXXXXXXX
    10.0000   45  .XXXXXXXXXXXXXXXXXXXXXXXXXXXXXXXXXXXXXXXXXXXXX
    15.0000   52  .XXXXXXXXXXXXXXXXXXXXXXXXXXXXXXXXXXXXXXXXXXXXXXXXXXXX
    20.0000   25  .XXXXXXXXXXXXXXXXXXXXXXXXX
    25.0000   30  .XXXXXXXXXXXXXXXXXXXXXXXXXXXXXX
    30.0000   30  .XXXXXXXXXXXXXXXXXXXXXXXXXXXXXX
    35.0000   25  .XXXXXXXXXXXXXXXXXXXXXXXXX
    40.0000   11  .XXXXXXXXXXX
    45.0000   15  .XXXXXXXXXXXXXXX
    50.0000    9  .XXXXXXXXX
    55.0000    7  .XXXXXXX
    60.0000    9  .XXXXXXXXX
    65.0000    2  .XX
    70.0000    3  .XXX
    75.0000    0  .
    80.0000    0  .
    85.0000    0  .
    90.0000    0  .
    95.0000    0  .
   100.0000    0  .
   105.0000    0  .
   110.0000    0  .
   115.0000    0  .
   120.0000    0  .
   125.0000    0  .
   130.0000    0  .
   135.0000    0  .
   140.0000    0  .
   145.0000    0  .
   150.0000    0  .
   155.0000    0  .
   160.0000    0  .
   165.0000    0  .
   170.0000    0  .
   175.0000    0  .
   180.0000    0  .
   185.0000    0  .
   190.0000    0  .
```

Figure 6.21 Percentage of events with inelasticity less than 50 MeV.

to T_p and θ'_p. It was with this property that the percentage was extrapolated to the region of T_p and θ'_p where a direct estimate was impossible for lack of inelasticity information. Figure 6.20 shows the extrapolation curves. Table 6.4 shows the weight factors used for events in category B. The method of interpolation and extrapolation was again used to assign a weight factor for an event at any given combination of T_p and θ'_p.

A careful check was made to make certain that the polarization calculated by method A and method B agreed within statistical tolerance. This was done by applying method B to events in category A. (The opposite check would not work since method A needs inelasticity as input information, but the events in category B do not have it.) For data taken around $\theta^*_\pi = 63$ degrees, the agreement was good (see Table 6.5). The small disagreement was believed to come from the fact that the events in category A usually had inelasticities far below 50 MeV. They were dealt with individually by McNeely's scheme. The analyzing power thus found was generally slightly higher than that from Peterson's curves for $\Delta E = 50$ MeV.

Events in category C, which constituted only about 10% of the events at $\theta^*_\pi = 93$ degrees, were too energetic to be dealt with by using either method A or method B. A recent paper by Eandi, etc. [24] listed the carbon analyzing power in the region $440 < T_p < 640$ MeV and $5.6 < \theta'_p < 24$ degrees. The inelasticity was not required in that measurement. Table 6.6 shows the analyzing power at all measured points. The analyzing power at different values of T_p and θ'_p was calculated by means of interpolation and extrapolation.

TABLE 8.4: WEIGHT FACTOR OF CARBON ANALYZING POWER WITH ENERGY ACCEPTANCE ΔE = 50 MeV

θ'_p (degrees)*	T_p (MeV)*										
	105	135	165	195	225	255	285	315	345	375	405
4.5	1.00	0.975	0.880	0.830	0.810	0.760	0.720	0.680	0.640	0.600	0.555
7.5	1.00	0.964	0.865	0.800	0.760	0.700	0.655	0.605	0.560	0.510	0.460
10.5	1.00	0.973	0.850	0.770	0.710	0.645	0.590	0.525	0.465	0.405	0.345
13.5	1.00	0.964	0.840	0.740	0.660	0.590	0.520	0.445	0.375	0.300	0.230
16.5	1.00	0.971	0.825	0.710	0.610	0.534	0.460	0.385	0.305	0.225	0.145
19.5	1.00	0.971	0.815	0.680	0.560	0.480	0.410	0.320	0.230	0.140	0.050
22.5	1.00	0.954	0.800	0.650	0.510	0.420	0.330	**			
25.5	1.00	0.953	0.790	0.620	0.460	0.365	0.240				
28.5	1.00	0.969	0.770	0.590	0.410	0.310	0.185				

* A weight factor is a mean value in the bin ($T_p \pm 15$ MeV, $\theta'_p \pm 1.5^o$)

** Irrelevant

TABLE 6.5: POLARIZATION AT 63° CALCULATED BY TWO METHODS

k(MeV)	Weight Factor Method	McNeely's Method*
925	0.22 ± 0.24	0.15 ± 0.24
975	0.08 ± 0.17	-0.01 ± 0.16
1025	0.01 ± 0.12	0.00 ± 0.11
1075	0.15 ± 0.11	0.07 ± 0.10
1125	0.26 ± 0.11	0.16 ± 0.11
1175	0.55 ± 0.13	0.37 ± 0.12
1225	0.12 ± 0.22	0.10 ± 0.20
1275	0.58 ± 0.25	0.56 ± 0.25
1325	0.69 ± 0.30	0.54 ± 0.29

* At $\theta^*_\pi = 63 \pm 8^\circ$ most of the scattered tracks stopped inside the range chamber, i.e., calculation of inelasticity was possible, therefore McNeely's method weighed heavier than the weight factor method in the final calculation. The chi-square value of the two fits shows that

$$\chi^2 = \sum_{i=1}^{9} \left(\frac{P_{mi} - P_{wi}}{\Delta P_{mi}} \right)^2 = 2.3$$

TABLE 6.6: THE EFFECTIVE ANALYZING POWER OF CARBON AT T_p FROM 440 TO 640 MeV*

θ'_p (degrees)	T_p (MeV)										
	440	460	480	500	520	540	560	580	600	670	640
5.6	0.15	0.32	0.24	0.18	0.25	0.20	0.19	0.19	0.20	0.30	0.36
6.2	0.22	0.37	0.33	0.22	0.26	0.20	0.18	0.18	0.25	0.35	0.42
7.5	0.36	0.37	0.42	0.34	0.26	0.24	0.20	0.20	0.31	0.40	0.44
9.0	0.37	0.32	0.36	0.38	0.25	0.26	0.26	0.23	0.32	0.40	0.46
10.5	0.27	0.24	0.31	0.31	0.23	0.25	0.38	0.26	0.30	0.35	0.41
12.0	0.31	0.26	0.27	0.30	0.28	0.25	0.21	0.18	0.28	0.32	0.38
13.5	0.34	0.35	0.34	0.35	0.35	0.33	0.29	0.22	0.30	0.38	0.40
15.0	0.39	0.44	0.35	0.35	0.35	0.40	0.30	0.24	0.27	0.34	0.35
16.5	0.39	0.39	0.23	0.17	0.23	0.31	0.28	0.24	0.24	0.30	0.33
18.0	0.20	0.25	0.26	0.17	0.17	0.30	0.20	0.20	0.20	0.27	0.36
21.0	0.24	0.33	0.36	0.23	0.27	0.27	0.16	0.12	0.18	0.33	0.32
24.0	-0.03	-0.05	0.22	0.29	0.20	0.26	0.12	0.15	0.28	0.22	0.33

*From Ref. (23)

A high percentage of events was lost because of the large scattering angle at high T_p. The remaining events were further reduced by the presence of the weight factors (see Figure 6.12). By the time the polarization was calculated, not too many events survived the double biasing, which in turn made the polarization points above k = 1150 MeV at $\theta^*_\pi = 93 \pm 8$ degrees have large error bars.

To summarize, it is difficult to compile the existing carbon analyzing power data by a unique and general method. The existing data at $T_p > 400$ MeV are scarce and inadequate. On the other hand, when $T_p > 400$ MeV, which is much larger than the C_{12} binding energy (93 MeV), it is doubtful whether the carbon nucleus would still retain its identity after the interaction. The present techniques of measurement never try to detect all the final particles. If high energy p-C interactions are indeed heavily contaminated by the dissociation of the C nucleus or the generation of pions, the measurement of analyzing power using the old technique would become meaningless. The art of polarization measurement might be restricted to the energy region where a high level of confidence can be maintained that the carbon nucleus stays the same before and after the interaction, except for a possible energy level change.

6.15 Proton Carbon Scattering Data

With the 35,000 proton carbon scattering events, all from the same experiment, we were in a good position to present the interaction cross section as a function of polar scattering angle θ'_p in a region from 4 to 45 degrees. As explained in Appendix 6.12, not all

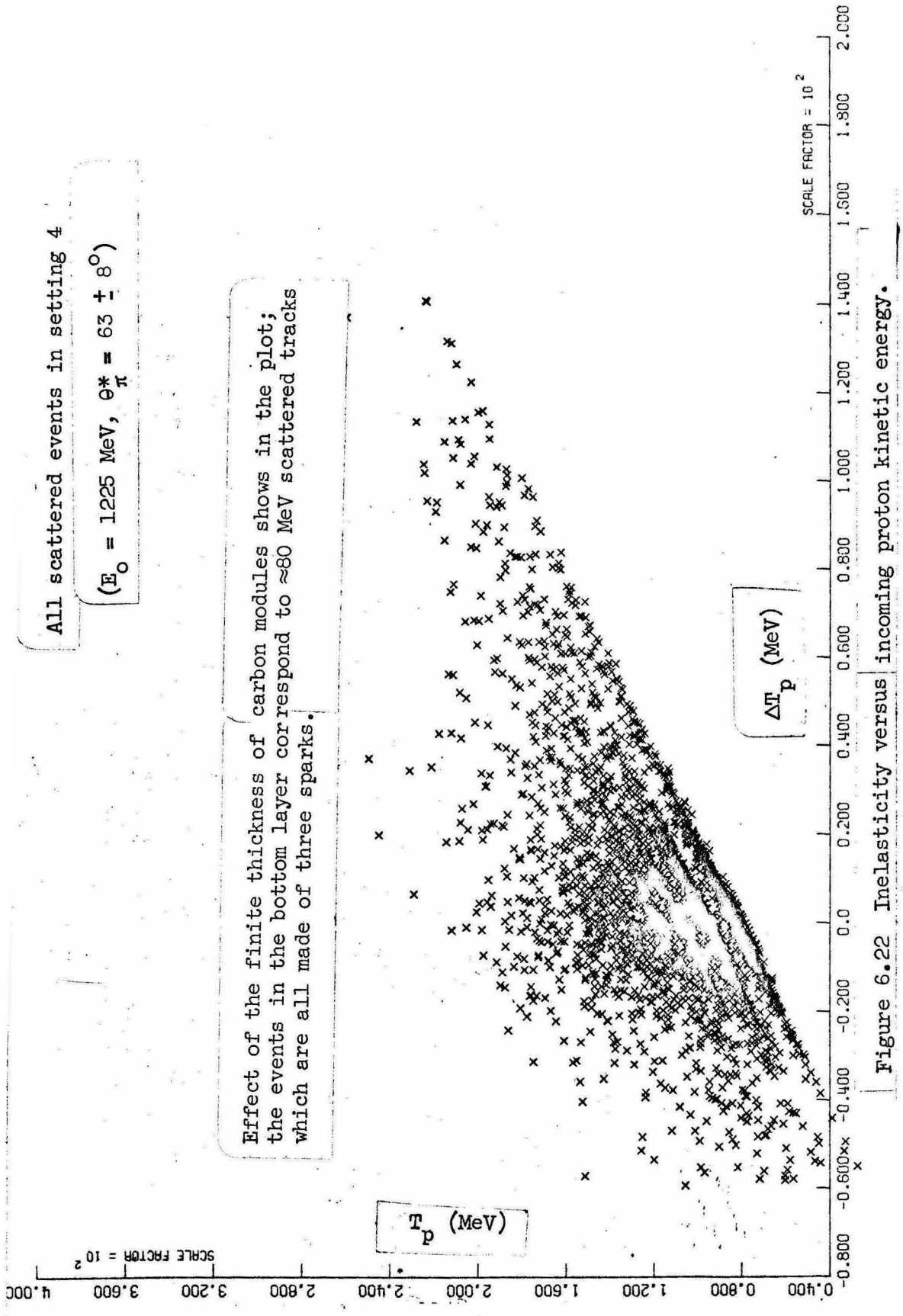

Figure 6.22 Inelasticity versus incoming proton kinetic energy.

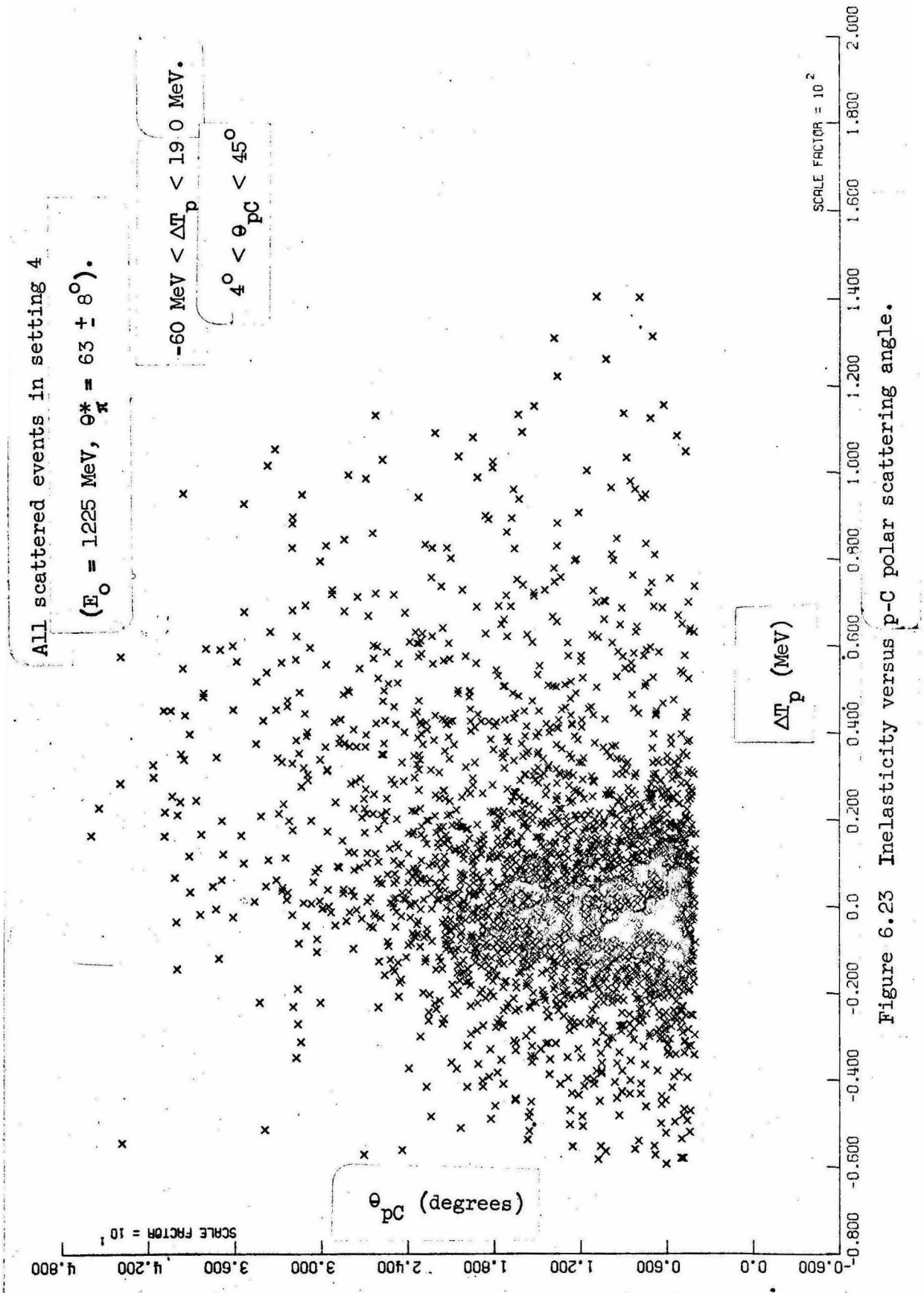

Figure 6.23 Inelasticity versus p-C polar scattering angle.

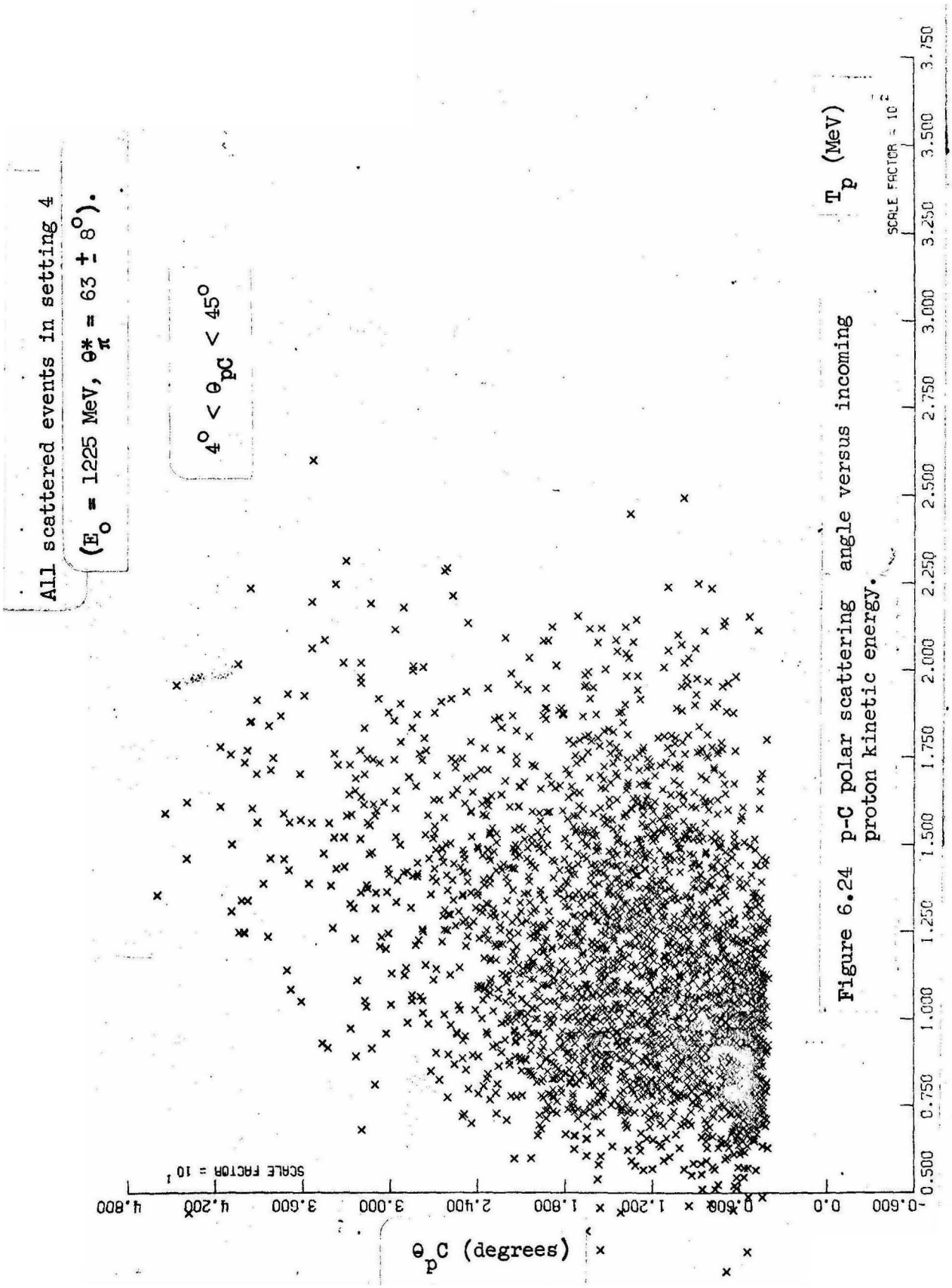

Figure 6.24 p-C polar scattering angle versus incoming proton kinetic energy.

events in the region $4^{o} < \theta'_{p} < \tan^{-1}(\sqrt{2} \tan 4^{o})$ were included because of the way they were selected. Since the energy resolution was typically 15 MeV, no attempts were made to resolve the fine structure of the differential cross section as a function of inelasticity.

From Figure 6.25 to Figure 6.27, the angular differential cross sections of p-C scattering are presented in 50 MeV intervals. Events with all inelasticities are included.

A simple rule that seems to hold true in all the data is that the higher the proton energy the more likely it would be scattered to a large angle (and therefore would be more highly inelastic). No attempt was made to try to explain the structure of these data.

6.16 Geometrical Detection Efficiency of Single π^{o} Photoproduction

To estimate the counting rate of the experiment, a Monte Carlo calculation was performed assuming a single π^{o} production. The input information of the calculation included the dimensions and locations of the liquid hydrogen target, shower counter, proton aperture, and the magnet configuration. It generated an event from a value of k, then tested if the recoil proton successfully entered the proton aperture and, if so, rejected the proton whose trajectory on the exit side of the bending magnet could not satisfy the criteria of the wire orbiting calibration. It then calculated the probability of the shower counter being triggered by at least one decay photon of the π^{o} with energy greater than 250 MeV. An elaborate scheme was devised in this calculation explicitly to take care of the edge effect of the proton aperture. Figures 6.28 and 6.29 show the calculated Monte Carlo geo-

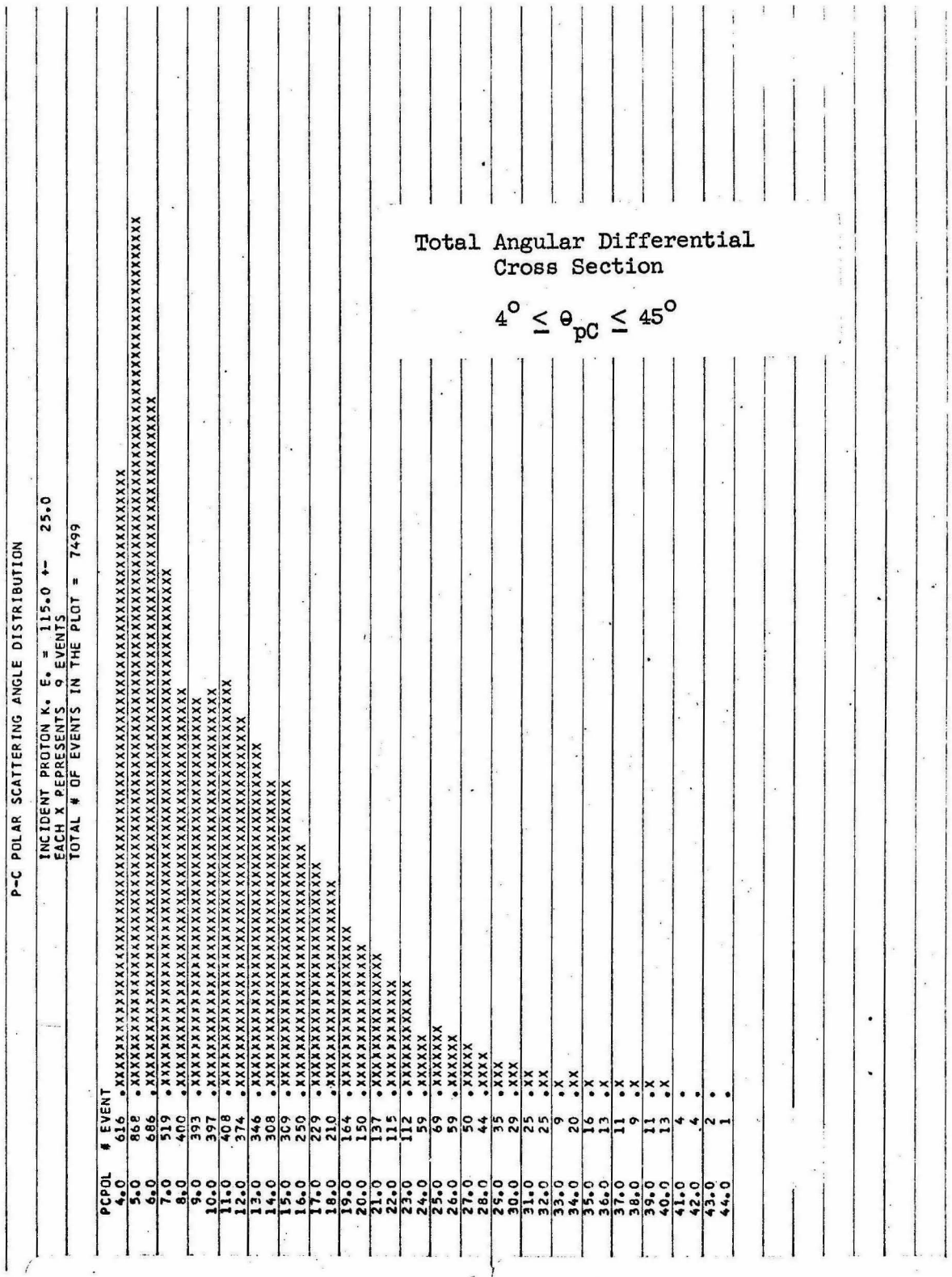

Figure 6.25 A: p-C scattering data at T_p = 115 ± 25 MeV.

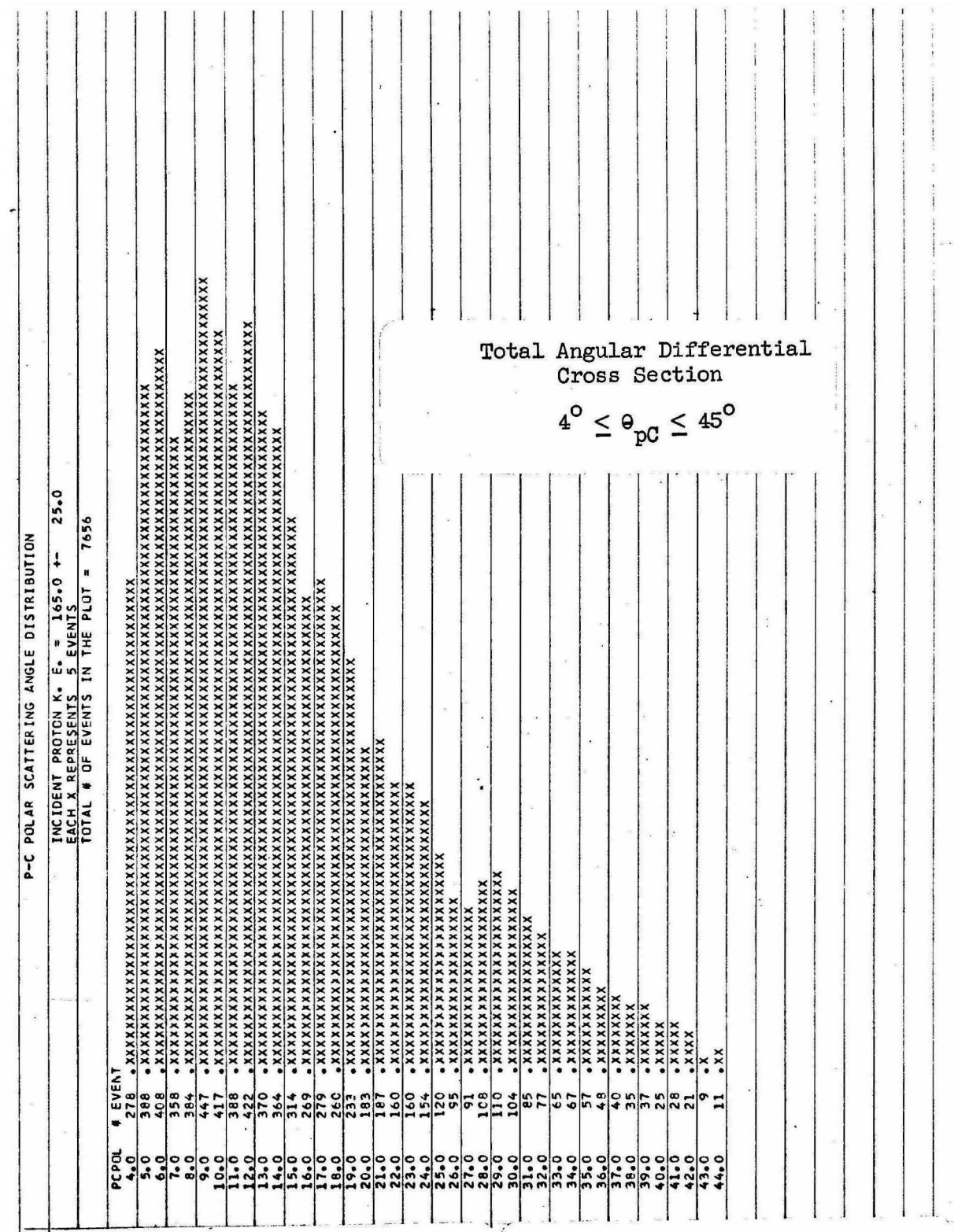

Figure 6.25 B: p-C scattering data at T_p = 165 ± 25 MeV.

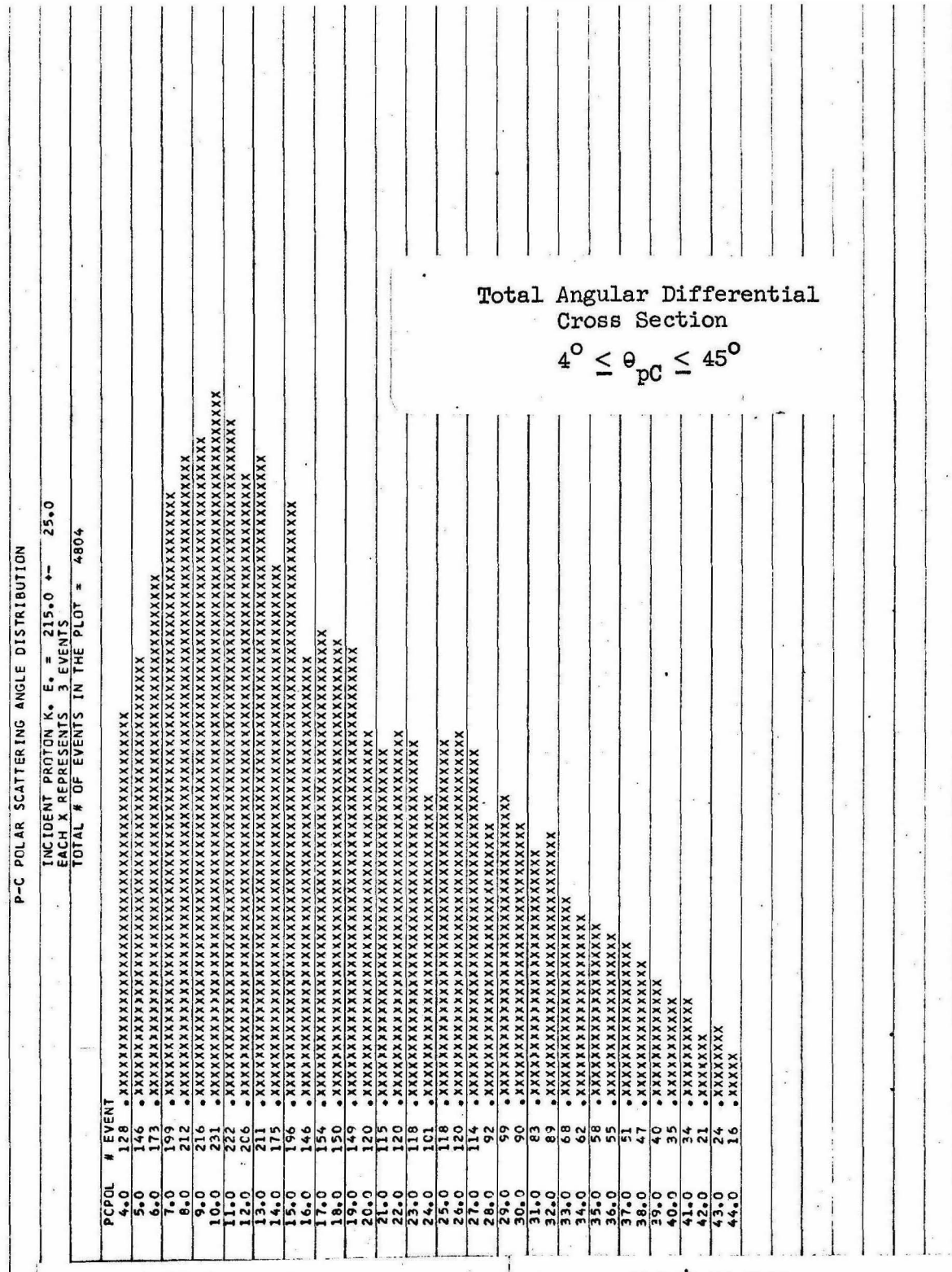

Figure 6.26 A: p-C scattering data at T_p = 215 ± 25 MeV.

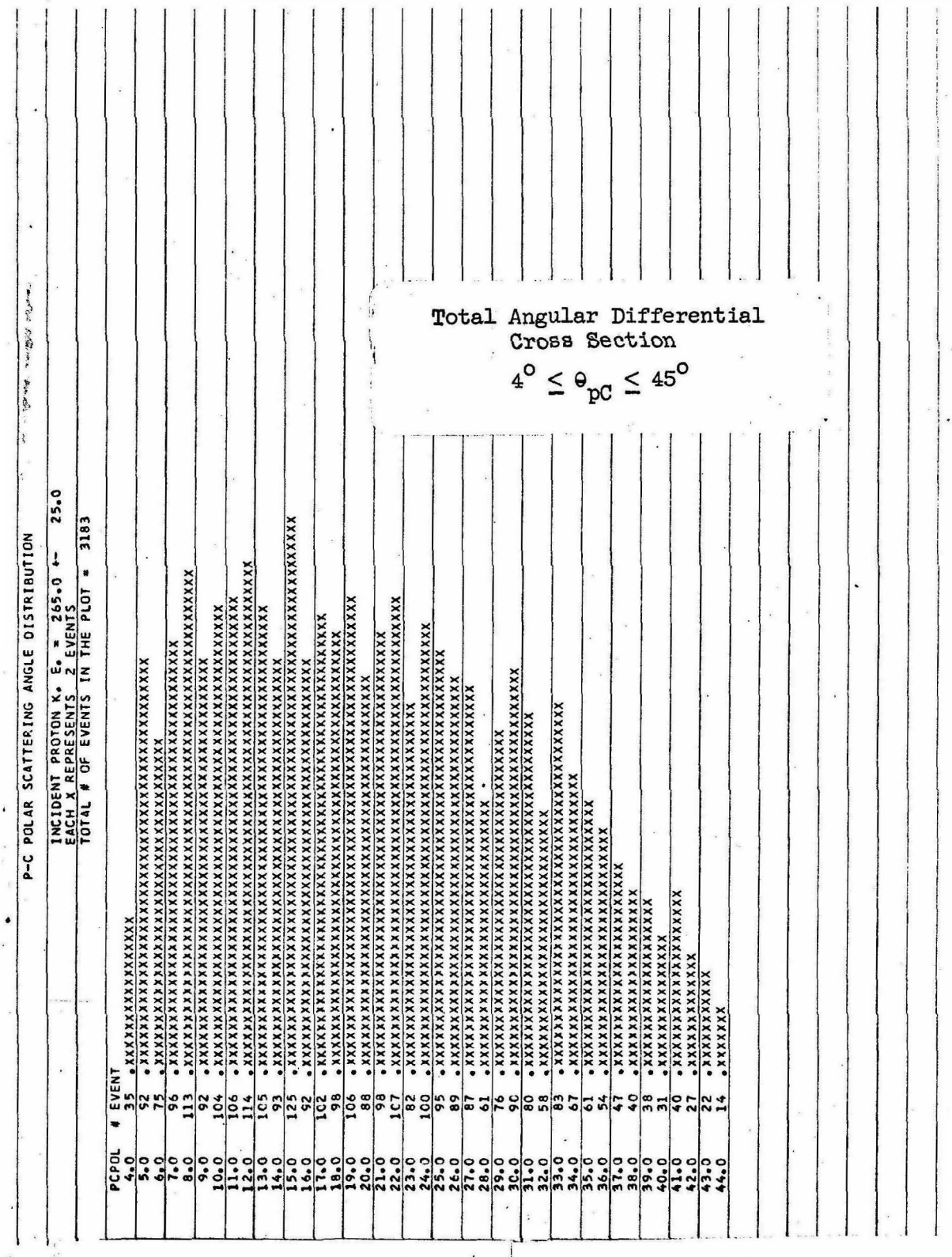

Figure 6.26 B: p-C scattering data at T_p = 265 ± 25 MeV.

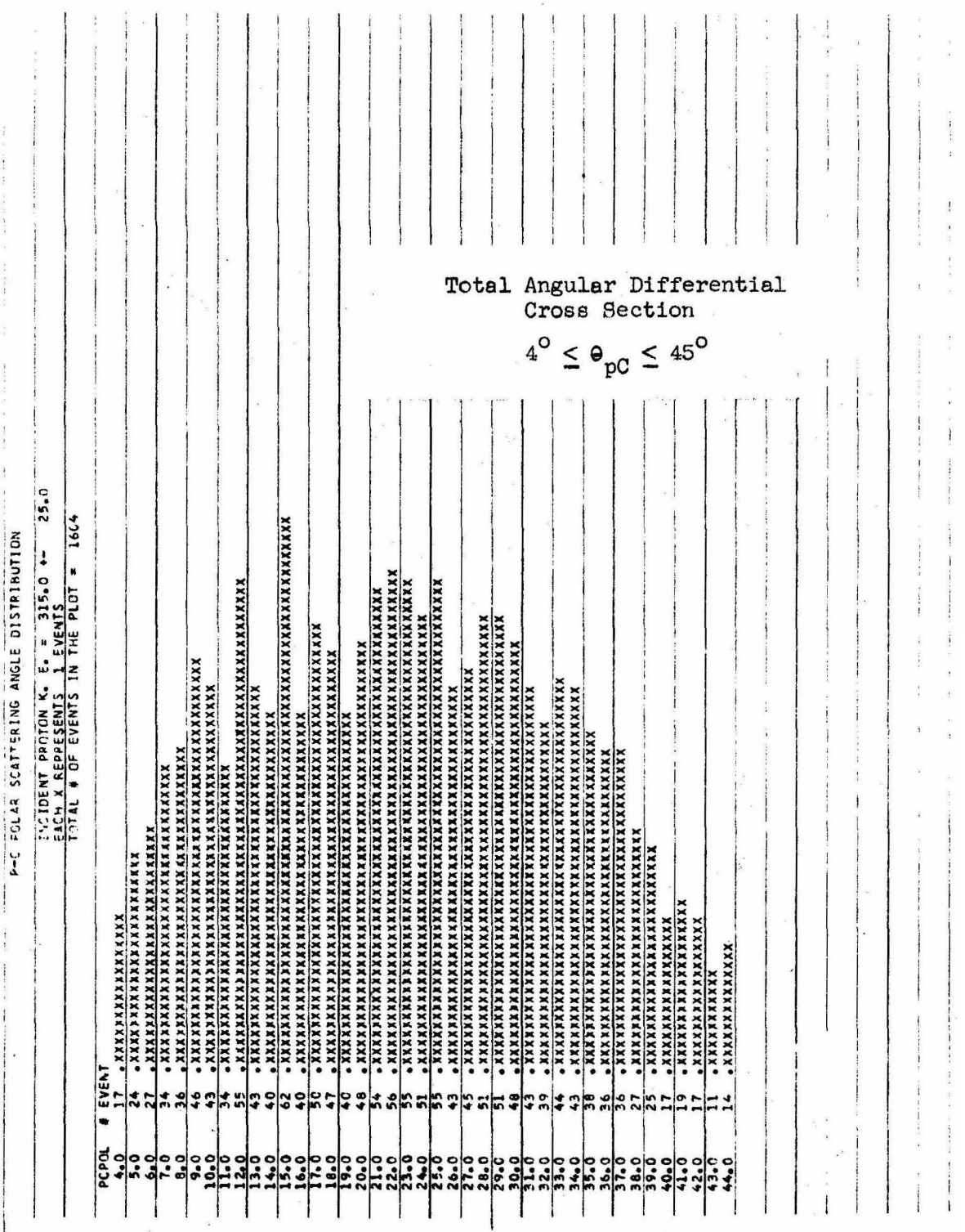

Figure 6.27 A: p-C scattering data at T_p = 315 ± 25 MeV.

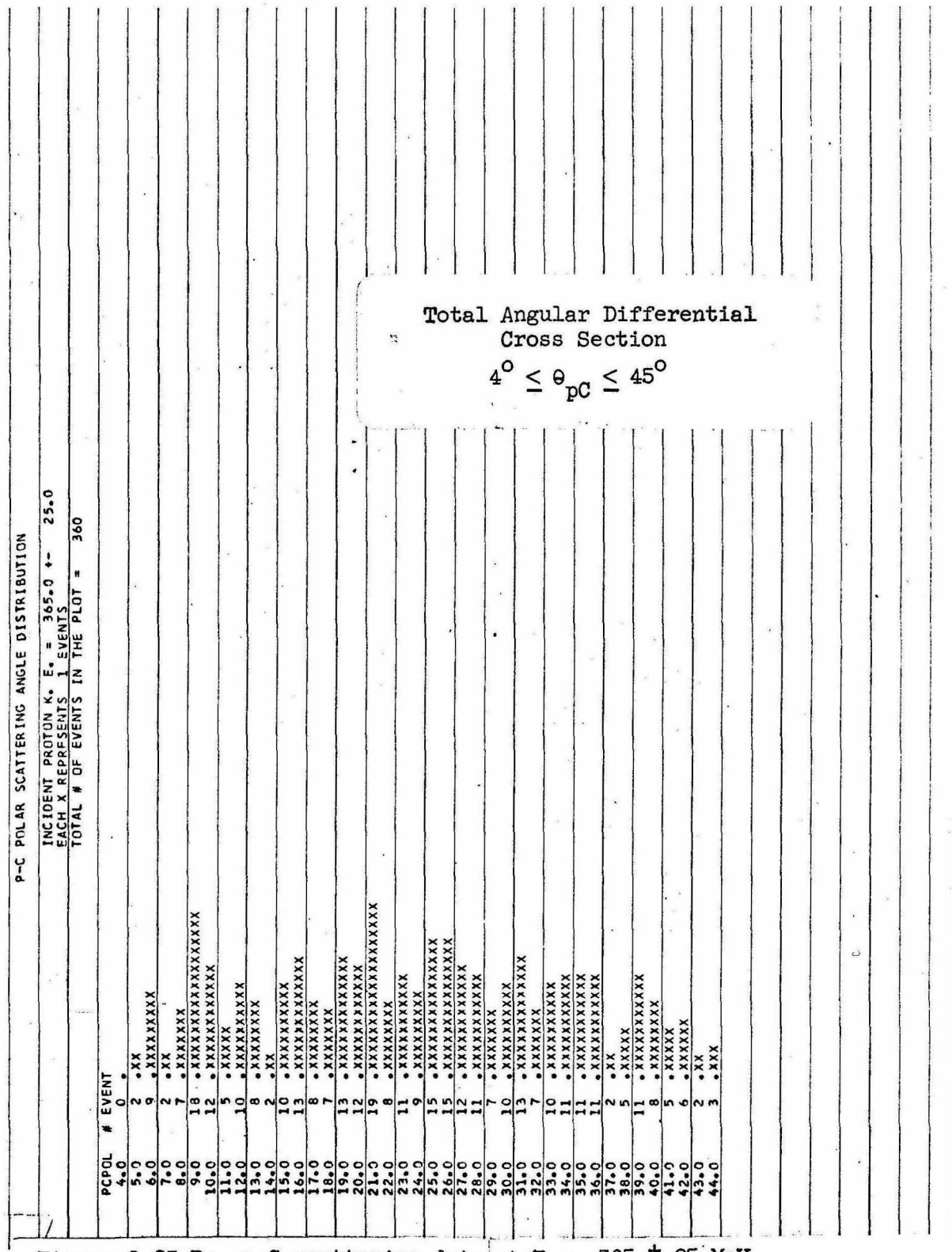

Figure 6.27 B: p-C scattering data at T_p = 365 ± 25 MeV.

metrical detection efficiencies. The numbers in the graphs were used to calculate the pion differential cross section in Section 4.2.

6.17 Calculation of the Contamination of Two π^o Photoproduction Background

A Monte Carlo calculation was performed to estimate the geometrical detection efficiency for two π^o photoproduction events. The calculation was complicated by the fact that three final-state particles decay into a 5-body state almost instantly.

The calculation was made in the following steps.

(1) Choose a photon at energy k, to initiate the reaction $\gamma p \rightarrow 2\pi^o p$, assuming p is produced on the horizontal plane.

(2) Use a random number generator to generate a possible interaction vertex inside the target cylinder.

(3) In the CMS of γp find the momentum range of the recoil proton. The range is then represented by a number of equally spaced momenta each associated with a weighting factor (phase space factor).

(4) For each value of proton momentum in the CMS, try to find the range of theta (in the CMS) explicitly such that the corresponding range of theta in the Lab system can be accepted by the proton aperture.

(5) Make certain that the recoil proton momentum can fit into the prescribed momentum range of the wire-orbit calibration.

(6) Find the motion of the C.M. of the $2\pi^o$ system in Lab.

(7) In the CMS of the $2\pi^o$, let $2\pi^o$ decay isotropically, then

transform each π^o back into Lab system.

(8) In the rest system of the first π^o, let 2γ decay isotropically, then transform them individually into Lab system; see if any γ can trigger the biased shower counter. If not, try the second π^o.

(9) Multiply the efficiency thus found by a factor of $\Delta\Phi_p/2\pi$, $\Delta\Phi_p$ being the azimuthal angular acceptance of the proton aperture.

The calculated detection efficiencies are presented in Figure 6.28 and Figure 6.29. They are on the average of 4% of that of single π^o photoproduction.

To estimate the final background counts, information was also needed on the $2\pi^o$ cross section. Unfortunately, no such measurement has been made because of the experimental complexities involved. Any attempt to try to relate the known $\pi^+\pi^-$ data to $2\pi^o$ data is always confronted with grave difficulties. No single dynamic model proposed could stand for further experimental tests. Hauser [25] found that the OPE model could best describe the qualitative feature of his $\pi^+\pi^-$ data. But the OPE model could not possibly account for the $2\pi^o$ production because of C invariance. It has been generally believed that the $2\pi^o$ cross section could not be larger than that of $\pi^+\pi^-$. The other incomplete evidence from the DESY bubble chamber experiment [13] indicated that the single π^o photoproduction also accounted for most of the photoproduction reactions below k = 1200 MeV. It was with this rather incomplete information that we set an upper limit of 18 μb for the $2\pi^o$ total cross section, for 18 μb was the mean π^o total cross section

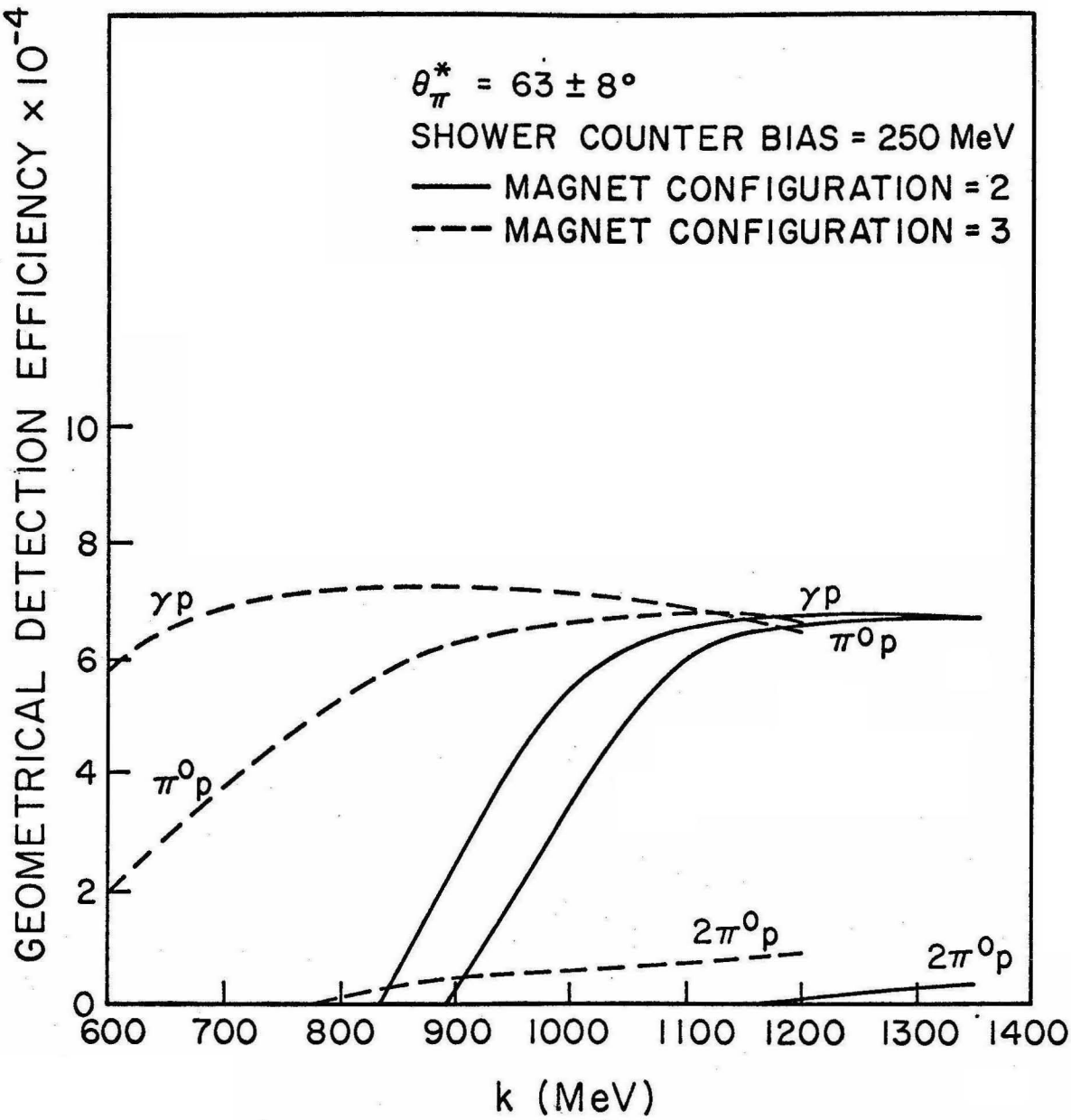

Figure 6.28 Geometrical detection efficiencies at $\theta_\pi^* = 63 \pm 8^\circ$.

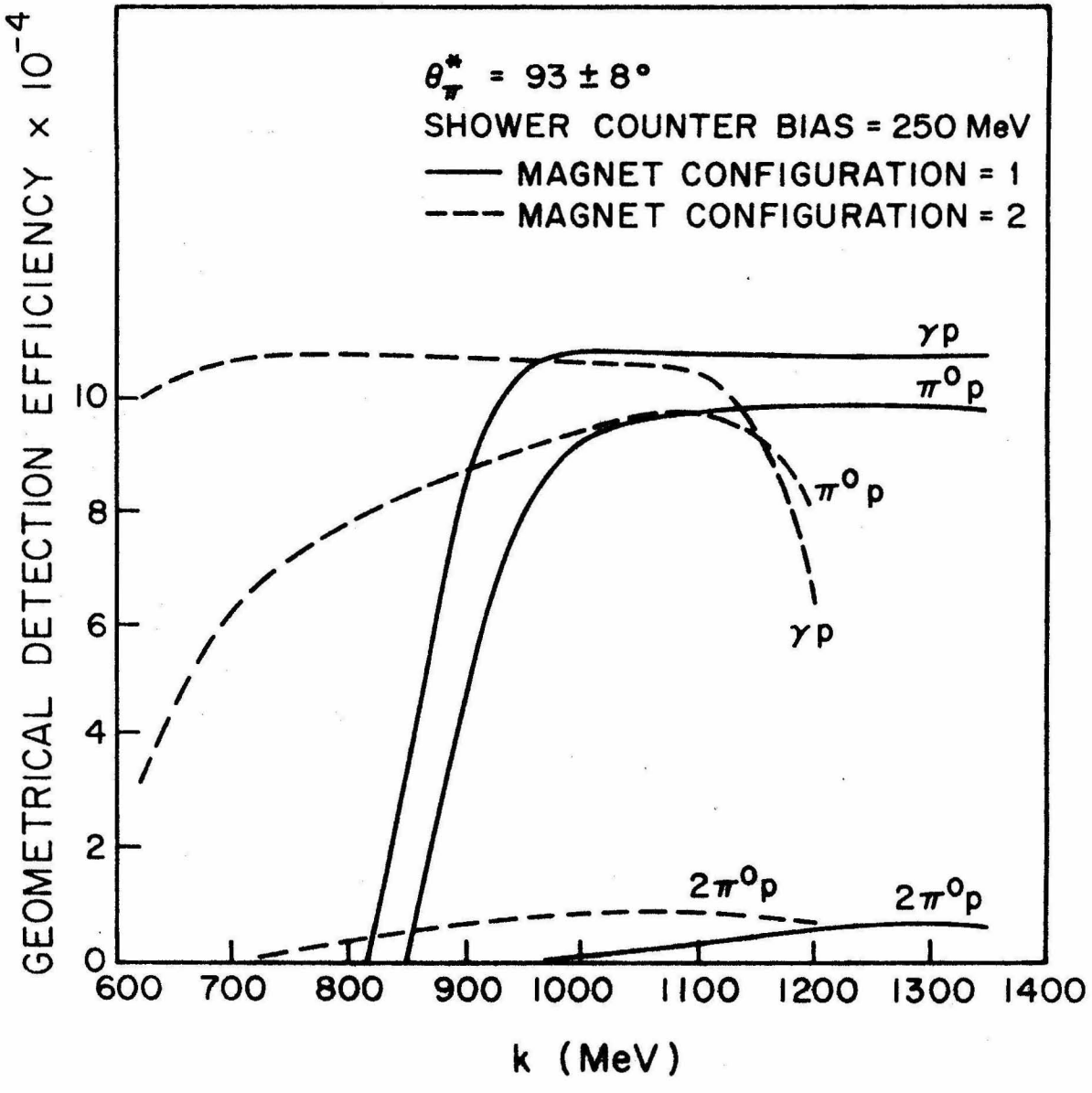

Figure 6.29 Geometrical detection efficiencies at θ^*_π = 93 ± 8°.

in the energy range covered.

Figure 6.30 presents the background counts as a function of incident photon energy in setting 2. The overall contamination of all $2\pi^{o}$ events was on the order of 3%.

6.18 Calculation of the Contamination of Proton Compton Scattering Background

The photon energy in this experiment was always much larger than the rest mass of the π^{o} (135 MeV). Consequently the kinematics of proton Compton scattering was very similar to that of single π^{o} photoproduction. For a comparison at k = 1000 MeV, see Table 6.7.

The scattered photon in Compton scattering behaves very much in the same manner as the forward decaying γ of pion in single π^{o} production. Our γ detection system did not have a hodoscope system to determine the location of shower, nor did the shower counter have a good energy resolution (~15%). Therefore, it was clear that the system would accept a Compton event as easily as a π^{o} event. In fact, because of the 250 MeV pulse height bias of the shower counter, a higher detection efficiency was expected for the Compton events than for the single π^{o} events in the lower region of k.

A relatively simple Monte Carlo type calculation was made to estimate the geometrical detection efficiency for Compton scatter events. The program was modified from the single π^{o} detection scheme: the rest mass of the π^{o} was replaced by zero ($m_{\gamma} = 0$); we then tested whether this scattered γ triggered the biased shower counter.

The differential cross sections of Compton scattering at

TABLE 6.7: KINEMATICS TABLE OF SINGLE π^o PHOTOPRODUCTION AND PROTON COMPTON SCATTERING AT k_γ = 1000 MeV

$\gamma p \rightarrow \pi^o p$							$\gamma p \rightarrow \gamma p$					
	π^o			p			γ			p		
θ_{cm} (degrees)	θ_{lab}	T_π	β_π	θ_{lab}	T_p	β_p	θ_{lab}	T_γ	β_γ	θ_{lab}	T_p	β_p
55	32.4	723	0.99	57.9	142	0.50	32.8	855	1	58.7	145	0.50
57	33.7	713	0.99	56.8	152	0.51	34.1	845	1	57.6	155	0.51
59	35.1	703	0.99	55.8	162	0.52	35.5	835	1	56.6	165	0.53
61	36.4	693	0.99	54.8	172	0.53	36.8	825	1	55.5	175	0.54
63	37.8	683	0.99	53.7	182	0.55	38.2	814	1	54.4	186	0.55
65	39.2	672	0.99	52.7	193	0.56	39.6	804	1	53.4	197	0.56
67	40.6	662	0.99	51.7	203	0.57	41.0	793	1	52.3	207	0.57
69	42.0	651	0.99	50.7	214	0.58	42.5	782	1	51.3	218	0.58
71	43.4	640	0.98	49.6	225	0.59	43.9	770	1	50.2	230	0.60
85	54.1	560	0.98	42.6	305	0.66	54.8	689	1	43.1	311	0.66
87	55.7	549	0.98	41.7	316	0.66	56.4	677	1	42.1	323	0.67
89	57.4	537	0.98	40.7	328	0.67	58.1	666	1	41.1	334	0.68
91	59.1	525	0.98	39.7	340	0.68	59.8	654	1	40.1	346	0.68
93	60.8	514	0.98	38.7	351	0.69	61.6	642	1	39.1	358	0.69
95	60.8	502	0.98	37.8	363	0.69	63.2	630	1	38.1	370	0.70
97	64.3	490	0.98	36.8	375	0.70	65.1	618	1	37.2	382	0.70
99	66.1	479	0.98	35.9	386	0.71	67.0	606	1	36.2	394	0.71
101	68.0	467	0.97	34.9	398	0.71	68.9	595	1	35.2	405	0.72

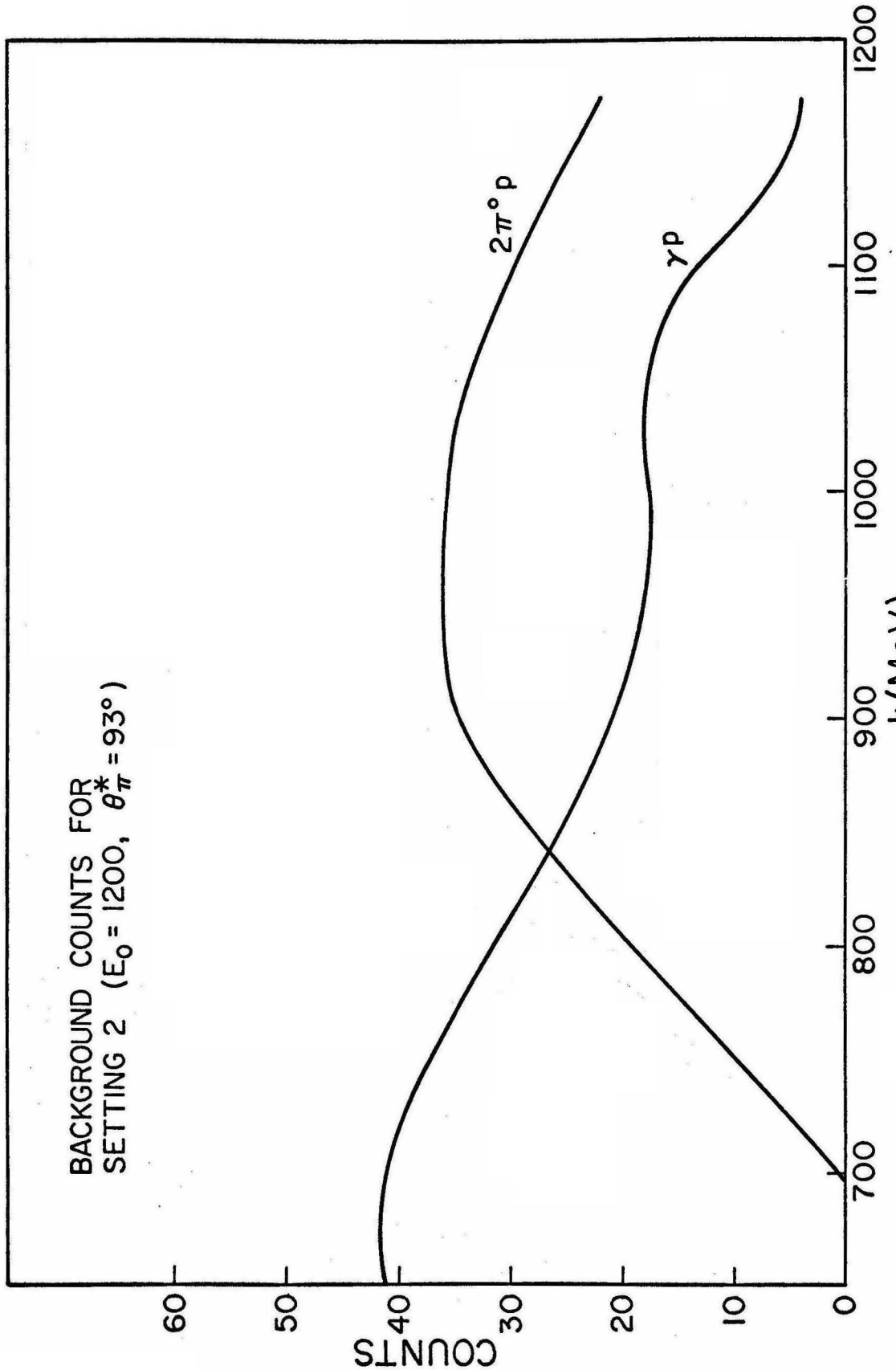

Figure 6.30 Background counts at E_o = 1200 MeV, $\theta^*_\pi = 93 \pm 8^\circ$.

$\theta^*_\gamma = 65^\circ$ and 90° are well known (see Figures 2.4 and 2.5). By folding the cross section with the detection efficiency, we were able to calculate the background counts in setting 2 (see Figure 6.30). The overall contamination was estimated to be on the order of 4%. The worst possible effect of these background events, plus those from $2\pi^\circ$, on polarization was discussed in Section 4.1.

7. REFERENCES

1. R. L. Walker, Physical Review, 182, 1729 (1969).
2. D. Beder, Nuovo Cimento, 33, 94 (1964).
3. M. Jacob and G. C. Wick, An. Physics, 7, 404 (1959).
4. J. J. Sakurai, PRL, 1, 258 (1958).
5. R. M. Talman, Ph.D. Thesis, California Institute of Technology (1963).
6. E. D. Bloom, Ph.D. Thesis, California Institute of Technology (1967).
7. R.Dolen, D. Horn, and C. Schmid, Physical Review, 166, 1768 (1968).
8. C. Chiu and A. Kotanski, Nuclear Phys. 137, 615 (1968).
9. In this experiment we used grade ATJ graphite plates (mean density 1.75 gm/cm^3) for carbon modules. They are consisted presumably predominately of C_{12}.
10. L. Wolfenstein, Ann. Rev. of Nuclear Sciences, 6, 43 (1956).
11. Y. Nagashima, Progress of Theorectical Physics, 33, 828 (1965).
12. D. R. Rust, et al, PRL 15, 938 (1965).
13. DESY Report 65/11.
14. C. Y. Prescott, S. U. Cheng, and K. T. McDonald, Nuclear Inst. and Methods 76, 173 (1969).
15. S. U. Cheng and G. R. Stewart, CTSL Internal Report 48 (1970).
16. W. S. C. Williams, An Introduction to Elementary Particles, Chapter 8 (1961).
17. C. Y. Prescott, Ph.D. Thesis, California Institute of Technology (1966).
18. R. R. Wilson, Nuclear Instruments, 1, 101 (1957).
19. C. A. Heusch, et al, Nuclear Inst. and Methods, 29, 205 (1964).

20. J. O. Maloy, Ph.D. Thesis, California Institute of Technology (1961).

21. H. Cramer, Mathematical Methods of Statistics (Princeton University Press, Princeton, New Jersey, 1958) see p.498.

22. Wm. McNeely, CTSL Internal Report 30 (1967).

23. V. Z. Peterson, UCRL - 10622 (1963).

24. R. D. Eandi et al, Nuclear Inst. and Methods, 32, 213 (1965).

25. W. G. Hauser, Ph.D. Thesis, California Institute of Technology (1967).